RHODES UNIVERSITY
Where leaders learn

A COMPARATIVE MINERALOGICAL AND GEOCHEMICAL STUDY OF MANGANESE DEPOSITS IN THE POSTMASBURG MANGANESE FIELD, SOUTH AFRICA

MAMELLO THOKOA

Thesis submitted to the Department of Geology, Rhodes University in fulfilment of the requirements for the degree of

MASTER OF SCIENCE

February 2020

Supervised by Professor Harilaos Tsikos

Abstract

The Postmasburg Manganese Field (PMF), located in the Northern Cape Province of South Africa, is host to some of the largest deposits of iron and manganese metal in the world. These deposits are restricted to a geographical area known as the Maremane Dome, an anticlinal structure defined by folded dolostones of the Campbellrand Subgroup and overlying iron-formations of the Asbestos Hills Subgroup of the Neoarchaean-Palaeproterozoic Transvaal Supergroup. Manganese ores associated with the Maremane Dome have been divided into two major classes in the literature: the Wolhaarkop breccia-hosted massive ores of the Eastern Belt, as well as the shale-associated ores of the Western Belt. The Eastern Belt ores have been classed as siliceous in nature, while the Western Belt deposits are reported to be typically ferruginous. These divisions were made based on their varying bulk chemical and mineralogical compositions in conjunction with their different stratigraphic sub-settings. Presently, both deposit types are explained as variants of supergene mineralisation that would have formed through a combination of intense ancient lateritic weathering in the presence of oxygen, extreme residual enrichments in Mn (and Fe), and accumulations in karstic depressions at the expense of underlying manganiferous dolostones.

This study revisits these deposits and their origins by sampling representative end-member examples of both Eastern Belt and Western Belt manganese ores in both drillcore (localities Khumani, McCarthy and Leeuwfontein), and outcrop sections (locality Bishop). In an attempt to provide new insights into the processes responsible for the genesis of these deposits, the possibility of hydrothermal influences and associated metasomatic replacement processes is explored in this thesis. This was achieved using standard petrographic and mineralogical techniques (transmitted and reflected light microscopy, XRD , SEM-EDS and EMPA), coupled with bulk-rock geochemical analysis of the same samples using a combination of XRF and LA-ICP-MS analyses.

Combination of field observations, petrographic and mineralogical results, and geochemical data allowed for the re-assessment of the different ore types encountered in the field. Comparative considerations made between the bulk geochemistry of the different end-member ore types revealed no clear-cut compositional distinctions and therefore do not support existing classifications between siliceous (Eastern Belt) and ferruginous (Western Belt) ores. This is supported by trace and REE element data as well, when normalised against average shale. The geochemistry reflects the bulk mineralogy of the ores which is broadly comparable, whereby

braunite and hematite appear to be dominant co-existing minerals in both Eastern Belt (Khumani) and Western Belt (Bishop) ore. In the case of the McCarthy locality, manganese ore is cryptomelane-rich and appears to have involved recent supergene overprint over Eastern Belt type ore, whereas the Leeuwfontein ores are far more ferruginous than at any other locality studied and therefore represent a more complex, hybrid type of oxide-rich Mn mineralisation (mainly bixbyitic) within massive hematite iron ore. In terms of gangue mineralogy, the ores share some close similarities through the omnipresence of barite, and the abundance of alkali-rich silicate minerals. Eastern Belt ores contain abundant albite and serandite whereas the main alkali-rich phase in Western Belt ores is the mineral ephesite. In both cases, Na contents are therefore high at several wt% levels registered in selected samples.

The afore-mentioned alkali enrichments have been variously reported for both these deposit types. The occurrence of high alkalis cannot be explained through classic residual or aqueous supergene systems of ore formation, as proposed in prevailing genetic models in the literature. Together with the detection of halogens such as F and Br through SEM-EDS analyses of ore from both belts, the alkali enrichments suggest possible hydrothermal processes of ore formation involving circulation of metalliferous sodic brines. Selected textural evidence from samples from both ore belts lends support to fluid-related models and allow the proposal for a common hydrothermal-replacement model to have been responsible for ore formation across the broader Maremane Dome region.

Declaration

I declare that this thesis is being submitted in fulfilment for the Master of Sciences degree in the Department of Geology at Rhodes University.

MAMELLO M. THOKOA

……………………………………..

Acknowledgements

I would like to extend my deepest gratitude to PRIMOR as well as the funding company ASSMANG without whose support and funding this research would never have made it off the ground. Next, I would like to pass my deepest gratitude to KUMBA IRON ORE for allowing access to selected boreholes used in this study. A huge thank you as well to Chris van der Merwe and his father Sollie van der Merwe for their guidance, for allowing me access to the McCarthy drill cores, for sharing their knowledge of the region and the deposits as well as the time they spent showing us some magnificent outcrops showcasing the ore of the region. This work wouldn’t be what it is without you.

I would like to extend my utmost gratitude to my supervisor and mentor, Professor Harilaos Tsikos. Conducting research and writing a thesis is no child’s play, it takes a level of critical thinking beyond that of a typical research assignment and project. I am truly grateful to you for opening my eyes to this way of thinking, a way of interrogation far beyond just scratching the surface of geology. Thank you for your guidance and motivation in my times of frustration, I truly appreciate it. I would like to thank the Rhodes Geology staff; Andile ‘Chris’ Pikoli, Thulani Royi, Vuyokazi Nkayi, Ashleigh Goddard, Andrea King for their administrative assistance during this study. I would like to extend my gratitude to Deon van Niekerk for his assistance, time and patience during my microprobe analysis sessions. Mrs Mareli Grobbelaar-Moolman and her team at Stellenbosch University are thanked for their assistance with the delivery of the XRF data used in this project. The Rhodes Chemistry Department staff is also thanked, particularly Dr. Jonathan Britton, for assistance in producing XRD data and going the extra mile by assisting me with further analysis of my samples.

I would like to thank my family for their constant support, for pushing me and always checking on my progress day in and day out especially in the final stages of my research when I was running out of steam. You guys were the wind beneath my wings. I would like to show appreciation and gratitude to Naso, for being patient and understanding in my times of frustration and anxiety, but most importantly for being my biggest cheerleader. You are truly appreciated.

Last but not least, I would like to thank my friends for their support as well as the PRIMOR family, for the laughs, assistance and motivation. Donald Motilaodi, I’m going to miss having you as a friend and office partner, and you Xolane Mhlanga, for always attending to my many questions despite the time differences, thank you.

Table of Contents

1 Introduction

1.1 General

The Late Archean and Early Paleoproterozoic were significant time periods in geological history for the development and deposition of economically important manganese and iron ore deposits (Roy, 2006; Gutzmer and Beukes, 2008). Iron and manganese ores are hosted by deposits of various sizes, metal grades and formation processes, however 95% of the deposits exploited today are sedimentary in nature (Gutzmer and Beukes, 2008). Of these, the iron and manganese deposits of the Northern Cape in South Africa are considered to be among the largest resources in the world (Astrup and Tsikos, 1998).

The Northern Cape deposits have been of interest to explorers and researchers since the 1800s (Cairncross and Beukes, 2013) with the first geological journal publication of this area dating back to 1987 by the European explorer G.W. Stow (Cairncross & Beukes, 2013). These iron and manganese deposits can be subdivided into two major fields; the Kalahari Manganese Field (KMF) and the Postmasburg Managanese Field (PMF), both hosted in the Griqualand West Basin. Exploration and mining initially began in the PMF in the 1920s (Gutzmer and Beukes, 1996); however, by the 1980s attention had already turned to the KMF which offered ore of much higher grades and volumes, and simpler geological setting for effective exploitation (Gutzmer, 1996). Apart from the superior ore hosted in the KMF, other factors which resulted in the closure of mines in the PMF at the time included the irregularity of the size and shape of the PMF deposits, as well as their often-unfavourable composition for market purposes (Gutzmer, 1996).

The huge growth in exploration and mining of iron and manganese across the globe is driven by the growing steel-making industry (Gutzmer and Beukes, 2009). Advancements in European technology to exploit these massive iron ore reserves (Friede, 1980) as well as the introduction of the blast furnace which allowed for easier smelting of iron, further aided the development and sustained growth of this industry, and hence more exploration and mining for raw ore. Apart from its role in the steel-making industry, manganese also sparked interest to miners and researchers alike as a certain percentage of the metal also goes into battery and chemical industries (Astrup and Tsikos, 1998). With this huge growing market for manganese, an understanding of the ore genesis as well as exploration for new resources has become of increased importance to researchers and investors alike.

1.2 Regional Geology

Rocks of the Palaeoproterozoic Transvaal Supergroup are well preserved within the Kaapvaal Craton, an Archean geotectonic unit which covers an area of roughly 1,200 km^2 (Beukes, 1986). The Transvaal Supergroup was initially deposited in a single sedimentary basin; however, the development of a natural barrier known as the Vryburg rise, effectively resulted in the subdivision of this once single basin into two sub-basins, namely the Transvaal and Griqualand West Basins. The Transvaal Basin circumscribes the Bushveld Complex, the world's largest layered intrusion while the Griqualand West Basin is host to the KMF and PMF iron and manganese deposits (Fig 1; after Moore *et al.,* 2001). For the purpose of this study, only the stratigraphy of the Transvaal Supergroup in the Griqualand West Basin will be dealt with in detail.

1.2.1 Ghaap Group

The Griqualand West basin comprises two major stratigraphic entities, namely the Transvaal Supergroup and the overlying Olifantshoek Supergroup. The Transvaal Supergroup can be further subdivided into two major Groups, namely the Ghaap Group and the Postmasburg Group (Beukes, 1986). The Ghaap Group, which forms the base of the Transvaal Supergroup in the Griqualand West basin, consists of four subgroups; the Schmidtsdrift, Campbellrand, Asbestos Hills, and Koegas Subgroups (Beukes, 1983). The older Schmidtsdrift Subgroup, which unconformably overlies the ~2.7 Ga volcanic rocks of the Ventersdorp Supergroup (Beukes, 1983) comprises fluvial, shallow marine, intertidal arenites, and platform carbonates (Beukes, 1986). The Campbellrand Subgroup, a 1500-1700m succession of carbonate rocks (mainly dolostone and lesser limestone) conformably overlies the Schmidtsdrift Subgroup (Beukes, 1987). The Campbellrand Subgroup comprises two major paleofacies, the Ghaap Plateau facies and the Prieska facies, which are divided by the Griqualand fault zone (Beukes, 1987). The Ghaap Plateau facies can further be divided into eight formations, of which only two, the Reivilo and the Fairfield Formations are known to be hosts to the manganese of the PMF.

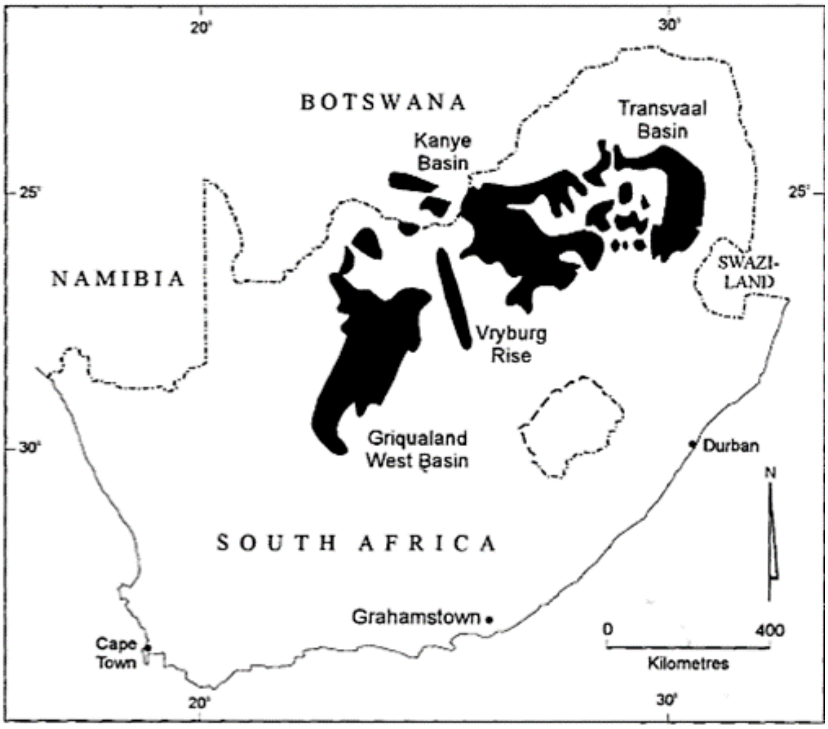

Figure 1: Map showing the distribution of the Griqualand West and Transvaal basins (modified from Moore *et al.,* 2011).

The Reivilo Formation rests on the Monteville Formation and can be divided into 6 members (Beukes, 1980). One of these, the basal Ulco member, consists of giant domal bioherms (Altermann and Siegfried, 1997), which host about 2-3 wt% MnO (Beukes 1978). This is thought to play a very important role as source of metal in the deposits of the PMF. Apart from the bioherms, other facies in the Reivilo Formation include stromatolites, stratiform mats, and chert beds (Altermann and Siegfried, 1997). The chert-bearing Fairfield Formation contains an average of 1-3 wt% MnO, also of importance to the PMF deposits as it is thought to be another key source of manganese to the resultant ore bodies (Beukes, 1978; Phelwe-Leissen, 1995). This formation consists of basal columnar stromatolites, irregular laminoid fenestral mats, intermediate fenestral dolomites with chert replacements, columnar and domal stromatolites with an upper zone of ripple cross-laminated dolarenite, coarsely recrystallised laminoid fenestral dolomite, and a dolomite-clast breccia in a shale matrix upper boundary (Altermann and Siegfried, 1997). The difference between the Reivilo Formation and the Fairfield Formation is that the former is essentially chert-free (Gutzmer and Beukes, 1996). The remaining four formations of the Ghaap Group are summarised in Table 1.

Table 1: Simplified Stratigraphy of the Griqualand West basin (Modified after Altermann and Siegfried, 1997)

SUPERGROUP	GROUP	SUBGROUP	FORMATION	LITHOLOGY
OLIFANTSHOEK		Elim	Hartley	Volcanic rocks
			Lucknow	Quartzites
			Mapedi	Quartzites and shales
TRANSVAAL	POSTMASBURG	Voelwater	Mooidraai	Carbonates with minor chert
			Hotazel	BIF and Mn formations
			Ongeluk	Andesitic basalts
			Makganyene	Diamictite
	GHAAP	Koegas	Nelani	Siliciclastics and BIF
			Rooinekke	
			Naragas	
			Kwakwas	
			Doradale	
			Pannetjie	
		Asbestos Hills	Griquatown	Clastic-textured BIF
			Kuruman	Microbanded BIF
		Campbellrand	Gamohaan	Stromatolitic/laminated carbonates
			Kogelbeen	Dolomites, limestones, cherts
			Klippan	Stromatolitic dolomite
			Papkuil	Stromatolitic/fenestral limestones
			KlipfonteinHeuwel	Silicified stromatolitic dolomites
			Fairfield	Stromatolites, stratiform mats
			Reivilo	Stromatolitic/fenestral dolomites
			Monteville	Dolomites
		Schmidtsdrift		Mudstones and wackes

Overlying the Campbellrand carbonate sequence is the Asbestos Hill Subgroup, a sequence of rocks which comprises the microbanded Kuruman Iron Formation (BIF) and the overlying, clastic-textured (granular) Griquatown Iron Formation (Beukes, 1983). The Kuruman BIF is made up of three members: the Kliphuis member is made up of alternating chert and ankerite-rich mesobands, and forms the basal portion of the Kuruman BIF (Beukes, 1983). This is followed by the chert-rich Groenwater member, and higher up lies the Riries Member, which consists largely of siderite-greenalite rhythmite. The Riries member effectively forms the onset of a very gradual transition to the overlying Griquatown Iron Formation (Beukes, 1983, 1986).

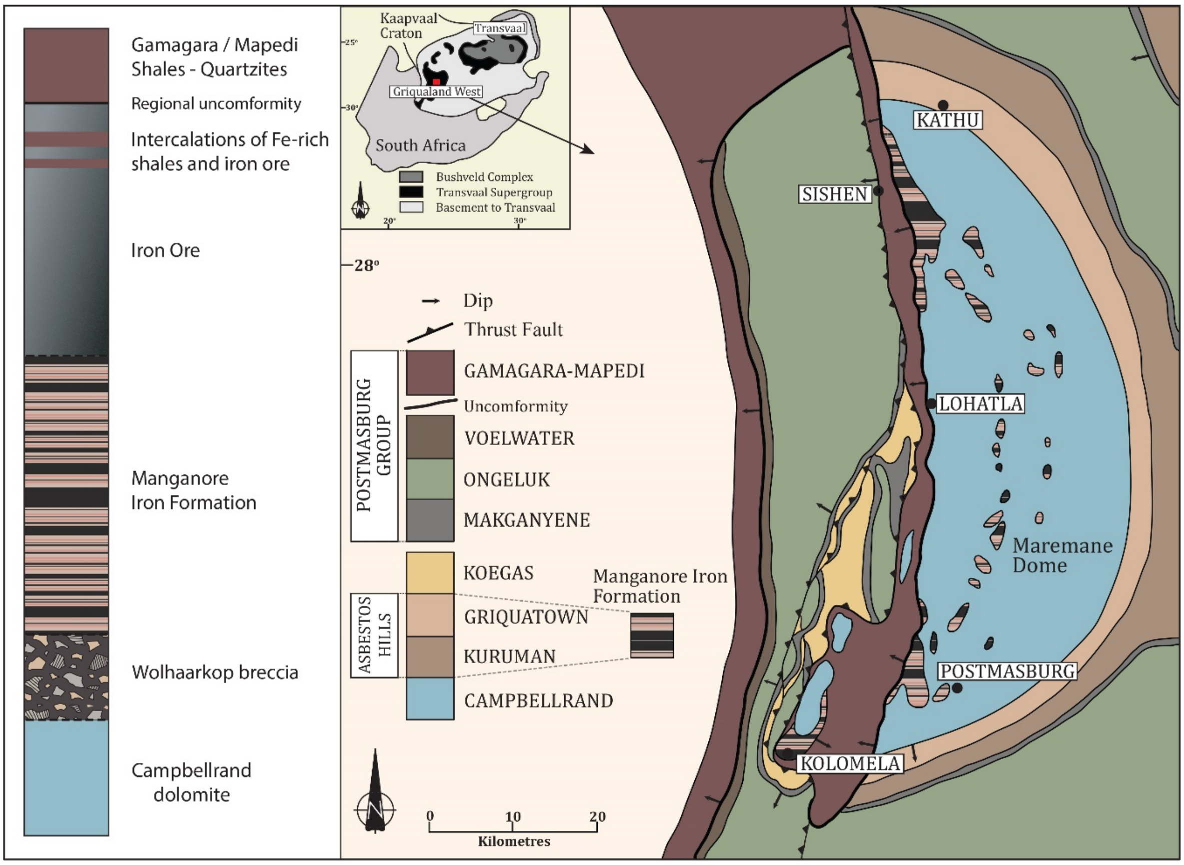

Figure 2: Geological map showing the distribution of the Transvaal and Olifantshoek Supergroups in the Maremane Dome region of the Northern Cape Province. On the left is a column depicting the representative stratigraphic configuration and associated lithotypes that characterise areas of Fe and Mn mineralisation of the eastern belt, as developed within sinkhole structures in carbonate rocks of the Campbellrand Subgroup

The Griquatown Iron-Formation has also been subdivided into three members from the base upwards, namely the Middlewater, Danielskuil, and Pietersberg Members. The Middlewater Member is a siderite-hematite rich facies that grades into predominantly siderite-greenalite mudstone of the Danielskuil member. The Danielskuil member is overlain by mud-clast conglomerates at its top, before finally transitioning into the greenalite-rich muds and siliclastics of the topmost, and final member of the Griquatown Iron Formation, namely the Pietersberg member (Beukes, 1983).

The last unit of the Ghaap Group is the Koegas Subgroup which comprises siliciclastics and iron formations (Beukes, 1986, Tsikos and Moore, 2001). This subgroup is, however, developed only in the southern parts of the Northern Cape Province, effectively south of the Griquatown growth fault (Beukes, 1983, 1986).

1.2.2 The Postmasburg Group

The lower stratigraphic member of the Postmasburg Group is the Makganyene Formation, which consists of glacial diamictites interlayered with shales, sandstones and minor BIF (Moore *et al.,* 2001). According to Beukes (1986) a regional unconformity exists between the Ghaap Group and the Makganyene Formation, which he attributes to a period of uplift and erosion that took place in the region. This was however challenged initially by Moore *et al* (2001) and subsequently rebutted by Polteau *et al* (2006), who indicated that no unconformity appears to be present between the Ghaap and the Postmasburg Group and therefore cannot be denoted as regional. According to Polteau *et al.*, (2006) there is convincing and unequivocal evidence that the transition from the Ghaap Group to the Postmasburg Group is actually transitional, as indicated by diamictite beds that are commonly found interbedded with the upper parts of the Rooinekke BIF of the Koegas Subgroup (Table 1).

Nevertheless, Beukes (1986) interpretation of the Ghaap-Postmasburg uncomformity was used as evidence to strengthen and support a ~2.22 Ga age of the Ongeluk Formation, the volcanic sequence overlying the Makganyene diamictite (Cornell *et al.,* 1996). Polteau *et al.* (2006), as well as Moore *et al*. (2001, 2003, 2012) however, have always disputed the 2.22 Ga age of the Ongeluk Formation, a contention supported further by absolute detrital zircon ages obtained from the Makganyene Formation itself (Moore *et al.,* 2012). This interpretation is also further strengthened by the age of the Mooidraai Formation, a carbonate succession at the very top of the Postmasburg Group (see below), which was dated by Pb-Pb carbonate dating at ~2.39 Ga (Fairey *et al*., 2013). These ages were ultimately confirmed by recent re-dating of the Ongeluk Formation (Gumsley *et al.,* 2017), which effectively placed an end to the dispute on the controversy surrounding the interpreted Ghaap-Postmasburg unconformity.

The Ongeluk Formation consists of basaltic andesites (Polteau *et al.,* 2006) and pillow lavas (Cornell *et al.,* 1996) and conformably overlies the Makganyene Formation. Above the Ongeluk Formation rests conformably the economically very important Hotazel Iron-Formation, which is made up of three sedimentary manganese layers interbedded with BIF. The Hotazel Formation effectively makes up the most dominant succession in the so-called Kalahari Manganese Field (KMF). Overlying the Hotazel Formation and effectively terminating the stratigraphy of the Postmasburg Group is the Mooidraai Formation (Fairey *et al.,* 2013), a largely limestone-rich succession with dolomitized equivalents in the southern KMF.

A regional angular unconformity exists between the Transvaal Supergroup and the basal shale unit of the overlying Olifantshoek Supergroup, known as the Mapedi/Gamagara Formation (Grobbelaar *et al.,* 1995; Yamaguchi and Ohmoto, 2006). This unconformity has been attributed a major metallogenic role in the literature, as it is thought to control primary formation (as paleo-lateritic deposits during its primary development) and subsequent hydrothermal upgrading (as a later fluid conduit) of Fe and Mn ores in both the KMF and the PMF (Gutzmer and Beukes, 1996; Tsikos *et al,* 2003; Moore *et al,* 2011).

1.2.3 Tectonic events and deformation within the Transvaal Supergroup

Deposition of the Transvaal Supergroup was followed by tectonic activity that resulted in some prominent structural features in the region. The first of these is thought to have been a major east-west compressive event associated with folding and uplift in the region (Alchin *et al.,* 2008; Cairncross & Beukes, 2013). This event resulted in the development of the prominent anticlinal feature known as the Maremane Dome, and adjacent associated synclines namely the Dimoten and Ongeluk-Witwater synclines (Fig. 3) (Beukes, 1983; Grobbelaar *et al.,* 1995). A period of non-deposition and erosion followed, over a tie length of probably at least 200 Ma, resulting in the development of the major regional angular unconformity between the Transvaal and Olifantshoek Supergroup (Grobbelaar *et al.,* 1995) as discussed above.

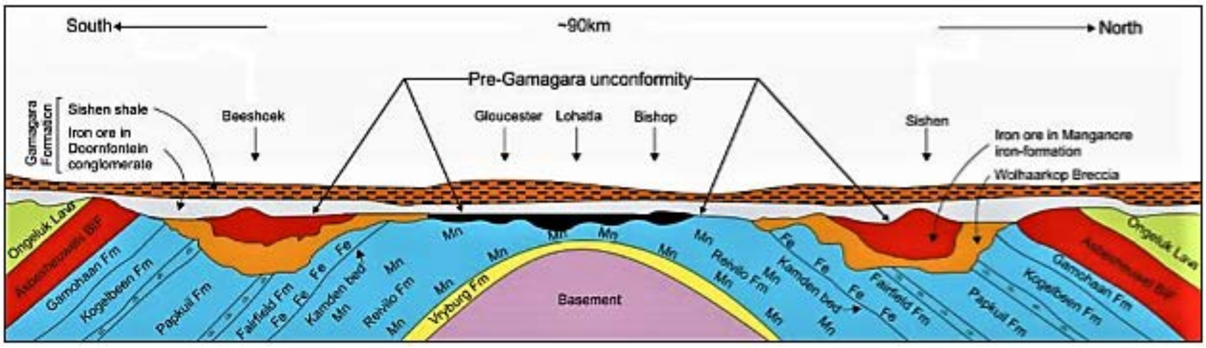

Figure 3: A NS cross-section of the Maremane Dome and associated manganese and iron ore deposits. See also Figure 2 earlier for a plan view of the lateral extent of the Dome (modified after Smith and Beukes, 2016)

A north-south striking metamorphic belt known as the Kheis Belt, found along the western margin of the Kaapvaal Craton, also underwent deformation as a result of the 1830-1730 Ma orogenic event (Tsikos *et al.,* 2003). This event produced the so-called Blackridge thrust towards the western part of the Maremane Dome, which is responsible for duplicating strata of the Transvaal and Olifantshoek Supergroups within the Griqualand West basin (Grobbelaar *et al.,* 1995).

1.2.4 Metasomatic effects

As already alluded to in the foregoing sections, the unconformity between the Olifantshoek and Transvaal Supergroups appears to have played a fundamental role in the formation and/or metal upgrading of both manganese and iron ore deposits, (Moore *et al.,* 2011). The unconformity stretches from the KMF to the north, right across the PMF to the southernmost extremity of the Maremane Dome and beyond. In association with these deposits, evidence for hydrothermal overprinting lies in alkali rich assemblages that have been reported from both the KMF and the PMF. These include occurrences of aegirine, serandite, albite, ephesite, and a wealth of other far more uncommon associated Mn minerals containing alkalis such as norrishite, sugilite, armbrusterite, tokyoite and noelbensonite (Dixon, 1985, 1989; Gutzmer & Beukes, 1996; Tsikos and Moore, 2005; Moore *et al.,* 2011; Costin *et al.,* 2015; Fairey *et al.,* 2019). One of the more recent discoveries is the sugilite associated with the Wolhaarkop breccia obtained from Bruce iron-ore mine in the Northern Cape (Moore *et al*., 2011). Sugilite had been previously reported from the Wessels mine in the northernmost KMF (Dunn *et al.,* 1980; Dixon, 1985, 1989) hence the new discovery of the sugilite assemblage in the PMF suggests that a possibly regional-scale, widespread hydrothermal alteration event in the vicinity of the unconformity between the Olifantshoek and Transvaal Supergroups, is responsible for these occurrences (Moore *et al.,* 2011). Further evidence for regional hydrothermal activity may include the recent findings by Land *et al.,* (2018) on red shales of the Mapedi/Gamagara Formation at the base of the Olifantshoek Supergroup. The specific study reported the presence of anomalous high field strength element concentrations at the lowermost portion of these shales and a high K content throughout the section, which the authors interpret as evidence for an alkaline hydrothermal fluid event, which may or may not be linked to the event/s producing the predominantly sodic assemblages mentioned above.

1.3 Local Geology and Metallogeny of the PMF

The overarching feature of the iron and manganese deposits of the PMF is that they are restricted to the (anticlinal) Maremane Dome, which extends along a 60 km strike from Postmasburg to Sishen in the Northern Cape, South Africa (Gutzmer and Beukes, 1996). The Maremane Dome is predominantly defined by dolomitic outcrops of the Campbellrand Subgroup and iron-formation of the Asbestos Hills Subgroup (Beukes, 1986; Plehwe-Leissen and Klemm, 1995). Strata dip gently in an arc fashion to the north, east and south, at an angle of 10˚ (Beukes, 1978). Ores associated with the Maremane Dome have traditionally been sub-divided into two types, namely Eastern Belt and Western Belt deposits, based on their varying chemical, mineralogical composition, as well as their contrasting stratigraphic placement (Plehwe-Leissen and Klemm, 1995). A third, "mixed-type" of ore seems to contain features of both the Eastern and Western Belts has been described in areas where these two belts meet – such as Rust-en-Vrede and King in the North (Plehwe-Leisen and Klemm, 1995; Gutzmer and Beukes, 1996). The distribution of these ore types on the Maremane Dome is indicated in Figure 4.

The general interpretation of the paleoenvironment of ore formation in the Maremane Dome assumes that the region lay above sea level over protracted lengths of time thus exposing the rocks of the dome to intense chemical and physical erosion. This resulted in widespread karstification of the Campbellrand dolostones and consequently the formation of sinkhole structures. Zones of tectonic weakness on the Maremane Dome that occurred mainly along 10˚, 50˚ and 150˚ strike directions, would have further augmented the loci of karstification (Leisen 1987). In the Eastern belt, which straddles the North, East and South of the dome, dissolution of Campbellrand dolostones would have resulted in the accumulation of a manganese rich residual wad at the base of the karstic structures (Gutzmer and Beukes, 1996). The manganese would have been sourced from the leaching of the chert-rich manganiferous dolomites of the Fairfield Formation (Plehwe-Leissen and Klemm, 1995), which, as indicated earlier, contains an average of 1-3 wt% MnO (Beukes, 1978). The manganese, together with silicified dolomite and remaining chert fragments make up a residual karst breccia that "lines" the karstic surface, known as the Wolhaarkop Breccia.

The Western belt dolostones were, however, exposed to subaerial conditions much longer, and as a result, they were eroded and leached down to the Ulco Member (Beukes, 1978; Plehwe-Leisen and Klemm, 1995). This prolonged exposure means the Asbestos Hills BIF found in the

Eastern Belt is naturally absent here. Instead, reworking of eroded BIF and allochtonous deposition of the so-called Doornfontein Conglomerate – an apparently clastic, detrital deposit of highly ferruginous BIF replaced by hematite and forming much of the commercial iron ores in the region – would only follow much later (Plehwe-Leisen and Klemm, 1995; Gutzmer and Beukes, 1996).

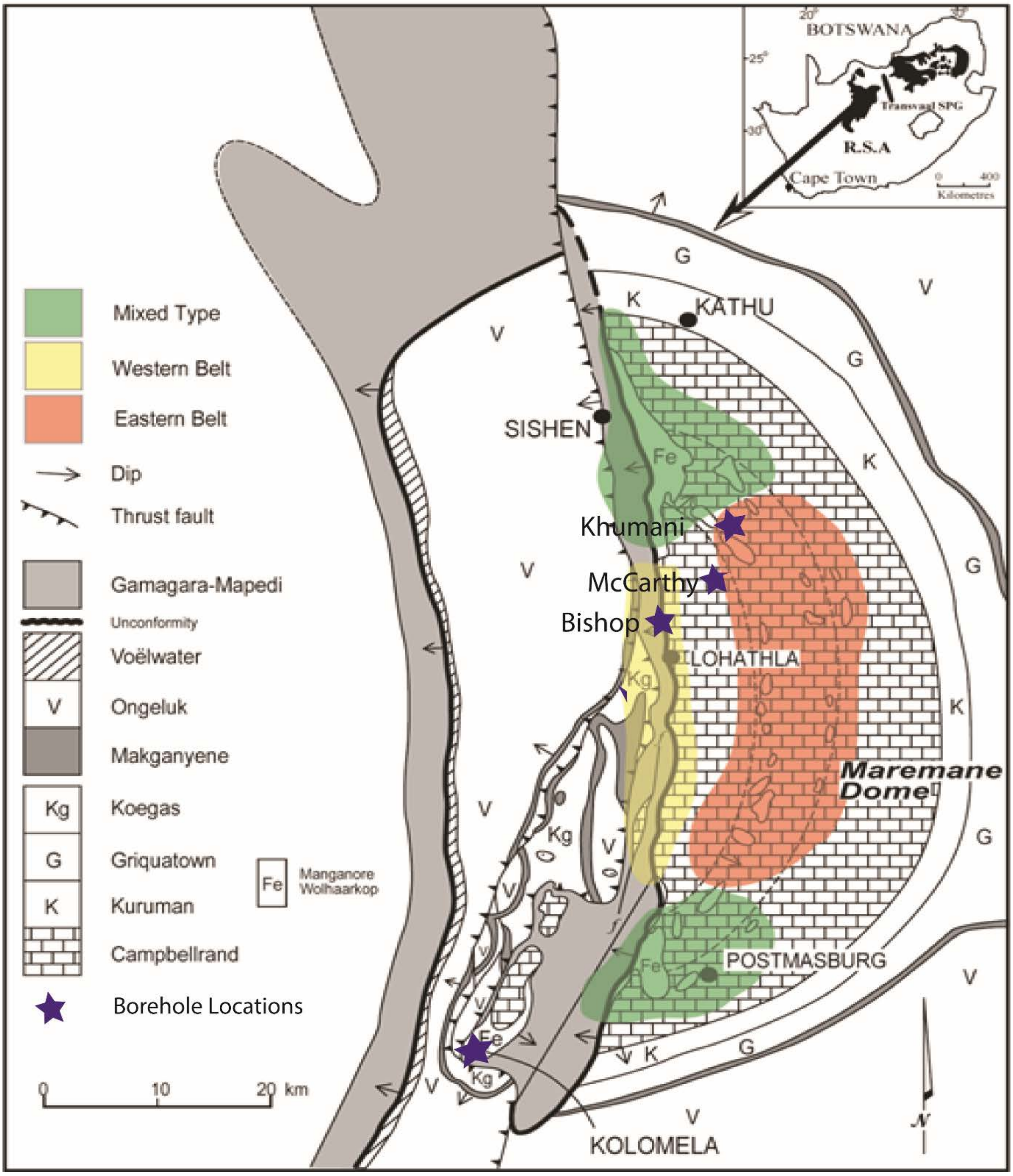

Figure 4: Regional geological map of the study area showing distribution of manganese ore in the eastern and western belts of the Postmasburg Manganese Field (PMF). Localities of drillcores and outcrops where samples were obtained for this study are also indicated (modified after Fairey *et al.,* 2019)

The Doornfontein conglomerate has been interpreted sedimentologically as a transgressive facies (Beukes, 1986) and was ultimately followed by the deposition of the Olifantshoek Supergroup sediments which contain at their base the so-called Gamagara shale. The latter is interpreted as a lateral correlative of the Mapedi (shale) Formation to the north of the Maremane Dome, although recent ages and interpretations appear to question this relationship (Beukes, 1986; Rasmussen *et al.,* 2020). To eliminate confusion of these two shale facies, they will be referred to from here on as the Mapedi/Gamagara Formation. Higher up in the stratigraphy, the Marthaspoort/Lucknow quartzite Member forms a predominant lithology of the Olifantshoek Supergroup right across the region, which protected it from further erosion. especially in the western end of the Maremane Dome where the Gamagara Ridge develops (Plehwe-Leisen and Klemm, 1995). Karstic systems in the east were nonetheless eroded much deeper, leaving behind manganiferous infills which today represent the so-called Klipfontein Hills (Plehwe-Leisen and Klemm, 1995).

1.3.1 The Eastern Belt ores

In the Eastern belt, the interpreted local stratigraphy involves original Kuruman BIF which in a normal stratigraphic context would rest conformably on Capbellrand dolostones. Here however, it is separated from the underlying Campellrand dolostones by a solution collapse unconformity (Gutzmer and Beukes, 1996) which is believed to be a result of slumping of the BIF into the underlying karstic structures. This resulted in the development of highly folded and brecciated deposits which have since been termed Manganore Iron Formation (Beukes, 1983). A residual breccia – the Wolhaarkop breccia – forms at the interface between the Manganore Iron Formation and the underlying Campbellrand dolostones (Fig. 5) (Beukes, 1983; Plehwe-Leisen and Klemm, 1995; Gutzmer and Beukes, 1996). The breccia is the result of the dissolution of the underlying manganiferous chert-rich Fairfield Formation causing the residual build-up of insoluble material that includes chert (including silicified dolostones) and a primary manganese wad which would be incorporated in the breccia as the predominant matrix (Plehwe-Leisen and Klemm, 1995; Gutzmer and Beukes, 1997). At the lower part of this breccia, near the contact with the underlying dolostones, small lenses and pods of high-grade manganese ore are found (Gutzmer and Beukes, 1997). High grade Mn ore may extend higher up within the breccia matrix and at the transition with the overlying Manganore Iron Formation.

It is because of the association with a chert-rich host that the Eastern Belt is ultimately considered siliceous in nature, resulting in braunite being the predominant manganese mineral in these rocks as replacement and/or recrystallisation product after primary wad (Plehwe-Leisen and Klemm, 1995). Other manganese minerals like bixbyite and pyrolusite have been reported albeit in smaller quantities (Plehwe-Leisen and Klemm, 1995). With respect to overall iron content, the ore shows significant variation stratigraphically, ranging from relatively more manganiferous at the base to more siliceous and ferruginous at the top as it transitions into the Manganore Iron Formation (Gutzmer and Beukes, 1996).

The bulk matrix of the breccia is reported to be dominated by quartz, hematite and braunite. However, intercalated laminations of manganiferous clays have been reported, as well as cross-cutting barite veins (Plehwe-Leisen and Klemm, 1995; Gutzmer, 1996). Crude layering is also a common feature in the ore, a texture that Gutzmer and Beukes (1996) have reported to be the result of the dissolution of chert-rich dolostones layers. A simplified stratigraphic depiction of the Eastern Belt is shown below (Fig. 5).

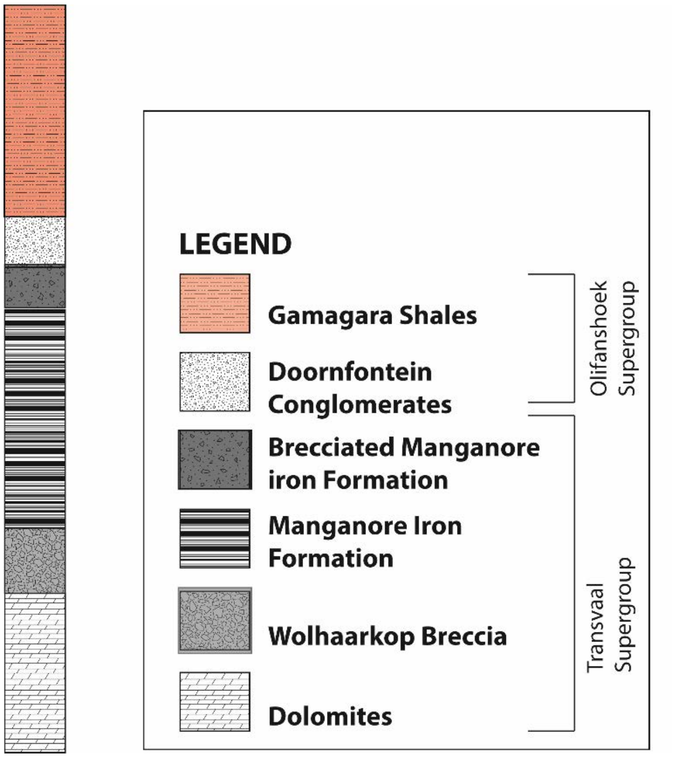

Figure 5: Simplified sketch (not to scale) of typical Eastern Belt ore stratigraphy (modified after Gutzmer and Beukes, 1996)

A mulit-stage development of how the ore formed has been described and is to date the prevailing model. The Plehwe-Leisen (1995) as well as Gutzmer and Beukes (1996) models are somewhat similar and both describe the Wohaarkop breccia as being the consequence of carbonate dissolution resulting in a chaotic accumulation of chert clasts and a manganiferous wad at the base of these sinkholes. Fluid interaction and the extensive and intensive period of erosion during the Late Paleoproterozoic are the main causes of the extent of dolostone dissolution which resulted in the formation of cavities in this part of the stratigraphy. As dissolution advanced, it left behind insoluble material from the dolostones, and the postulated primary manganese wad that settled at the bottom of the karstic sinkholes.

In a similar fashion, residual enrichment processes in a subaerial chemical weathering environment would have subjected the Kuruman BIF (Plehwe-Leisen and Klemm, 1995) to undergo extensive hematization and enrichment to form the Manganore Iron Formation, the main source of iron ore in the region (Gutzmer and Beukes, 1996; Smith and Beukes, 2016). The lithostatic weight of the Manganore Iron Formation on the already weakened substrate of weathered dolostone, would have resulted in further collapse of the cavities and subsequent slumping of the Kuruman (now Manganore) Iron Formation into the dissolution structures, a process believed to have taken place entirely prior to deposition of the overlying Olifantshoek shales (Plehwe-Leisen and Klemm, 1995; Gutzmer and Beukes, 1996). This was followed by another period of erosion which is represented by an erosional unconformity that separates the Manganore Iron Formation and the localised development of the overlying Doornfontein Conglomerate (Plehwe-Leisen and Klemm, 1995). Deposition of the Olifantshoek shales (Mapedi/Gamagara), Marthaspoort/Lucknow quartzites and ultimately the Paling shales higher in the stratigraphy (Gutzmer and Beukes, 1996) followed upon the basal conglomerate.

1.3.2 Western Belt end-member ores

The Western belt ores are reported to be more ferruginous in nature and are confined only to the central parts of the Gamagara Ridge (Plehwe-Leisen and Klemm, 1995; Gutzmer and Beukes, 1996). The ores appear tabular on an ore-body scale, and show a more direct stratigraphic association with the Mapedi/Gamagara shale of the basal Olifansthoek sequence. Texturally, the ores grade from generally massive and crudely laminated at their basal contact with the underlying dolostones, with no apparent development of a residual breccia (like the Wolhaarkop breccia). Textures of the ore grade into more laminated higher in the stratigraphy, resulting in a well-stratified and layered manganese deposit with a distinct shaly parting

(Plehwe-Leissen and Klemm, 1995). These laminations however may be disturbed or obliterated laterally, possibly due to the effects of later fluid-flow and recrystallization. Based on these varying textural observations as well as the mineralogy of the ore, Gutzmer and Beukes (1996) further divided the ore into three groups; fine-grained, laminated, apparently sedimentary braunite-patridgeite ore; coarse-grained massive to vuggy bixbyite-rich ore; and lastly, supergene altered ore composed of romanecheite, pyrolusite and cryptomelane, that would have formed at a later supergene stage. A simplified stratigraphy of the Western Belt is shown in Figure 6 below.

The origin of the western belt Mn deposits of the PMF remains a topic of debate amongst different researchers. Diverse ore-forming processes have been previously proposed, ranging from magmatic-hydrothermal (De Villiers, 1944) to fluid replacement (Hall, 1926; Nel, 1929), based on petrographic and mineralogical studies. In one of the earlier works which was based almost entirely on petrographic evidence (Schneiderhöhn, 1931) a sedimentary origin was suggested for the ores. Further models followed, which will be discussed in the following section dealing in more detail with previous studies. Neverthelss, the most popular model currently appears to agree with the sedimentary school of thought which has gained subsequent support from workers like Plehwe-Leisen (1985), Grobbelaar and Beukes (1986), Plehwe-Leisen and Klemm (1995) and Gutzmer and Beukes (1996).

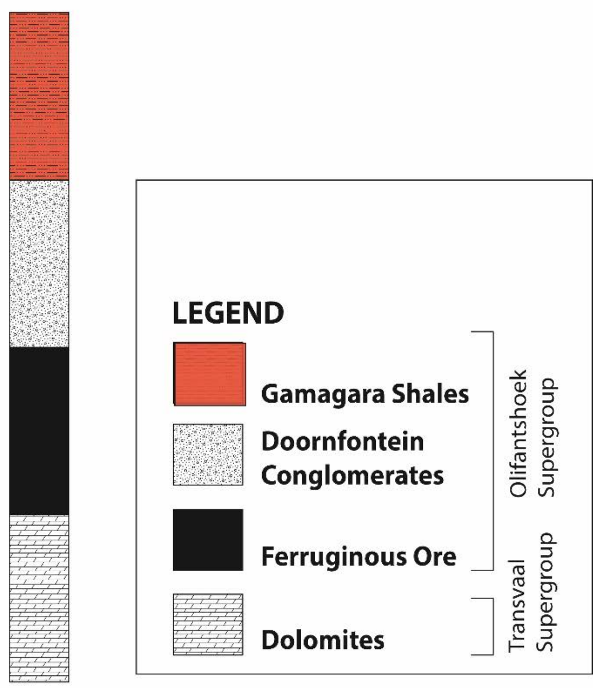

Figure 6: Simplified sketch (not to scale) of typical Western Belt ore stratigraphy (modified after Gutzmer and Beukes, 1996)

The sedimentary model as refined by Gutzmer and Beukes (1996), initially involves the development of a manganese wad at the contact with the underlying dolostone, as a result of dissolution and residual manganese enrichment of the Reivilo Formation during the karstification process. Other insoluble material that accumulated during this time would have involved hematite clasts as well as lateritic clays. This process, however, is thought to have taken place in localised aqueous environments resembling lakes, resulting in no residual breccia development but rather crude to more rhythmic deposition of layered Mn-rich material with time. Subsequent burial and diagenesis of the deposited material would have caused recrystallization of the original sediment into the present assemblage of braunite, partridgeite and bixbyite. According to Gutzmer and Beukes (1996), the lack of good preservation of the original sedimentary mineral assemblages and textures and the difficulty in distinguishing mineral species under the microscope, is a characteristic that is directly attributed to diagenetic and low-grade metamorphic overprinting. Expulsion of fluid during burial diagenesis would have led to the formation of irregular pods rich in bixbyite, ephesite and diaspore, which apparently crosscut the earlier sedimentary ores. Recent erosion and secondary karstification resulted in the exposure of the deposits to surficial conditions as well as associated supergene alteration (Gutzmer and Beukes, 1996).

1.4 Previous Studies

Hall (1926) and Nel (1929) initially proposed that the western belt Mn ores of the PMF are deposits of a replacement type, a result of replacement reactions against sedimentary clay material by manganese assemblages transported in circulating hydrothermal fluids. Hall (1926) suggested that the manganese precipitated from meteoric water (groundwater) an idea soon rejected by Nel (1929) and other geologists who favoured the notion that the source of the manganese oxides (as well as associated iron) to be the underlying Campbellrand dolostones. Visser (1944) was one of the earliest scientists to map out thrust planes within the PMF which he considered to have served as the conduits for circulating fluids. Such fluids would have acted as a solvent for the Campbellrand dolostones, as well as a manganese leaching agent and carrier to be deposited higher up in the stratigraphy (De Villiers; 1944, 1956, 1960). The fluids interacting with the Campbellrand dolostones were concluded by De Villiers to be magmatic in origin, due to the presence of B, Li, Na, Cl and F as well as the common hydrothermal textures in the ore. This notion however, is not favoured by most scientists who have opted for the metasomatic origin as initially proposed by Hall (1926),

As indicated in the previous section, Schneiderhöhn (1931) suggested a sedimentary origin for the PMF deposits, whereby the manganese was deposited as the basal portion of the Mapedi/Gamagara Formation. This would have been followed by a metamorphic overprint resulting in the presently observed mineral assemblages and textures. This idea gained a lot of support from other researchers such as Kaiser (1931), Richter and Richter (1933), Button (1986) and Plehwe-Leissen and Klemm (1985), to mention a few. A supergene model was first proposed by Du Toit (1933), whereby meteoric fluids were suggested as being responsible for carbonate dissolution and leaching of manganese which was ultimately deposited within the surrounding rocks. This supergene model is the currently favoured model, as it gained further and stronger support from, and refinement by Phlewe-Leissen and Klemm (1995), and Gutzmer and Beukes (1996). The model describes an ancient lateritic enrichment of residual manganese oxides at the expense of carbonate rocks of the Campbellrand Subgroup in the Transvaal Supergroup, subsequently modified through burial processes. Beukes (1978) further suggested that the deposition of either iron- or manganese-rich residual ore would depend on the composition of underlying dolostones, with ferruginous ores found in association with the Reivilo Formation on the western belt while the siliceous one would be associated with the chert-rich Fairfield Formation in the eastern belt.

More recently, works by Moore *et al* (2011), Costin *et al* (2015) and Fairey *et al* (2019), have exploited the occurrence and textural features of alkali metasomatic assemblages in the PMF ores. They have proposed that the circulation of hydrothermal brines has had at least some impact on manganese ore genesis, either through enhanced transport of metals (Mn, Fe) and/or through subsequent metal upgrading against an original low-Mn protolith. The latter possibility essentially brings back to the fore the earlier replacement models for the origin of the PMF deposits.

1.5 Aim of the Study

Recent studies into the PMF deposits have raised some fundamental questions about the underlying mechanisms responsible for ore formation. These studies essentially represent the re-emerging hydrothermal school of thought mentioned in the previous section and have brought about geochemical, and mineralogical evidence that challenge the current supergene model that has for so long been widely accepted for the genesis of these deposits. This whole argument therefore continues to make the PMF a hot-spot for further research, not simply in terms of the economic potential of the ores going forward into the future, but also to expand and build on the current knowledge and understanding of these deposits and therefore aid in future exploration efforts.

Moore *et* al (2011) describe and discuss the significance of the occurrence of sugilite in the Wolhaarkop breccia, an alkali-rich mineral known before from the KMF. They regard this occurrence as evidence for alkali metasomatic processes affecting the Transvaal Supergroup deposits. Other rare minerals like norrishite and armbrusterite, along with much serandite and albite, were also identified in smaller quantities filling vug spaces. Similar mineral assemblages have been reported in the Wessels mine in the KMF (Dunn *et al.,* 1980; Dixon, 1985, 1989) as well as in association with tokyoite, As-rich tokyoite and noelbensonite in exploration drillcores for iron ore intersecting Mn in the western Maremane Dome area (Costin *et al,* 2015). These studies reinforce the regional alkali-rich hydrothermal alteration event that has evidently affected these deposits. All these deposits and associated alterations are found in the vicinity of the unconformity between the Olifantshoek and Transvaal Supergroups, suggesting the fluids exploiting this unconformity to constitute a potential genetic cause for both occurrences. The presumed residual supergene nature of the Wolhaarkop breccia and associated Mn enrichments (eastern belt ores) through fresh water-dolomite interaction does not readily account for the elevated alkali content. It is noteworthy that Gutzmer and Beukes (1996) also reported the presence of alkali mineral assemblages in the PMF ores in the form of Ba-muscovite, aegirine, albite and barite, which does not satisfy the proposed fresh-water model discussed in their paper.

Further evidence supporting a possible hydrothermal interpretation of these deposits has been provided through various unpublished studies by research unit PRIMOR at Rhodes University, which stands for: Postgraduate Research (unit) in Iron and Manganese Ore Resources (PRIMOR). PRIMOR is dedicated to the study of iron and manganese deposits and their origins through the involvement of post-graduate research, and the present thesis forms another example of the activities and outputs of this unit. Selected researchers of PRIMOR have previously undertaken studies in the Transvaal Supergroup that highlight the presence of a widespread hydrothermal alteration in the Griqualand West basin and the rocks it contains. Moloto (2017) conducted a bulk and fraction-specific geochemical analysis on iron ores at the

PMF, specifically from the Hotazel and Khumani region. His study showed a distinct (although small) alkali and transition metal signal in these deposits, suggesting the possibility of a post-unconformity epigenetic hydrothermal event/s influencing iron ore formation against BIF. In a similar way, Cousins (2016) discusses HFSE enrichment and K-metasomatism in the Mapedi/ Gamagara shales of the Olifantshoek Supergroup which are stratigraphically adjacent to the PMF Mn (and Fe) ores. Cousins (2016) argues that these enrichments can only be accounted for *via* post-depositional hydrothermal event exploiting the underlying unconformity. The above results replicate and strengthen similar arguments presented in an earlier thesis by Fairey (2013), which was carried out prior to the launch of PRIMOR in 2014.

This study was motivated and spawned as natural consequence of recent results supporting a hydrothermal overprint in the Maremane Dome region, by identifying the manganese deposits of the PMF as the next suitable target. The necessity for carrying out a study of this nature is further reinforced by the evident difficulty to interpret the local stratigraphy of the manganese deposits in question. As it has hopefully become obvious from the preceding literature review of the regional and local geology, elucidating the sequence of events that led to the formation of the different deposits is hindered by obscure contact relationships between different lithologic units. This is the result of a combination of multiple erosional events and associated alteration processes, brittle deformation of many of the various rock types implicated, and fluid processes that appear to overprint a variety of possible protoliths. All these events and phenomena take place against the primary Transvaal and Olifantshoek Supergroup stratigraphies which also, until recently, were open to contrasting interpretations due to conflicting age constraints and challenging field relationships.

In light of the above facts and considerations, this study specifically targets the two belts of Mn ore (and thus ore types) present in the Maremane Dome. It uses a combination of field-work (outcrop and drillcore examination), mineralogical and geochemical analyses of samples collected from eastern- and western-belt manganese ores, and evaluation and interpretation of all the data produced, to achieve the following three main objectives:

1. To examine, compare and contrast the composition of western- and eastern-belt ores with emphasis on their geochemistry, and identify alkali overprints where present;

2. To assess whether either of the end-member types examined may require revision with respect to its genetic model, and particularly whether a hydrothermal replacement model may be applicable for either and/or both major ore types; and,

3. To constrain, if possible, whether the Campbellrand sequence of carbonate rocks remain as a potentially viable, common metal source for the formation of these manganese deposits.

The above objectives are dealt with through the thesis structure presented in the following section.

1.6 Thesis Outline

The five chapters that follow and make up the main body of this study are structured as follows: the 2nd chapter follows this introduction and is devoted to the methodology used to carry out this study as well as descriptions of the drill cores and outcrop sites selected for sampling. Chapter 3 offers a review on breccias and their origin as an essential background for some of the rock types encountered during this study. Petrographic and geochemical analysis of such breccias makes up the latter part of this chapter, in an attempt to classify these different breccias and help assess their relevance in the context of Mn ore formation at the PMF.

Petrography and geochemistry of the different ore types of the PMF, namely western belt and eastern belt ores as sampled for this study, are comprehensively presented in chapter 4. The final 5th chapter is dedicated to a detailed discussion and synthesis of the results presented in the foregoing chapters. This chapter highlights specific physical and chemical signals and attributes gleaned from this study in combination with published works, that inform the ore genesis in the PMF as well as their likely protolith where relevant. Part of the discussion involves an assessment of the Campbellrand dolostones as a viable source of metals for the Mn ores hosted within it. This is achieved through application of the so-called isocon method of Grant (1985). The chapter – and the thesis as a whole – concludes by means of offering a revised and holistic genetic model, followed by suggestions for future research work.

2 Methodology and Sampling

2.1 Methodology

A total of one field site and 4 boreholes from different localities were selected for this study (Fig. 4). The western belt manganese ore is represented by two adjacent drill cores from farm Leeuwfontein, which forms part of the Kolomela mine area exploiting iron ore near Postmasburg in the southern edge of the Maremane Dome (the Kolomela mine is owned by the company KUMBA IRON ORE, whose courtesy allowed the logging and sampling of the cores). In addition to these cores, an outcrop section located at the Bishop farm in the central Maremane Dome was also targeted for western belt ore. A drill core from farm McCarthy to the immediate north of farm Bishop, as well as one from the nearby Khumani iron ore mine operated by ASSMANG Ltd, represent both eastern belt ore. The drill cores from Leeuwfontein and Khumani were selected for analyses in part because the operating companies kindly disclosed to the author and her supervisor, the high manganese enrichments recorded in the respective rock intersections. Specifically, bulk-rock assays from KUMBA IRON ORE indicated the Mn values to be in the range 11.11 - 52.81 w% in drill core LF391, while drill core LF393 showed a range between 10.31 to 36.66 wt %. Similarly, high values are present in the drillcore from Khumani mine. Finally, drillcore from McCarthy farm was kindly provided access to by consulting exploration company OREX based in Kuruman.

The above drill cores were sampled, resulting in a total of 36 samples used for the mineralogical and geochemical analyses of this study. The selection was made in such a manner that captures sufficient lithological or compositional variability for the purposes of this study; the samples represent effectively eastern belt massive ore and associated breccias; western belt laminated and massive ore; and a small selection of Campbellrand dolomites.

A combination of bulk-rock and mineral-specific analysis techniques were applied on the collected samples. Bulk rock mineralogy and bulk geochemical compositions were obtained through x-ray diffraction (XRD) and x-ray fluorescence (XRF) techniques, both typically conducted on pulverised rock samples. The XRD analysis was conducted at the Rhodes University Chemistry department while pulverised samples were sent to Stellenbosch University for further processing (production of fused glass beads) and bulk rock geochemical analysis using x-ray fluorescence analysis to determine their major and trace chemical compositions.

Mineralogical and petrographic descriptions and analyses were achieved through the means of transmitted and reflected light microscopy, Scanning electron microscope-energy dispersive analyses (SEM-EDS) and electron probe microanalyses (EPMA). The transmitted and reflected light microscope was used mainly for basic textural descriptions, and mineral identification using basic optical properties, where this was possible by virtue of the very fine size of minerals. The SEM-EDS and EPMA were used in instances where mineral identification through the use of the microscope was unachievable due to the very fine-grained texture of the sample. Detailed descriptions of the instrumental settings and instrument specifications can be found in Appendix A. For microscopic investigations, SEM and EPMA analysis, brecciated and laminated samples were cut into polished thin sections while for samples representing massive ore, polished round blocks were used. Corresponding powder samples were also crushed for further analysis through the XRD technique (see Appendix A). The sample lithologies and locations are displayed stratigraphically beside their corresponding logs.

2.2 Drill Core Descriptions

Drill core and hand specimens have been grouped below according to the locality from which they were obtained in the study area of the Maremane Dome. Description of the drill cores and outcrop gives a clearer field and stratigraphic context of the localities selected for sampling and displays where possible the relationships between the different lithologies targeted. In most instances however, the extraction of such relationships on core intersections was very challenging and was largely inferred rather than determined.

2.2.1 Leeuwfontein Farm (Kolomela Fe ore mine, southern Maremane Dome)

Drill Core LF391

Two drill cores from the Leeuwfontein farm namely LF391 and LF393, were identified and selected to represent the typically ferruginized western belt ore as known to occur in the Maremane Dome. Beginning with intersection LF391, it represents a total of 61.8 meters of core which consists broadly of Campbellrand dolostones at the base, followed by red shales that were interpreted to belong to the Mapedi/Gamagara Formation, and ultimately various textural sub-types of massive, ferruginous manganese ore (Fig. 7).

Zooming in, the Campbellrand dolostones intersection extends for about 7 meters and grades into a brecciated ferruginized red shale zone. Red shale directly overlying the dolostones is atypical of the local stratigraphy of the PMF and therefore suggests that if it is part of the Mapedi/Gamagara Formation of the Olifantshoek Supergroup, it indicates an unconformable contact or a tectonic one. The latter seems favourable as it would also explain the intense brecciation associated with this zone.

Massive, fine-grained, laminated and dominantly black manganese ore with small chert fragments, overlies the aforementioned shale. The manganese ore gradually transitions upwards into an apparently more shale-like zone, which is completely free of fragmentary material; this extends for about 14 metres. Above the manganiferous shale rests again another portion of shale which may also stratigraphically be considered as part of the Mapedi/Gamagara Formation, through a relatively sharp contact (Fig. 7). At the top of this shale intersection, there is the occurrence of apparent agglomerate (breccia) of manganese-rich shale which marks the end of drill core LF391. Sampling positions are indicated against the log shown in Figure 7.

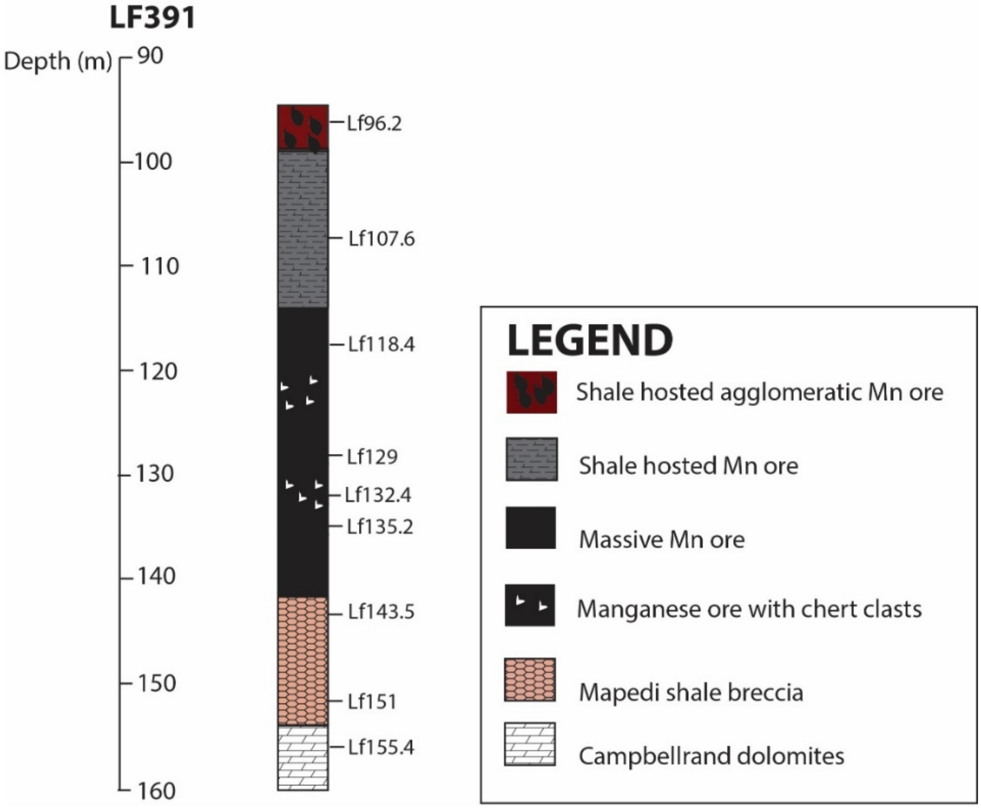

Figure 7: Stratigraphic log of drill core LF391

Drill Core LF393

Figure 8 shows the log and sampling positions of approximately 50 meters of diamond drill core LF393 which also captures Mn ore and associated lithologies of western belt-type manganese deposits. This drill core correlates closely with the LF391 drill core described above with the exception of the apparent Mapedi/Gamagara shale overlying the Campbellrand dolostones which in this drill core is not brecciated. A sharp contact exists between these red shales and overlying massive manganese ore at about 144 m. The ore is generally massive with two exceptions, both recorded at approximately 128m and 121m within the ore zone. At 128m, about 4m of agglomerated red shale occurs that appears to be comparable to similar lithology in drillcore LF391. Over the interval 121m to 119m within the same ore intersection one observes alternating layers of apparently Mn-poor shale and manganese-rich material. The rest of the core can be adequately characterised as structureless, massive manganese ore.

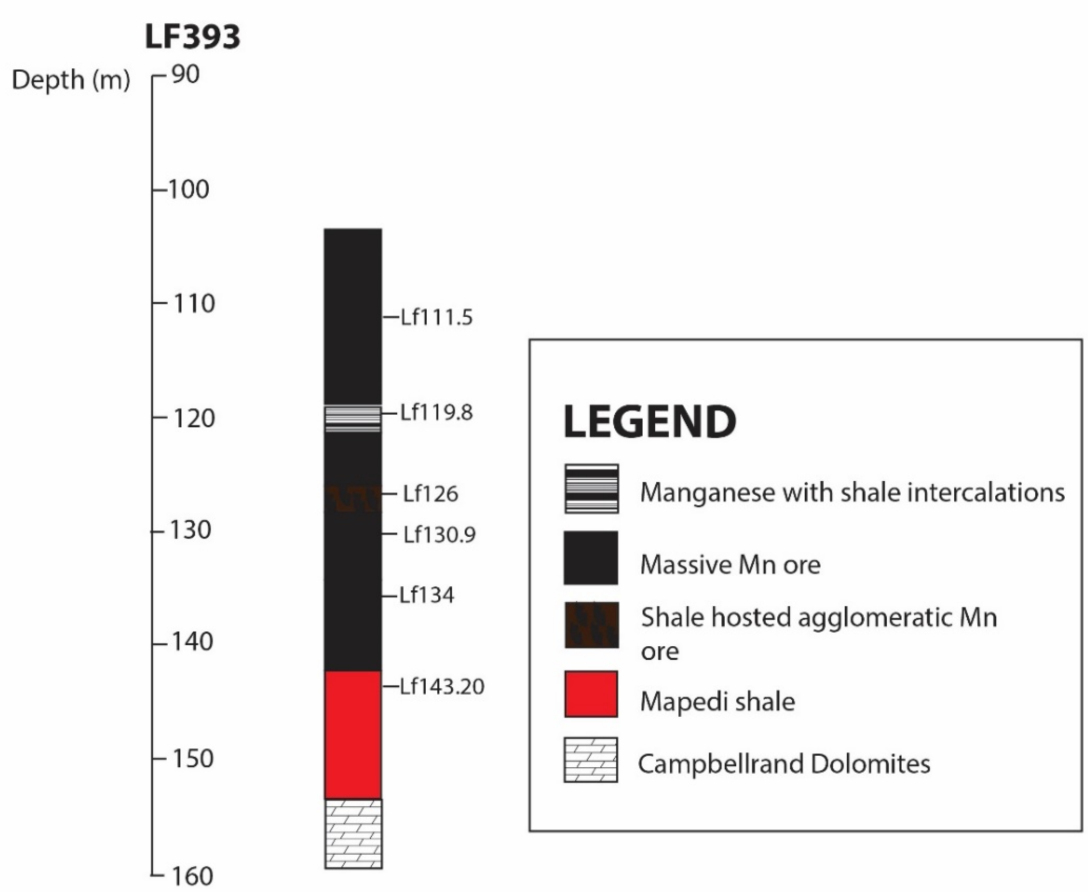

Figure 8: Stratigraphic log of drill core LF393

2.2.2 McCarthy Farm: eastern belt manganese and associated iron ore

Drill core MC35

Drill core MC35 straddles depths below surface from 111m to 20m; this part was obtained through diamond coring whereas the top 20m were percussion-drilled. This allowed for 91m of the stratigraphy to be logged and sampled. The core was presented by the consulting geologists of OREX as typically capturing a section of eastern belt Mn ore. The first 5.57 m of the drill core from the base upwards represents a reddish shaly zone which is inferred to form part of a continuum with the manganese-rich zone above it. This shaly interval appears to be iron-rich and contains chert clasts within parts of it. These clasts wane in abundance over the interval 99.5 m to 94.9 m and re-appear once more over about 7.6m before the transition into a manganese rich zone with a macroscopically similar shaly appearance.

The manganiferous material here is soft, friable and easily falls apart at planes of apparent parting, suggesting a likely supergene weathering overprint by low-temperature meteoric fluid circulation. Chert clasts however are also present, and can be observed between 87.3m to 81.7m where brecciation is developed. The manganiferous shale transitions into a red shale, and crude bands of chert clasts can be seen throughout the red shale, alternating with chert free zones as indicated in Figure 9. These chert-rich zones effectively represent brecciated domains within the red shale.

A clast-supported breccia is encountered at around 61.2 m before becoming more matrix supported at around 50.6m. At 38.6m the clast sizes seem to increase from mm- to cm-scale up to the 50.6m depth. The clasts are a creamy to white colour and are angular to sub-angular in shape. At the depth of 61.2m, the clast colour becomes a mixture of white and grey, and one can observe traces of flaky hematite – described widely in the literature as specularite – surrounding the clasts. The clasts become fewer upwards, and some distinctive veins are encountered at around 42.25m. This zone with secondary veining was avoided during sampling as it likely represents much younger fluid circulation effects and would therefore compromise bulk geochemical homogeneity.

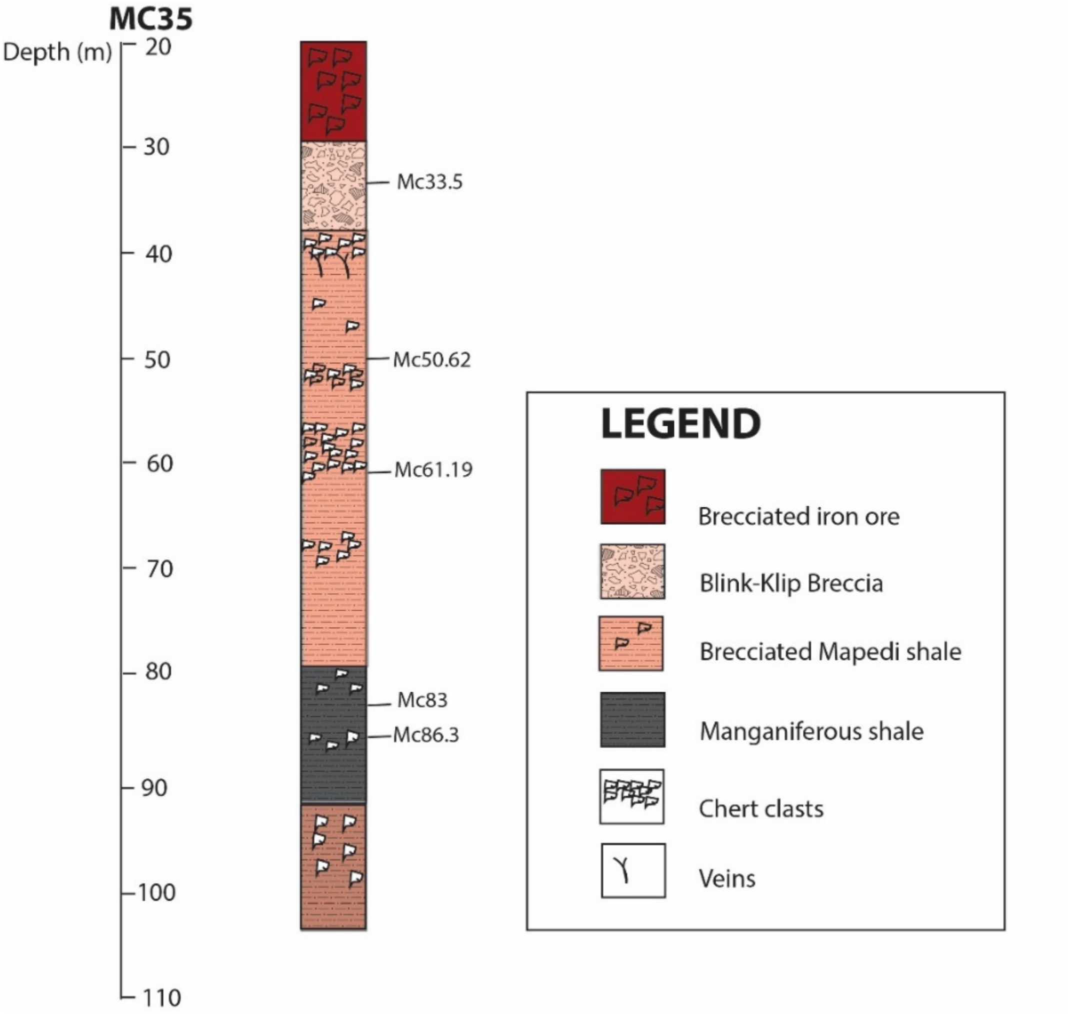

Figure 9: Stratigraphic log of drill core MC35

An iron-rich polymictic breccia described in the relevant literature as the Blinklip breccia, overlies the shale zone from 33.50m and extends for a further 3.80m; this breccia rests above the shale-hosted breccia. It is essentially a ferruginous, BIF clast-supported breccia hosted in a dull grey fine-grained hematitic matrix and is closely associated with massive iron ores in the region (Smith and Beukes, 2016). The contact between the Blinkklip and the underlying shale-hosted breccia is a gradational one. The gradational change is first observed through the change in clast composition which transitions from being quartz-dominated to BIF-dominated (37.42m). This is soon followed by a matrix compositional change at about 38m where it changes from the typical red shale lithology to a hematite rich matrix highlighted by (Fig. 9). This is the overlain by massive, breccia-textured hematitic iron ore (not sampled), up to the upper end of the core at 20m.

2.2.3 Khumani Mine: eastern belt manganese ore

Drill Core WK4/25

This drillcore was permitted to be accessed courtesy of ASSMANG Ltd that exploit iron ore at Khumani mine. Twenty-seven meters of core were logged, ranging from 14.8 m to 114.8m. This drill core captures essentially two key lithologies, namely the Wolhaarkop Breccia as well as massive iron ore of the Manganore Iron Formation. The contact between the two lithologic entities is almost impossible to locate, as it is extremely gradational.

The lower portion of the core from the base upwards represents the classic chert-rich breccia known as the Wolhaarkop breccia. The chert clasts are set in a fine-grained matrix with a fairly consistent colour and appearance throughout the drill core. The clasts in this zone are mainly angular in shape though the much smaller ones can be sub-angular to sub-rounded. Their colour ranges from creamy white to a greyish white, but some clasts show reddish iron staining suggestive of superficial iron oxide coatings developed upon some clasts.

The bulk of the Wolhaarkop breccia intersection is typified by a chaotic distribution of clasts over most part (135.3-124.4m) with individual clast sizes fluctuating in size from mm-scale up to several cm across (Fig. 10). This massive matrix-supported breccia shows some crude layering in parts as well as the presence of distinct reddish mudstone/shale intercalations at around 135.2m. The matrix takes on a dull grey to black colour and shows occasional reddish staining. In the absence of large clasts, fine, random mm-scale chert disseminations is seen within the dark matrix. At 121.8m, the clasts seem to aggregate into apparent banded assemblages of a thickness of about 1.5 to 2 cm each, alternating with clast free manganiferous material (Fig. 10).

It is precisely at this point of the intersection where the Manganore Iron Formation is expected to overlie the Wolhaarkop Breccia through a highly gradational transition. In this instance however, the material is strongly manganiferous and therefore represents a mixed kind of mineralisation with high iron oxide abundance accompanied by much manganese. In chapter 4, details on the exact composition of this material will be presented and evaluated. It should be noted that although chert clasts effectively disappear in this part of the intersection, they continue to be occasionally present, floating in the ferro-manganiferous matrix.

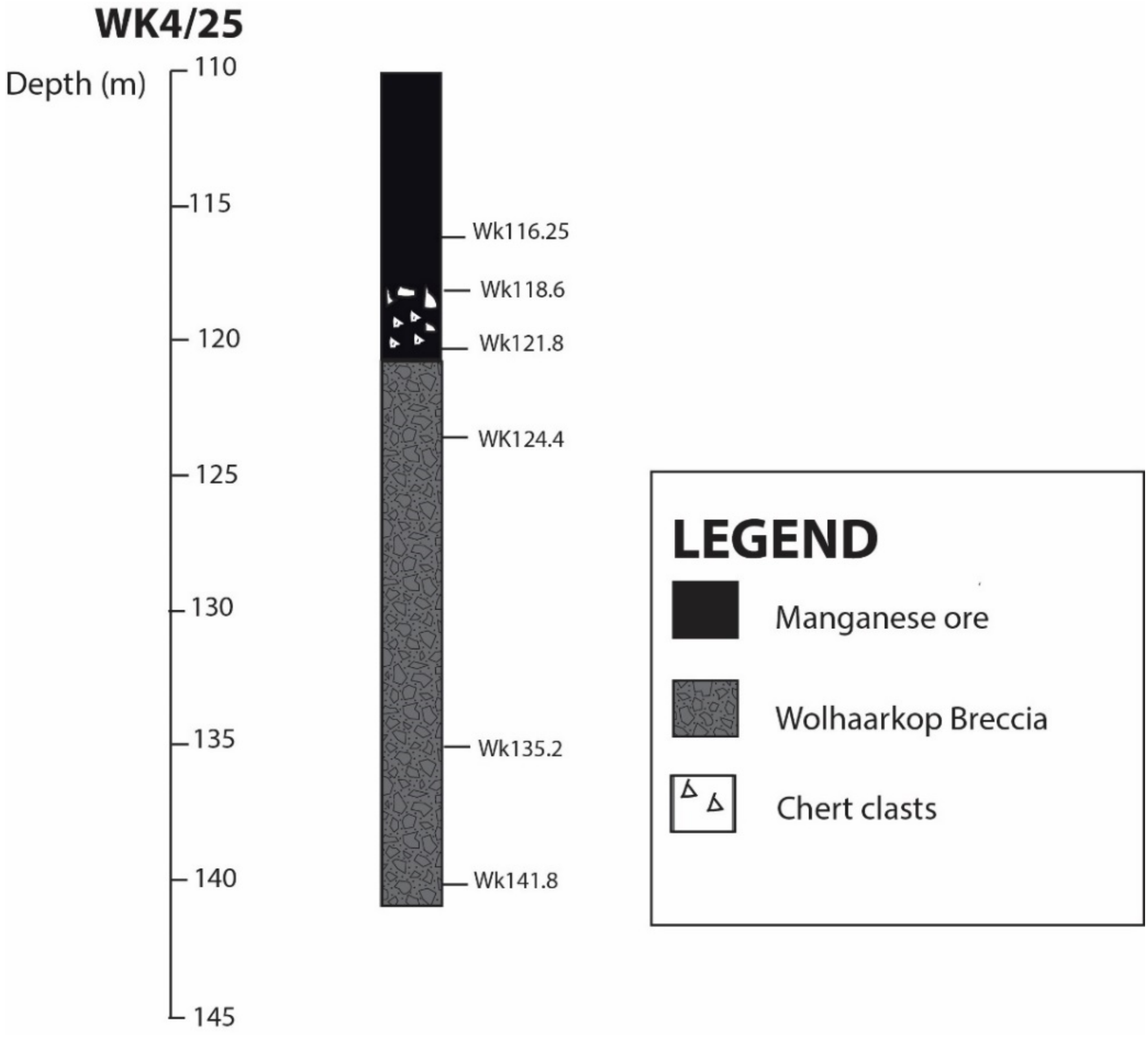

Figure 10: Stratigraphic log of drill core WK4/25

2.2.4 Bishop Outcrop

Sampling at the Bishop farm locality in the central Maremane Dome area was performed at two scales: on a larger scale, an outcrop section was selected and sampled at a dm interval (Fig. 11). In addition to the outcrop section, an individual sample from an adjacent outcrop containing very well-laminated ore was collected, as it permitted sampling at a much finer scale on a band-to-band basis. This kind of sampling permits any small-scale variability within the ore to be examined and assessed (Fig. 12).

The Bishop outcrop section sampled is approximately 150cm and shows typical eastern belt ore in massive form dipping gently southwards. Texturally, the ore shows an apparent shaly appearance with well-developed cleavage resulting in parting of the ore along its planes. The ore is invariably massive to laminated in appearance, with the laminations ranging from laterally continuous to contorted and brecciated. Of special interest in the laminated ore is the occurrence of intervals of intercalated shale horizons. Sampling was done at variable intervals (Fig. 11) in order to incorporate all lithological changes within the outcrop, including the shale intervals themselves. The first sample was collected at 30cm from the ground perpendicular to strike, followed by samples at 70cm, 89 cm, 122cm as well as 152 cm. The shale intercalations were sampled at 80cm and 89cm, with the latter sample incorporating also the enclosing Mn ore.

More samples to represent this ore were obtained from a drill core from Leeuwfontein, a farm located in the western part of the Maremane dome as well.

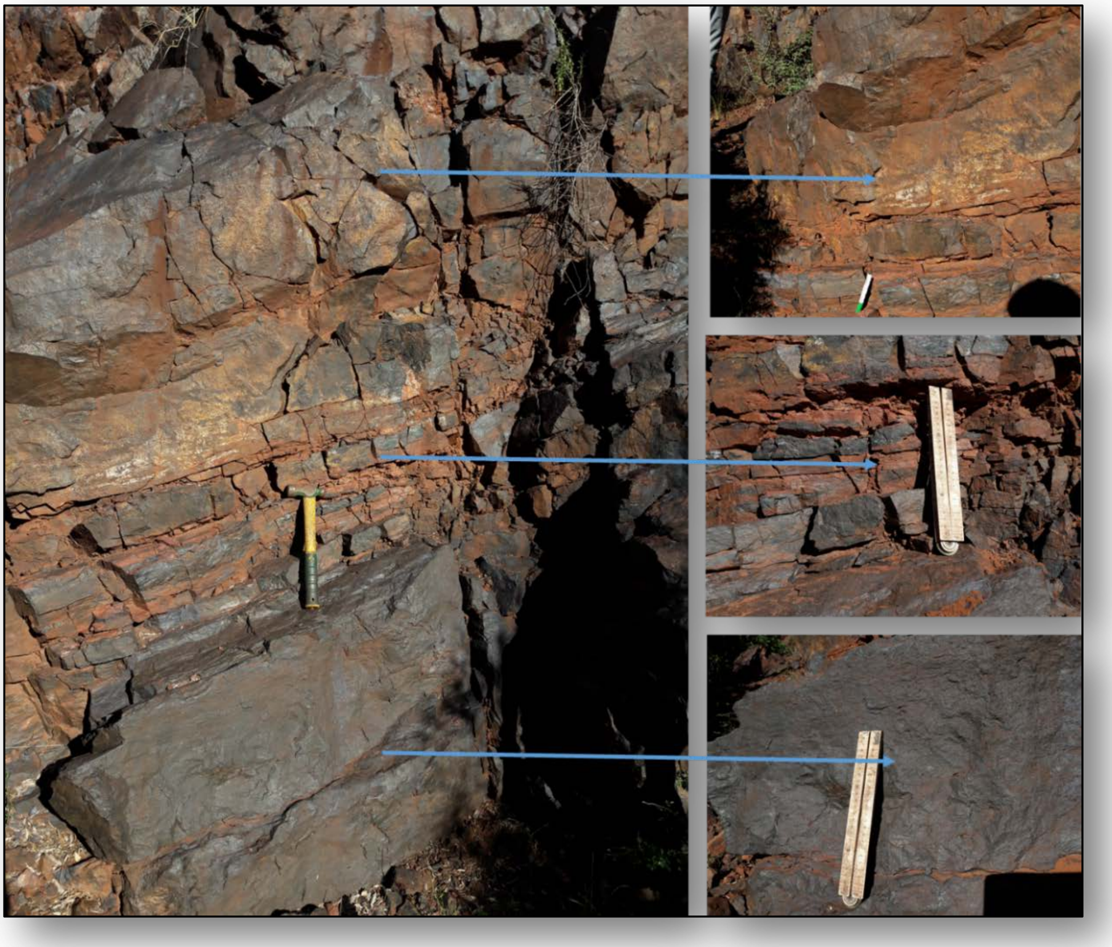

Figure 11: Bishop farm outcrop sampled at dm-scale intervals for petrographic and geochemical analysis.

The hand specimen collected was sampled from a similar adjacent outcrop and was in turn sampled at variable intervals to address the different lithological changes on a finer scale. As can be seen in Figure 12, five domains were subdivided, with the bottom (E) and the middle (C) of the specimen showing a well-developed laminated texture and fine intercalations of unmineralized shale and manganese ore, while the rest of the specimen was dominated by massive to crudely-laminated manganese ore.

As it will be shown later in this thesis, the outcrop samples of manganese ore and those obtained from the individual samples from the hand-specimen, were treated separately, but also together as an overall dataset representing typical western belt manganese ore.

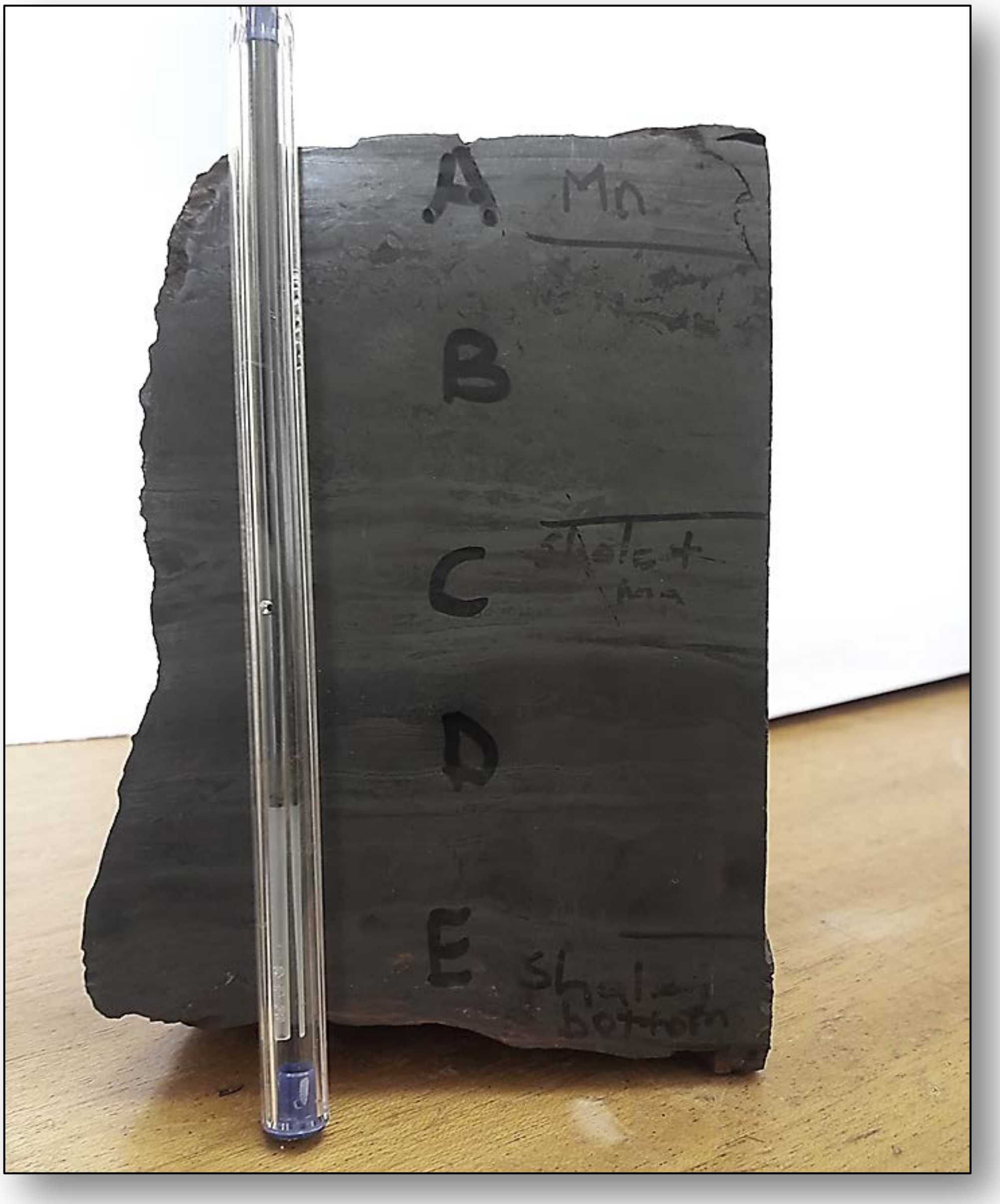

Figure 12: Hand specimen collected from farm Bishop sub-sampled at a smaller scale to allow assessment of corresponding mineralogical and chemical variability.

3 Breccias: a review

3.1 Introductory notes

The Postmasburg Manganese Field as elaborated in the previous chapter constitutes a key geographical region globally in the context of manganese metallogenesis and exploration, as it is host to large economic manganese and iron deposits (Astrup and Tsikos, 1998). Studies on the geology of the region have also revealed the presence of abundant breccias which nevertheless pose major challenges to research and industry geologists alike, due to their often enigmatic origins and irregular distributions across space. Some of the same breccias however, are also mineralised with respect to iron and manganese and therefore have great potential to inform not only geological processes of formation but also those of ore genesis.

Despite the dominance of these rocks and their significance as manganese and iron hosts, very little is understood about their origin and formation process. Previous studies have identified, documented and discussed mainly two major types of breccias in this region; the manganiferous chert breccia known as Wolharkop breccia (Boardman, 1964; Grobbelaar and Beukes, 1986; Plehwe_leisen and Klemm, 1995; Gutzmer and Beukes, 1996) as well as the iron rich, polymictic, BIF hosted breccia, known as the Blinkklip breccia (Plehwe-Leisen and Klemm, 1995). A thorough understanding of these types of rocks is thought to be crucial in better discerning the geological history of their occurrences, locally and regionally, a goal that can be at least partly achieved by constraining the type of breccias these are with respect to breccia-forming processes.

There is a plethora of breccia types that have been studied across the globe, which range from seismic, fault, collapse, chert and impact breccia to mention a few, all of which inform the geological environment and conditions in which they formed. For this particular study, this section will provide a review on breccias with focus on only three breccia types that have the highest probability of forming in this type of geological environment. It would, for example, be somewhat frivolous to discuss seismic breccias in an area that is by and large sedimentary in nature with no recorded history of any major seismic activity. Therefore, after thorough research into various breccia types documented in literature, the most likely types to characterize the PMF have been reduced to the following three types: dissolution, chemical and evaporite breccias. Carbonate breccia, despite their probability of forming in this region as they have been reported to form in karstic environments (Madden *et al,* 2017), have not been included in this review as they were not encountered during the field component of this study.

Breccias constitute the few geological structures that lend themselves to diverse interpretation, as any given type of breccia can be interpreted differently by researchers from different fields. This has therefore caused a lot of contention in finding a definition that caters for all fields of study into these rocks. The assortment in ideas and interpretations is partly due to the large number of processes contributing to the physical fragmentation of a lithology and the processes of assembly of rock fragments that are finally cemented into breccia (Norton, 1917). Despite all these nuances, many researchers still opt for the segregatory approach that attempts to describe breccias as either sedimentary or igneous, an approach which often sidelines other fields like structural and economic geology. The tectonic and economic importance of breccias, has also sparked further great interest beyond the sedimentology and igneous field that makes them of equal pertinence and geological importance to structural and economic geologists alike (Taylor, 2009). Due to this broad developing interest, and the occurrence of breccias in diverse geological settings – exogenic and endogenic – as well as their association with different ore types (Reimold,1998; Shukla and Sharma, 2018), attempts have been made in the past to find an all-encompassing definition and to classify breccias into different types (Laznicka 1988; Reimold 1998).

Laznicka (1988) attempted to categorise the different breccia types based on their metallic assoications, while Jèbrak (1997) discussed eight different types of breccias emphasizing mainly tectonic, fluid-assisted and wear-abrasion breccia-forming processes as the most common, especially in vein-type deposits. Others like Lawless and White (1990), have also attempted to classify breccias based on epithermal-mesothermal fluid-related processes, an idea inspired by the common and close association between brecciated host rocks and epigenetic precious and base-metal mineralisation. They grouped these into 7 classes, with further sub-classes emanating from them. These classification attempts have however proven largely unsuccessful due to a dearth of distinct diagnostic signatures as well as a lack of genetic associations which have not been well defined (Norton, 1917; Laznicka, 1988).

For the purpose of this thesis, the general definition used by Shukla and Sharma (2018) will be used as it has no obvious bias towards a specific geological field but rather provides a descriptive framework of essentially what a breccia is. They have described a breccia as a "rock that consists of mineral or broken rock fragments, often angular, cemented in a fine-grained matrix which may or may not be of similar chemical composition to the rock fragments". Another rock type that can be easily confused with a breccia is of course conglomerates, a rock type also present in the PMF in the form of the Doornfontein conglomerates found further up in the stratigraphy (Plehwe-Leisen and Klemm, 1995).The fundamental difference between a breccia and its counterpart, the conglomerate, lies in the shape of their clasts. The former has very angular clasts while the latter's clasts are by definition sub-rounded to rounded. It should be stressed here that Shukla and Sharma (2018)'s definition is quite different from that of authors likes Bates and Jackson (1987) who tended to associate breccias with a strictly sedimentary origin by defining them as "clastic", a statement opposed by Laznicka (1988) who emphasizes the stricter origin of conglomerate as clastic rocks, whereas such definition cannot be applied universally to breccias.

As mentioned in the introductory chapters, the omnipresent breccia in the eastern belt of the PMF is the Wolhaarkop chert breccia. This breccia is evidently a central component in mineralised manganiferous rock successions of the eastern belt and is therefore an obvious breccia type to focus on first as part of the following review.

3.1.1 Chert breccia

Traditionally, chert breccias were described as autoclastic breccias in which both matrix and clasts are dominated by microcrystalline quartz (Fairbridge, 1978). Chert, however, often contains impurities such as carbonates and iron oxides (Bates and Jackson, 1980), therefore these constituents too can form part of the resulting breccias. Chert has commonly been found in association with carbonate sequences (Shukla and Sharma, 2018) as has been documented in the Klipfontein Formation of the Campbellrand Group in South Africa, as well as the La Silla Formation in Argentina (Shukla and Sharma, 2018).

In places like Israel, specifically the Mishash Formation, these chert associations have been found to be a result of replacement of carbonate rocks, a process indicated by the abundance of replacement textures as well as ubiquitous silica in the rocks (Kolodny *et al,* 2005). An abundance of interlayered sequences of chert and carbonates prior to brecciation is therefore inferred. The Amman Formation in Jordan, an equivalent of the Mishash Formation, has been described to form this conspicuous feature as it too consists of chert layers alternating with chalk and limestone beds, overlain by phosphate-rich rocks (Kolodny *et al*, 2005). It is these chert layers that have drawn the attention of many geologists who have described and documented different chert types in attempts to understand their occurrence and resulting breccias (Blanckenhorn, 1914; Lees, 1928; Picard, 1931).

Brecciation of such chert layers can be a result of a number of processes, the most common being dissolution of the underlying more soluble rocks (Kolodny *et al,* 2005; Shukla and Sharma, 2018), a process simply known as dissolution collapse. Other processes that cause chert fragmentation are tectonic disturbances (Kolodny *et al,* 2005; Shukla and Sharma, 2018), high pore-fluid pressure (Harper and Tartarotti, 1996; Lees, 1928) and dehydration (Picard, 1931) to mention a few.

3.1.2 Evaporite Breccia

Evaporite breccias are a type of dissolution or collapse breccia formed by gravitational fragmentation caused by the dissolution of underlying strata (Friedman, 1997), specifically the dissolution of evaporites like gypsum, halite and anhydrite (Stanton, 1978).

The origin of evaporite breccias and collapse breccias in general is not always obvious and often hard to decipher especially in the case of evaporites. This is mainly a consequence of a lack of direct evidence for the existence of former interlayered evaporites, resulting in their prior existence being inferred based on the presence of preserved subsurface evaporites (Swennen *et al,* 1990). This has resulted in collapse breccias being assigned different formation processes by different researchers, an example of this being the Bear Rock Formation which has been described as either tectonic, dissolution-collapse or as a result of rock expansion due to anhydrite hydration (Friedman, 1997).

The difficulties often arise from the different considerations that need to be made when one classifies an evaporite breccia in order to determine its mode of formation. These include the type of fluid responsible for dissolution, depth of burial, as well as the age of the karstic system and brecciation (Eliassen and Talbot, 2005). All of these features can potentially be interpreted differently per researcher, due to factors like sampling bias, method used for sample analysis and so on.

However, some textural characteristics set evaporite breccias apart from other breccia groups, some of which include a matrix made up of insoluble material like mud, silt, chert, detrital quartz, clay, and dolomite. The breccia fragments on the other hand depend on the collapsing overlying strata or the host in which the evaporite layers were intercalated. Evaporite breccias tend to exhibit pseudomorph textures of dissolved evaporite minerals like anhydrite and gypsum (Friedman, 1997; Warren, 1999); some of these can be replaced or filled by calcite, silica and/or dolomite (Warren, 1999). Some of the evaporite breccias are commonly defined by gradual contacts with the overlying strata, while the lower contacts are usually much sharper. This is for example the case with the Belle Roche breccia in Belgium (Swennen *et al,* 1990; Warren, 1999), breccias of the Minkinfjellet and Wordiekammen Formations in Svalbard, Norway (Eliassen and Talbot, 2005), as well as breccias from the Madison Group in Montana (Middleton, 1961).

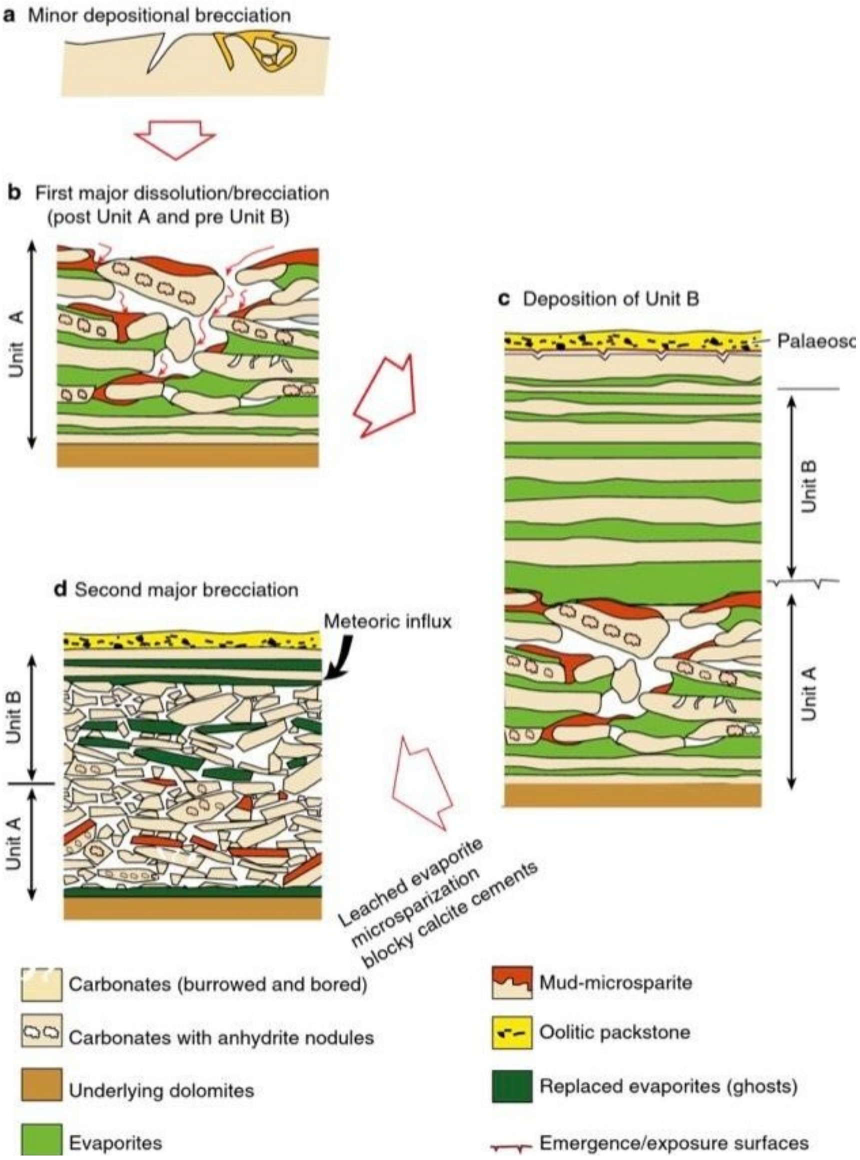

Figure 13: Sequential brecciation of the lower Visean Belle Roche breccia (after Swennen *et al,* 1990 and Warren, 1999). Note in (d) the discontinuous clast laminations. The brecciation process was described as foundering instead of a collapse mechanism, and hence stratigraphic order was retained.

Crude stratification is also an indicator of a once existing evaporite layer that has since been dissolved, often distinguished by semi-continuous clast layers within the breccia (Swennen *et al,* 1990). These crude stratification features have been variously observed and discussed for a number of evaporite breccias including the lower Visean Belle Roche breccia (Fig. 13). Chemically, evaporite breccia are often characterized by alkali enrichments. The Belle Roche breccia mentioned earlier is no exception, as it is characterised by enrichments in Mg, Sr, Na as well as Fe and Mn. This comes as no surprise, as the main mineral components of evaporites as identified by Bąbel and Schreiber (2014) typically include salts of Na^{+}, K^{+}, Mg^{2+}, Ca^{2+}, Sr^{2+}, Al^{3+} as well as Fe^{2+}. The anionic complexes are most commonly Cl^{-}, SO_4^{2-}, HCO_3^{-}, Br^{-}, I^{-}, F^{-}, $B_4O_7^{2-}$ and NO_3^{-}.

3.1.3 Chemical breccia

A process that still raises considerable debate around it as a mechanism for brecciation, is the so-called chemical brecciation. This process has been used to explain the formation of breccias that do not necessarily fit into the more common causes of breccia development such as tectonic, dissolution collapse and volcanic activity (Sawkins, 1969).

It seems however, that brecciation is not merely a result of pronounced physical processes as has been argued by earlier workers like Bryner (1961) and Sawkins (1969). The former suggested that a lot of the breccias associated with porphyry copper-type ore deposits are associated with the passage of hydrothermal solutions through these rocks derived from deeper magmatic sources. Although no sign of porphyry-type magmatic activity is evident in the PMF, one cannot discount the possibility of hydrothermal fluids of other origins passing through the region may have resulted in fluid-rock interactions which can not only potentially alter the chemistry and mineralogy of the interacting rocks but also cause physical breakdown of the host rock. Hydrothermal fluids also result in mineralization within crevices and fractures of the rock, a process which can also ultimately lead to brecciation. This process was first termed mineralization stoping by Locke (1926), a researcher who represents one of the earliest proponents of the chemical brecciation school of thought.

Brecciation evidence and its attribution to a possible source can be quite a challenging task, as a wide variety of processes can likely produce similar brecciation styles. It is however, the attention to fine structural, chemical and mineralogical detail that can permit one to constrain that one process bears more weight over the other, especially when it comes to deciphering chemical brecciation processes. Sawkins (1964), for example, observed jigsaw-like pyrite fragments in a chalcedony-infilled vug from the Salaverna region. This could be interpreted as a result of either two processes; replacement veining of pyrite, or the wedging apart of pyrite due to infilling chalcedony. The jigsaw geometry of the fragments does not favour the replacement as they fit together like a puzzle, indicating that they were simply "pulled apart" or separated from each other by the introduction and infill of the chalcedony.

Further examples of chemical brecciation have been attributed to expansive forces on clasts as has been observed by Brockie *et al* (1968) on the Westside-Webber deposits. They observed a 3D movement of chert clasts from the original chert lens, indicating an internal force as opposed to an external one responsible for the chert break-up. Their suggestion went against the main school of thought about the formation of these breccias which suggested collapse as the brecciation mechanism. Another inconsistency with the collapse mechanism in these particular deposits as put forth by Sawkins (1969) is the extreme angularity and intimate association of the clasts which cannot be explained by the downward settling of a bed at a distance of 10 metres (Fig. 14).

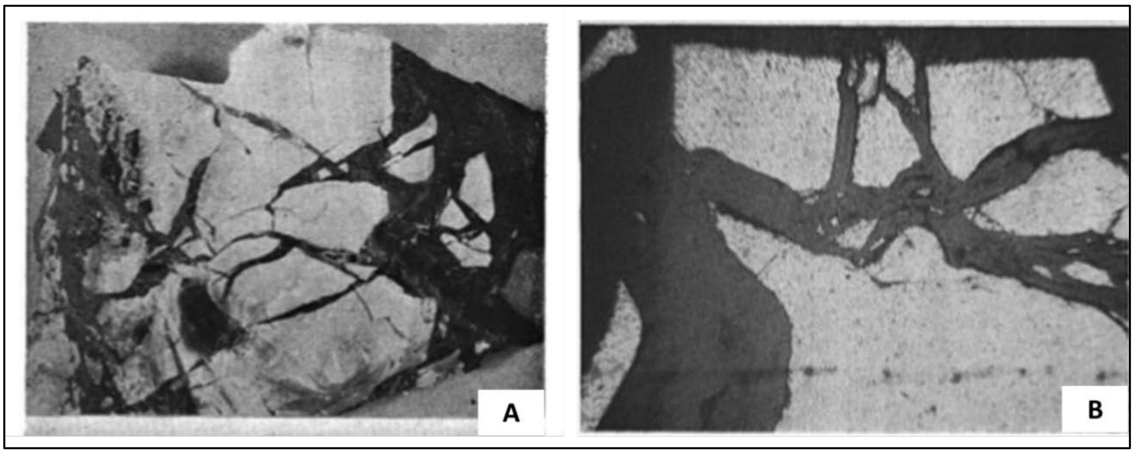

Figure 14: A. Brecciated sedimentary chert showing outward movement of breccia fragments in all directions (Sawkins, 1969) **B.** Sample showing expansive brecciation. The jig-saw aspect of fragments proves that this not replacement veining (Sawkins, 1969).

From the foregoing, it follows that chemical brecciation can be attributed to mainly two factors: fluid-rock interactions, which have the potential to weaken the rock especially if the fluid is alkali-rich (Hadley, 1961); as well as expansive forces, which break the rock perpendicular to fracture ingress or crack infill. The circulation of these hydrothermal fluids, produces physico-chemical changes in the rocks through which they circulate, resulting in chemical reactions through processes of dissolution and precipitation of new mineral assemblages (Pirajno, 2009).

Based on the controlling factor being the operation of fluid-flow through the rocks, which can result in either or both the above outcomes, it seems as though chemical brecciation could be more common than initially believed, and merits wider consideration when dealing with breccias.

3.2 Breccias in the PMF

As previously mentioned, two major breccia types have been studied and documented by different workers in the PMF region, and those are the Blinkklip breccia and the Wolhaarkop breccia, although there is very limited literature on the former. However, during the course of this study, one more type of breccia, namely a shale-hosted breccia, was encountered in both the drillcores from Leeuwfontein (Kolomela mine) as well as the drillcore from farm McCarthy. This prompted an additional interest in analysing these breccias as well, both mineralogically and chemically, so as to elucidate their origin. The following section provides a relatively basic, descriptive account of these breccias as encountered in this study, by means of standard observations and petrography enriched with standard geochemical analyses. This was done as a means of offering a resource to future researchers in the PMF and as introductory background for the manganese mineralisation associated with them that will be covered in the next chapter.

3.3 Petrography and Mineralogy

Petrographic and mineral-specific analytical work has been conducted on 11 polished thin-sections of breccia samples. Of these, four came from red shale-hosted breccias, two from the Blinkklip breccia, and the remaining five from the Wolhaarkop breccia. For geochemical analysis, the matrix was separated from the clasts and each were analysed separately with the exception of the Blinkklip breccia. As indicated earlier, the Blinkklip breccia is essentially clast-supported and has little to no matrix to be analysed. The clasts themselves are mostly apparent fragments of BIF that have been evidently replaced by hematite, which therefore results in a very iron-rich geochemical signature (~60 wt% total iron oxide) and the remaining component of the rocks being made up almost entirely by silica (38 wt%). The chemical and mineralogical simplicity of the Blinkklip breccia meant that bulk geochemical and observations had low potential to offer further insights into ore formation. The shale-hosted breccia and Wolhaarkop breccia clasts were also effectively dominated by chert and therefore also offer little from a geochemical viewpoint. Therefore, considerations were made only on the sub-sampled matrix from both of these breccias.

It must be stressed here that due to the direct metallogenic connection between the Wolhaarkop breccia and eastern belt manganese ore associated with it, it was decided that the results of the Wolhaarkop Breccia will be discussed in direct context of the manganese ores dealt with in the next chapter. Therefore, this chapter will terminate with descriptions of the Blinkklip and shale-hosted breccia as encountered in this study, whereas the Wolhaarkop Breccia will essentially constitute the link between this chapter and the next one in a kind of conceptual "continuum".

3.3.1 Blinkklip Breccia

The Blinkklip breccia is reportedly confined only to the eastern belt of the Maremane Dome (Plehwe-Leissen and Klemm, 1995). Very little work has been done on this iron-rich breccia type, probably due to its largely bimineralic nature (predominantly hematite and lesser quartz) and simple chemistry, which together do not offer much information to allow investigations about its origin on the basis of standard petrography and geochemistry.

Figure 15: Drillcore images from farm McCarthy containing eastern belt Mn ore , shale-hosted breccia and the Blinkklip breccia. **A.** The red square marks the occurrence of the Blinkklip breecia as well as its transition into the red shale-hosted breccia in drill core MC35; **B.** A typical hand specimen of the Blinkklip breccia.

Previous studies have stratigraphically placed the Blinkklip breccia to occur above the Wolhaarkop breccia as one of the three main iron ore types of the mineralised (with massive hematite) Manganore Iron Formation (Van Schalkwyk, 2005). It was first discussed by Van Schalkwyk and Beukes (1986) as a subset of the Manganore Iron formation in the iron ore deposits at Sishen in the northern edge of the Maremane Dome, and was described as a ferhythmite breccia, a brecciated version of laminated massive hematite ore. It has thus been ascribed to be a consequence of the karstic system collapse which took place in this region, a process responsible for the majority of breccias in this locality (Plehwe-Leissen and Klemm, 1995). A detailed description of the geology of the Maremane Dome has been presented earlier in the study and therefore will not be reiterated here. In short, karstic collapse of Asbestos Hills Iron Formation (mainly the Kuruman BIF) during a period of subaerial erosion of the Transvaal Supergroup strata, resulted in brecciation of the BIF to form the Blinkklip collapse breccia (Plehwe-Leissen and Klemm, 1995).

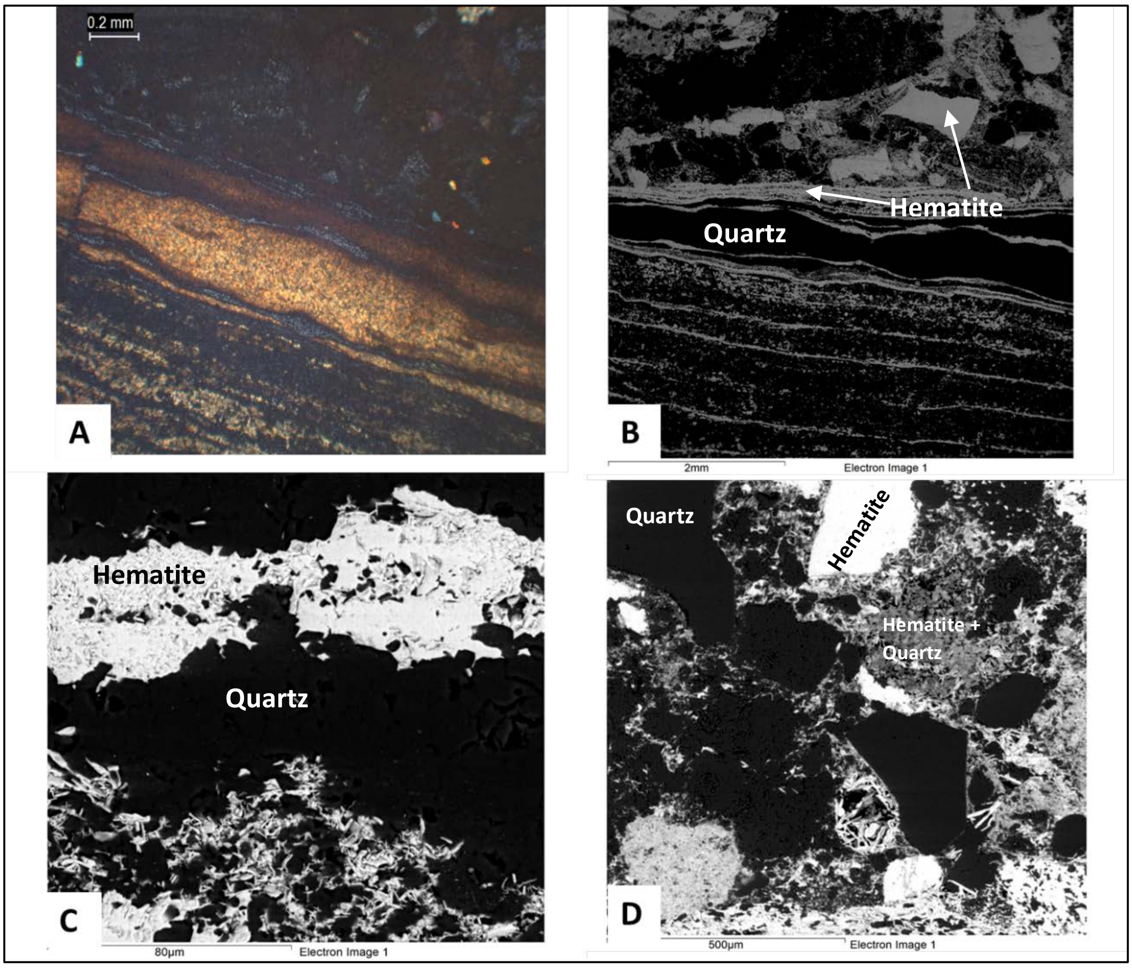

Figure 16: Photomicrographs of the Blinkklip breccia (all but A under reflected light), showing characteristic textural features in the Blinkklip breccia **A.** Bands of hematite and silica in a large clast, in contact with poorly sorted fragmentary assemblage of smaller hematite and quartz clasts; **B.** Same as A but under reflected light. **C.** Finer-scale textural relationship of hematite and quartz in a BIF clast, showing characteristically irregular contact; **D.** Poorly sorted aggregate comprising a mixture of fine-grained hematite and silica clasts.

The Blinkklip breccia samples collected here consist predominantly of BIF clasts showing variable degrees of hematite replacement, from partly hematitised cherty BIF clasts to massive hematite fragments (Fig. 15B). Minor quartz clasts are also occasionally present within the breccia. The matrix on the other hand is largely a mixture of fine-grained hematite and silica particles. The BIF clasts are sub-angular to angular and highly variable in size but generally large – reaching up to 3cm. The hematite and quartz clasts on the other hand display more rounded to sub-rounded shapes. This could suggest some degree of reworking of these clasts before they were cemented into the breccia, although one cannot discount the possible influence of chemical wear caused by circulating fluids in causing at least some of the rounding.

All identified clasts show no evidence of subsequent brittle fracturing or veining that would directly support fluid movement across the breccia. The arrangement and orientation of the clasts is very chaotic and random. Individual BIF clasts show the characteristic inter-banding of alternating silica and hematite, with band thickness ranging from 0.1mm to 1.5mm. Since the Kuruman and Griquatown BIFs are predominantly magnetite-rich, the above mineralogy suggests that the clasts possibly represent reworking of already oxidised Asbestos Hills BIF (Fig. 16A). Zooming closer into fine contact relationships, one can observe that the contacts between these bands are not sharp but instead show hematite truncating into the silica bands, probably as a result of earlier compaction effects in unconsolidated protolith sediment that has been preserved through the oxidation and hematite-forming process.

3.3.2 Shale Breccia

Samples representing this breccia type, just like with the Blinkklip breccia, were obtained from a farm known as McCarthy in the central part of the Maremane Dome (drillcore MC35). Quartz clasts are dominant in this breccia and can also be found as aggregates at certain intervals within the shale host. The breccia appears to be matrix-supported. Over most of the interval in which it occurs (from 50.6m to 38.6m) the clast sizes seem to decrease upwards from cm- to mm-scale. The clasts are of a creamy white colour and are angular to sub-angular in shape. They are set in a matrix with visible traces of iron enrichment in the form of micro-crystalline hematite (Fig. 17A). At a depth of 61.2 the clasts change from white to greyish in colour as the breccia appears to become more clast-supported (Fig. 17B). Traces of coarser flaky hematite (specularite) can be seen as well around the clasts in this part of the core. Some of the clasts appear more sub-rounded further deeper (e.g. at 70.3 m; Fig. 17C).

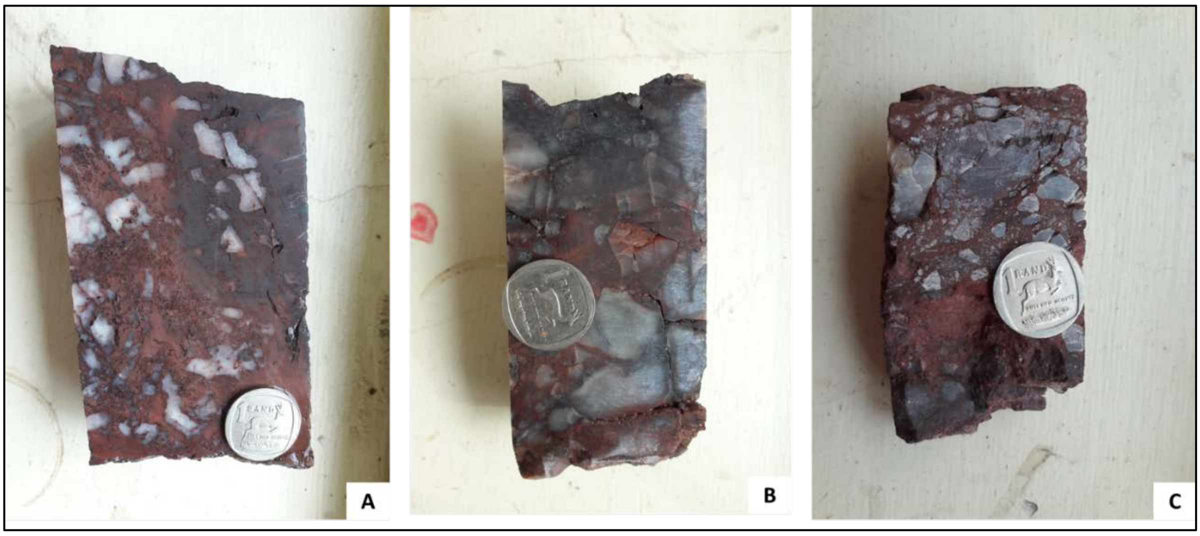

Figure 17: A. Shale hosted breccia**. B.** The breccia becomes clast supported and easily breaks apart around the clasts **C.** The clast become much more rounded

The shale hosted breccia is made up of sub-angular quartz clasts hosted in a fine-grained, hematite-rich matrix. The presence of high silica content – about 84.40% – however, obscures the observation of hematite peaks in related XRD spectra (see Appendix B; Table B10) due to their subdued relative abundance compared to quartz.

The quartz clasts occur in the form of sub-angular fragments reaching about 2cm in size, and less so as apparent fibrous growths of chalcedony. In PPL the quartz clasts exhibit an apparent mottled texture which may suggest a primary origin of the chert through silicification of pre-existing rock (e.g. carbonate). In association with the mottled quartz, local chalcedonic silica develops in association with developed fractures. Characteristic “crackling” textures of incipient fracturing and associated fragmentation is seen in the outer margins of the clasts, which suggest the possible involvement of fluid during a brittle tectonic event (Fig. 18C). Recrystallization effects often accompany the fracturing of the clasts, as seen in Figure 18B.

Fibrous chalcedony is the other form of silica found in this breccia, characterised by its distinct acicular radiating clasts with concentric laminations (Fig. 18D). It appears to be growing in vug spaces together with recrystallized quartz, thus acting as an apparent infill.

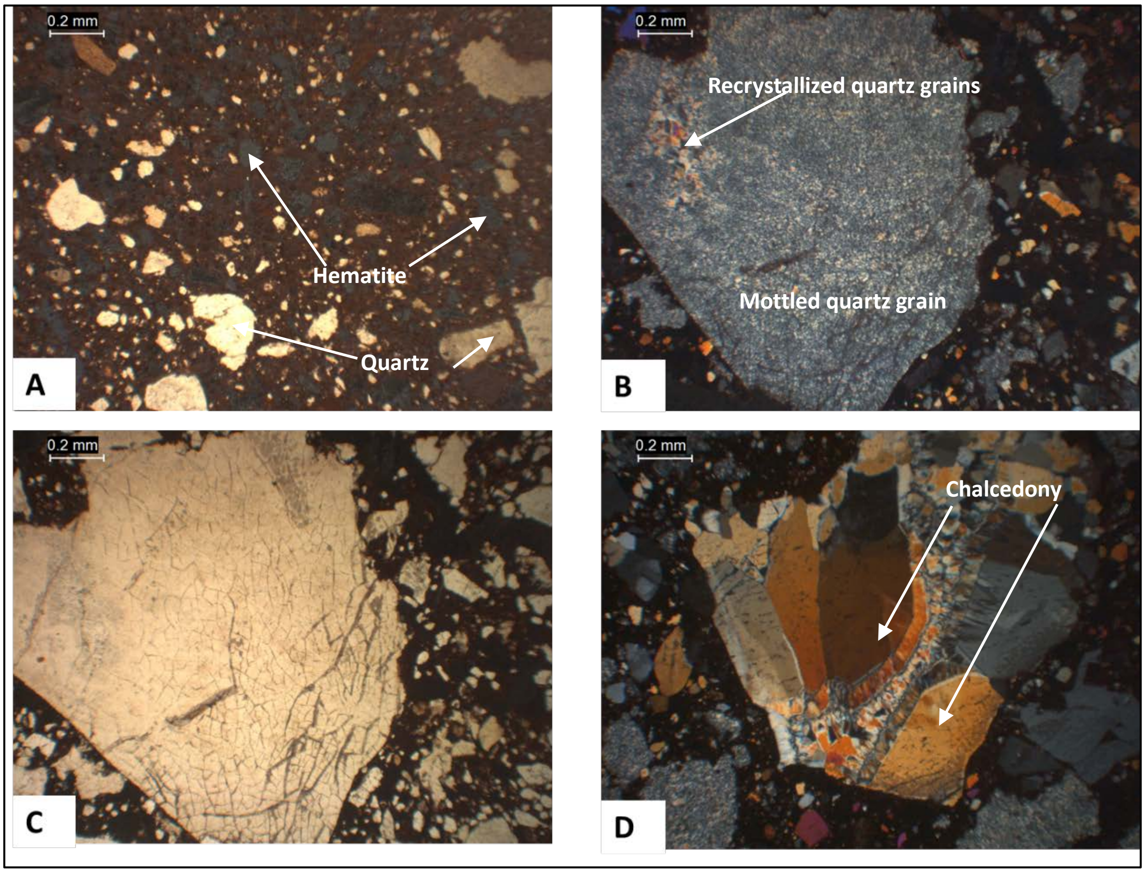

Figure 18: Photomicrographs under transmitted light of the McCarthy shale-hosted breccia. **A.** Overview of sample showing presence of quartz and generally smaller massive hematite clasts; **B.** Locally recrystallized microquartz in a fractured quartz clast; **C.** PPL image of B showing apparent cataclastic fracturing and fragmentation of the quartz clast from the edge inwards, in characteristic fracture patterns; **D.** XPL image of a quartz clast indicating co-existing recrystallized microquartz with microdomains of fibrous chalcedonic silica.

3.4 Geochemistry of shale and shale breccia

The presence of shale immediately above the Campbellrand dolostones as noted in the Leeuwfontein drill cores, as well as its presence both above and below the Wolhaarkop breccia as seen in drill core MC35, does not readily align with the typical primary stratigraphy of the PMF. Based on this, it was considered necessary to investigate further if the shale host bears any direct compositional similarity to shales of the Olifantshoek Supergroup and specifically the basal Mapedi/Gamagara Formation, or represents a possibly altered equivalent, or a different lithotype altogether.

Despite the different localities, the elemental compositions of red shales in Leeuwfontein and shale-hosted breccia at McCarthy are similar, with small variability in aluminium and potassium contents. All samples are dominated by SiO_2 (79.6 wt% - 86.1 wt%), Fe_2O_3 (10.3 wt% - 12.9 wt%) and Al_2O_3 (1.4 wt% - 6.6 wt%), while MnO consistently registers contents below 0.1 wt %.

Table 2: Compositional comparisons in ranges of elemental oxide abundances of shale breccia matrix and Mapedi/Gamagara shale as analysed by Land *et al* (2018).

Oxides	**shale breccia matrix**	**Mapedi shale (Land *et al.*,2017)**
SiO_2	74 – 94 wt%	53 – 73 wt%
Al_2O_3	0.4 – 9.1 wt%	13 – 20 wt%
Fe_2O_3	2.8 – 12.4 wt%	2.7 – 21 wt%
MnO	< 0.2 wt%	< 0.6 wt%
K_2O	0.6 – 2.7 wt%	3.6 – 6.2 wt%
CaO	0.1 – 0.3 wt%	0.01 – 1.5 wt%
Na_2O	< 0.2 wt%	< 0.6 wt%
MgO	0.1 – 0.4 wt%	0.2 – 2.3 wt%

With regard to the analysed matrix of shale breccia at McCarthy, this appears to be red in colour, fissile and very fine grained, akin to a typical Mapedi/Gamagara shale. Bulk analysis of the shale breccia also shows comparable amounts of iron and aluminium content to the afore-mentioned shales. Bulk-rock Fe_2O_3 contents range between 2.8-12.4 wt% falling into the Mapedi/Gamagara shale range as documented by Land *et al,* (2018). Concentrations of Al_2O_3 in the samples are also comparable to those of the Mapedi/Gamagara shale, ranging between 0.4 and 9.1 wt% (Table 2). The lack of manganese in the rocks also agrees with representative compositions of the Mapedi/Gamagara shale. Concentrations of alkalis and alkali earths (Na_2O and CaO) are very low and invariant with the exception of K_2O which registers above 1wt% in selected samples. The barium content in sample LF391/143.5 increases to 1287 ppm due to elevated fine-grained barite infills present in this zone, but otherwise registers values below 100ppm in all other shale samples. Transition metal contents are also quite low, not exceeding the value of 100ppm per element.

In terms of visual representation of selected geochemical signals of the above shales and breccias (as bulk samples or handpicked breccia matrix), Figure 19 below illustrates spidergrams of trace elements normalised against PAAS and against average Mapedi/Gamagara shale (Land *et al.,* 2018). The main points to be extracted is that the trace element distributions amongst the analysed samples do not really offer a consistent picture of correlation with the Mapedi/Gamagara shale or average shale (PAAS) in general, and that in terms of absolute abundances, they record normalised values almost always below the baseline for the greatest majority of elements plotted..

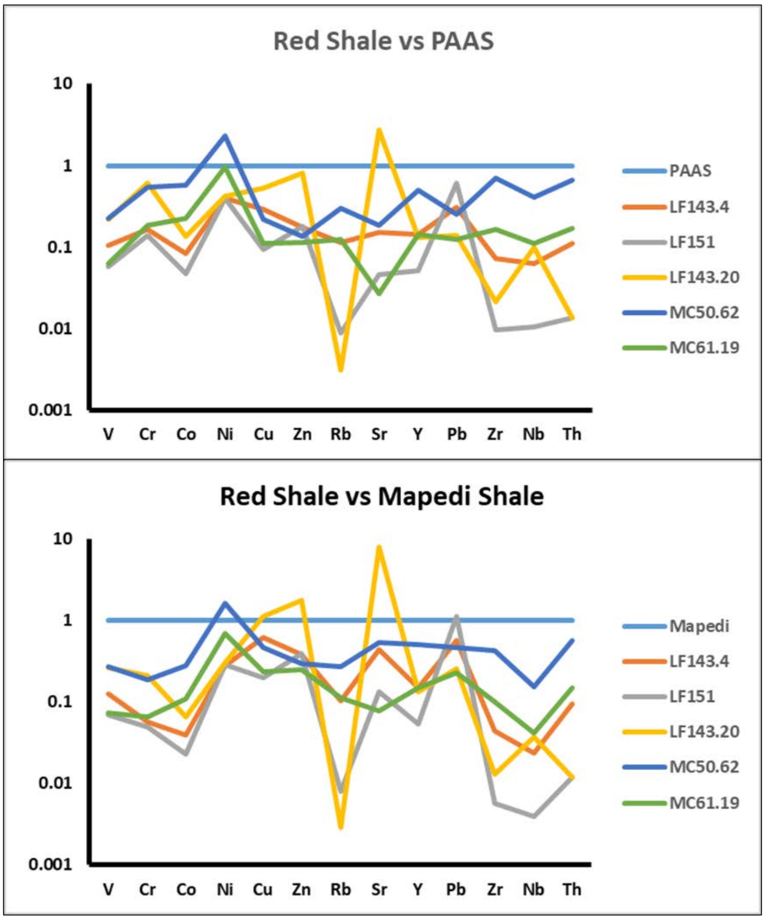

Figure 19: Red shale and shale-hosted breccia spidergrams from Leeuwfontein and McCarthy localities (western belt ores), normalised against PAAS and average Mapedi/Gamagara shale (Land *et al.,* 2018).

4 Manganese in the Postmasburg Manganese Field

4.1 Background

This chapter presents petrographic, mineralogical and geochemical results and some early interpretations obtained from selected representative samples of both the western belt and eastern belt deposits of the PMF. Drill cores LF391 and LF393 obtained from Leeuwfontein farm at Kolomela iron ore mine, and from outcrops at farm Bishop, represent the western belt case deposits. The eastern belt case deposits are represented by ore samples collected only from drill cores, namely WK4/25 and MC35, drilled in the Khumani iron ore mine by ASSMANG Ltd and in farm McCarthy by geological consultancy OREX, respectively.

With regard to the eastern belt ores, it should be noted that the Wolhaarkop breccia and associated Mn mineralisation from farm McCarthy showed evident signs of supergene alteration, resulting in a typically “earthy” and relatively soft and friable appearance of the intersected breccia-hosted ore. This adds a variance to the eastern belt sample set collected and analysed for this study. By contrast, the Khumani drill core samples represent unaltered portions of eastern belt ore well below the maximum depth of present weathering. Although the above allow for a much more complete assessment of the geological history of eastern belt ore by incorporating recent supergene effects, much of the attention regarding the primary origin of the said deposits will understandably be based mainly on the fresher samples from the Khumani drillcore.

The Wolhaarkop breccia represents the link between the previous chapter on breccias, their classification and origin, and the Mn ore deposits of the eastern belt. Manganese ore dominated by braunite is reported to make up the matrix of the Wolhaarkop breccia, together with other mineral phases such as hematite and quartz (Gutzmer and Beukes, 1996). Similarly, braunite/bixbyie assemblages with much hematite dominate the western belt ores. This section will assess the geochemistry of the western and eastern belt ores in light of previous published work as well as data obtained during this study. To this end, the mineralogy and petrography of the ores will be revisited but it will not constitute the primary focus of this chapter; it will only serve as the necessary context for interpretation of the geochemical data and signals.

4.2 Eastern belt manganese ores: Petrography and Mineralogy

The terminal depth of the drillcore intersection selected from the Khumani borehole WK4/25 is at 141m from present surface. The Mn-mineralised Wolhaarkop breccia samples were logged and collected from a depth of 141m to 121m, resulting in a total of 6 samples. These were complemented by two samples of apparently supergene-altered Wolhaarkop breccia obtained from the McCarthy core MC35. This particular core extended from 105m from the deepest point of drilling, up to 20m from present surface. The Mn-rich samples were obtained from a depth of 92m to 80m.

4.2.1 The Wolhaarkop breccia: drillcore WK4/25, Khumani Mine

The Khumani drillcore can be subdivided into two sub-portions: the highly brecciated lower unit (141m to 121m) comprising abundant mm- to cm-sized chert clasts set in a fine-grained ferro-manganiferous matrix; whereas the upper part appears to have a much smaller clast population ranging from mm to sub-mm scale. In the lower part of the upper portion, crude layering can be observed in the arrangement of clasts (Fig. 20A), a texture that has also been reported before in other publications (Gutzmer and Beukes, 1996; Plehwe-Leisen and Klemm, 1996), suggesting that this feature is probably distinctive and potentially significant for the Wolhaarkop breccia. The clasts are, however, not arranged in layers throughout the core; in the lower sub-portion of the Wolhaarkop breccia proper, they generally exhibit poor sorting with clasts size varying from mm to cm scale (Fig. 20B).

The contact between the clast-dominated lower portion of the core and the upper matrix-supported and more clast-poor one, can be reasonably considered as relatively sharp. The matrix is very fine-grained and its colour is typically dark grey to blackish throughout the core, while the clast colour ranges from creamy white to greyish-white. In terms of bulk mineralogy, XRD results of handpicked fragments of matrix ore were crushed and analysed, aiming to avoid the influence of very large chert clasts and thus dominance of silica (as quartz) in the resultant spectra. The results (Fig. 21) nevertheless still show the overwhelming presence of quartz, although peaks diagnostic of braunite and hematite were observed and therefore constitute major components of the matrix (Fig. 21). This is testament that fine-grained quartz is also a predominant matrix mineral component together with braunite and hematite.

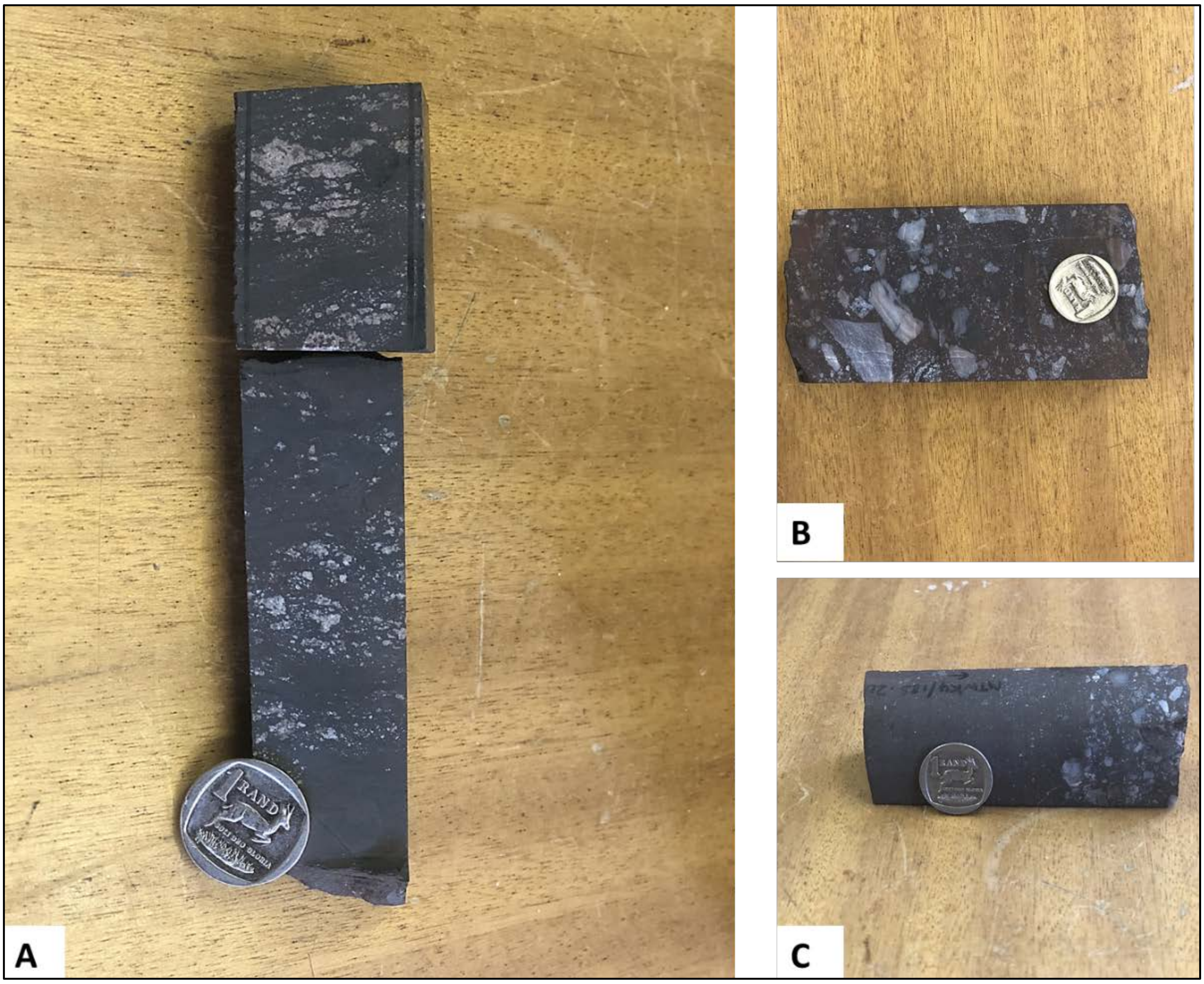

Figure 20: **A.** Crude layering within the Wolhaarkop **B.** The breccia also exhibits a poor sorting clasts **C.** Sharp contact exists between clast-dominated and matrix-supported lithology in the breccia.

Reflected light microscopy and SEM analyses revealed very intricate fine-grained textural arrangements of the main minerals observed and identified. Hematite-rich domains may take the form of individual clasts, but on a finer scale one can observe a complex relationship with small angular particles of braunite within hematite hosts (Fig. 22A). Numerous, small quartz grains make up a large portion of the rock in addition to the large quartz megaclasts floating in the matrix (Fig. 22B). Thin braunite rims are sometimes visible around quartz clasts (Fig. 22C), indicating possible replacement reaction products between silica and original manganese oxides in the matrix. Similar features were also observed by van Schalkwyk (2005) on Wolhaarkop samples collected from various localities in the PMF.

The Wolhaarkop breccia displays also abundant vuggy textures especially within the braunite-rich matrix, that are filled by quartz and barite grains that are quite dominant within many areas across the selected samples (Fig. 22D).

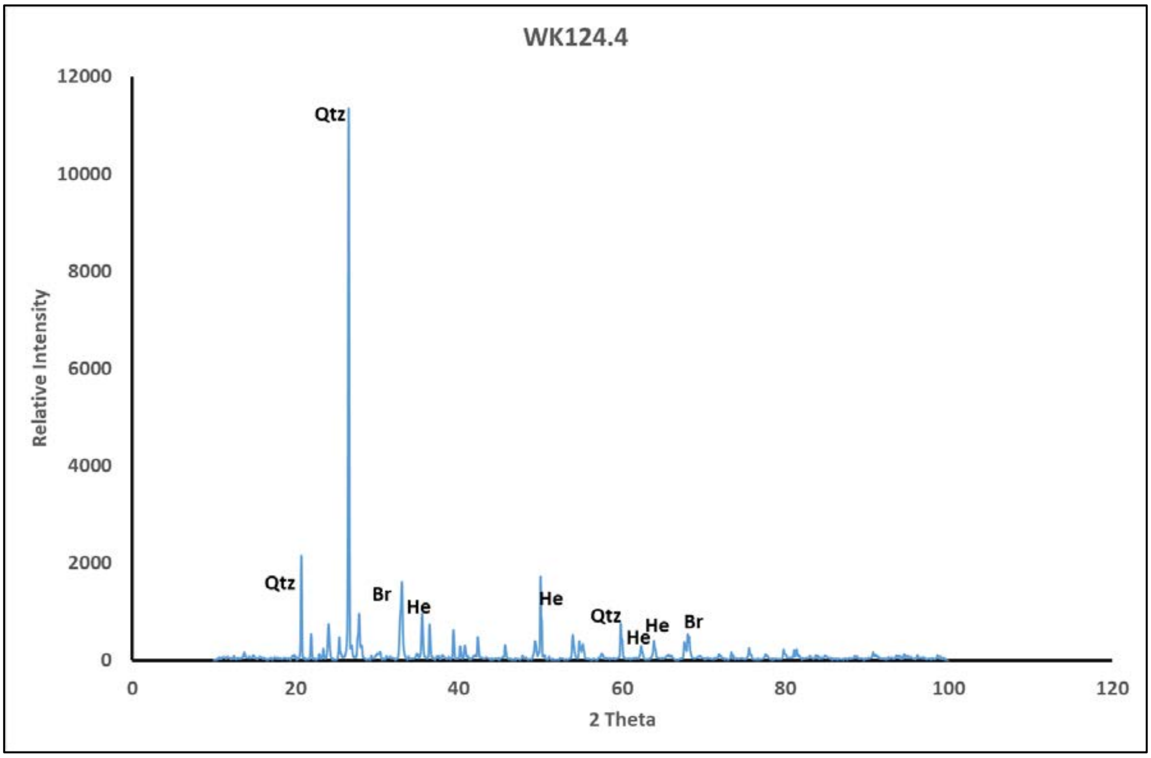

Figure 21: XRD spectra showing dominant mineral species in the Mn ore samples from the Khumani drillcore

Apart from its braunite association, anhedral barite grains are also found dispersed throughout the samples in a rather widespread fashion. In these particular samples, no cross-cutting barite veins were observed. Small apatite and albite crystals were also seen in association with the matrix in most of the samples collected.

It should be added that although previous publications have reported the presence of supergene minerals like romanechite, pyrolusite, ramsdellite and cryptomelane (e.g. Gutzmer and Beukes, 1996), the samples analysed above did not contain any of these, nor did they display any textures to suggest that they have undergone supergene alteration.

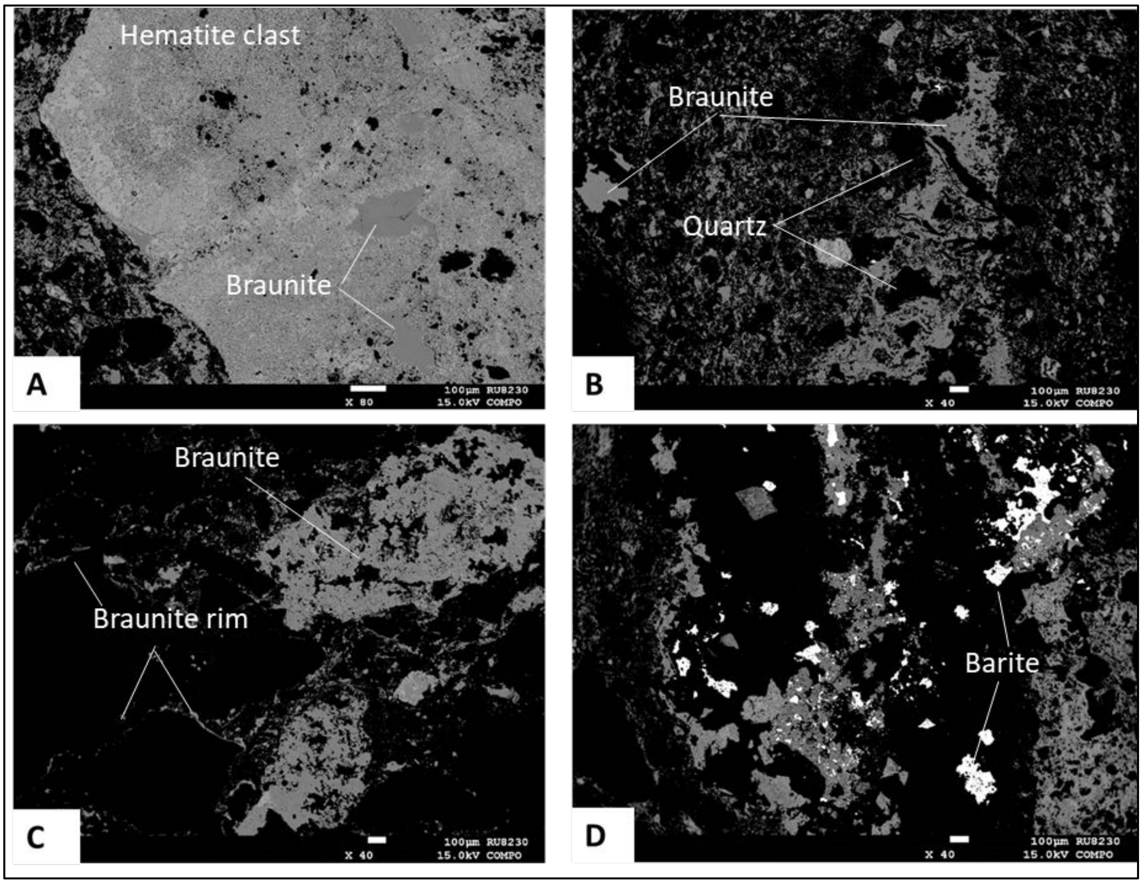

Figure 22: Backscattered SEM images of Wolhaarkop breccia, Khumani mine, core AK4/25. A. Hematite-rich "clast" in Wolhaarkop breccia matrix that encloses braunite **grains. B.** Typical Wolhaarkop breccia matrix composed of braunite, lesser hematite and abundant fine-grained quartz **C.** Quartz clasts displaying thin braunite rims **D.** Vuggy textures within the Wolhaarkop breccia matrix that are filled by quartz and small barite grains

4.2.2 Supergene-altered Wolhaarkop breccia: drillcore McCarthy (MC35)

Samples representing the Wolhaarkop breccia from farm McCarthy breccia were obtained from drill core MC35. Here, as previously mentioned, the breccia matrix appears much darker (essentially pitch black) and friable, yet retaining an abundance of subhedral chert clasts. Polishing of this material to produce sections for petrography was thus relatively more difficult. Under the microscope, the samples looked particularly fine-grained and presented great challenge even in terms of observing grain boundary relationships and individual mineral phases. In addition, a plethora of vugs was also observed, suggesting that the rock had suffered severe dissolution/leaching effects during supergene weathering. Because of the above, mineral identification for this sample relied mainly on XRD, and SEM-EDS/EPMA analyses.

It is important to note that many manganese oxides in supergene Mn ores may be better identified using other techniques (e.g. infra-red spectroscopy) than XRD, because of issues such as poor crystallinity, crystal size and lattice disorders (Potter and Rossman, 1979). Nonetheless, the XRD spectra of these samples in comparison to those of Zhao *et al* (2005) confirmed the presence of the Mn species cryptomelane (Fig. 23). This was further supported by probe analysis results of the same sample (see Appendix B; Table B9) and the positive correlation between Mn and K as obtained from bulk-rock XRF results (see next section), as K had not been included in the analytical set up for the EPMA analysis.

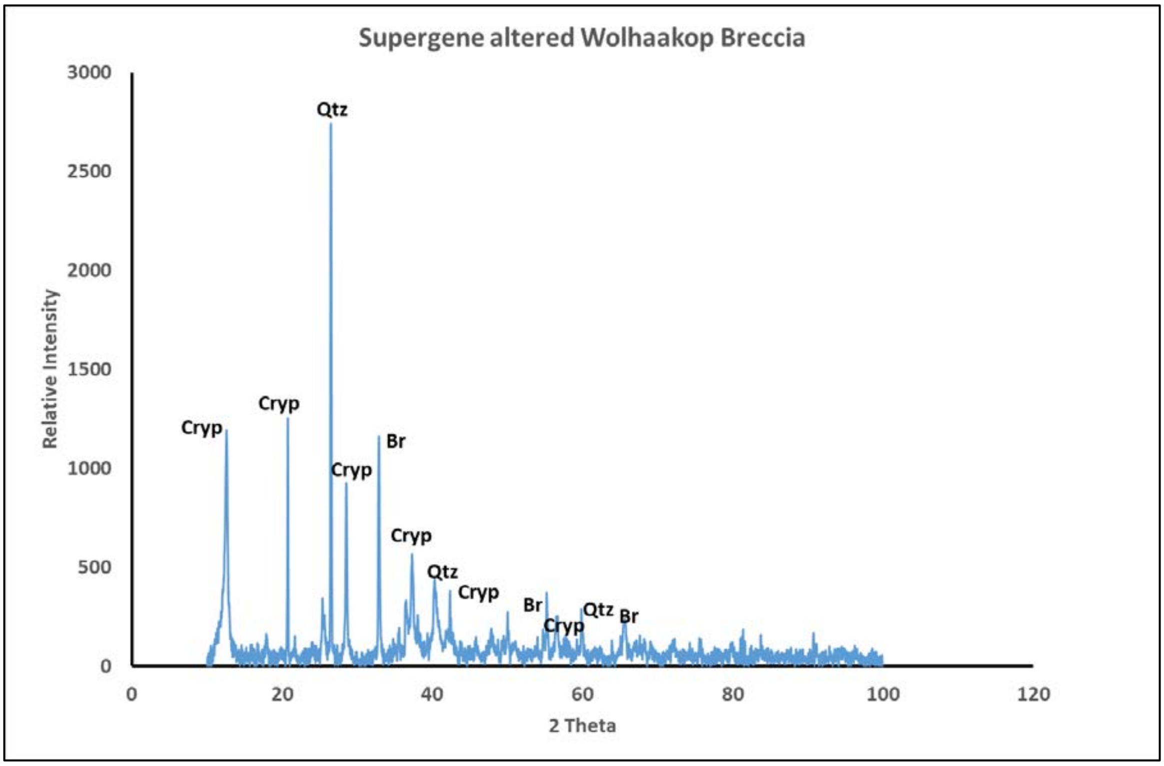

Figure 23: XRD spectra of the supergene-altered Wolhaarkop breccia Mn ore obtained from drill core MC35

It is therefore concluded that the matrix in the Wolhaarkop breccia is comprised of a relatively simple combination of very-fine grained cryptomelane together with residual braunite on microscopic scales, and an abundance of quartz clasts (Fig. 24B). Barite grains and veinlets are also observed throughout the matrix. The cryptomelane dominates the matrix of the breccia but it is also observed within veins along with barite (Fig. 24C) as open-space lath-like grains. EPMA analyses indicated that such grains may contain over 3wt% MgO (Appendix B: Table B9) which is somewhat atypical of the chemistry of pure end-member cryptomelane (Fig. 24D).

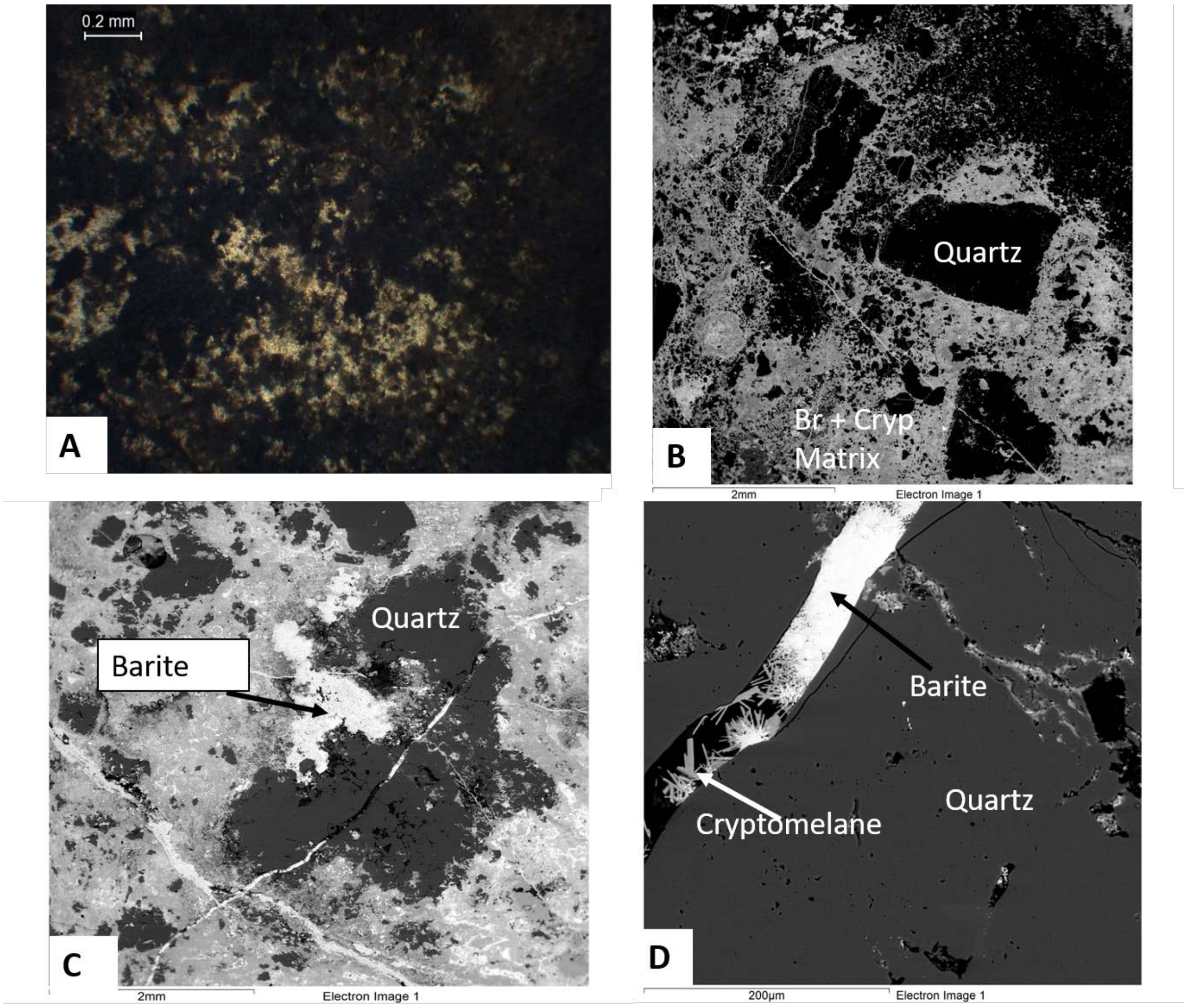

Figure 24: Petrographic and backscattered SEM images of Wolhaarkop breccia, McCarthy farm, drillcore MC35. **A.** Microscopic overview displays complex and very fine-grained textural relationships. **B.** Typical view of Wolhaarkop breccia showing quartz clasts in a complex Mn-rich (cryptomelane+braunite) matrix. **C.** Sub-angular fractured quartz clast with rugged contact relationships with surrounding matrix and crosscutting veins. Bright mineral in veins and matrix is barite. **D.** Zoomed view of part of image C, showing barite vein in which lathe-like open-space growths of Mg-rich cryptomelane are observed.

Further SEM and EMPA imagery revealed cryptomelane to also exist as vug fills in an already cryptomelane+braunite matrix (Fig. 25A). The fills are often characterized, rather curiously, by a characteristic thin braunite halo around them (Fig. 25B). It is important to note that EPMA analyses of braunite in some instances (see Appendix B; Table B10) produced silica content of about 4%, which is substantially lower than the stoichiometric abundance of silica in ideal braunite of 9 – 10 wt% (Gutzmer and Beukes, 1995). Such analyses may reflect partial breakdown of braunite and associated silica loss, without associated development of cryptomelane as replacement product

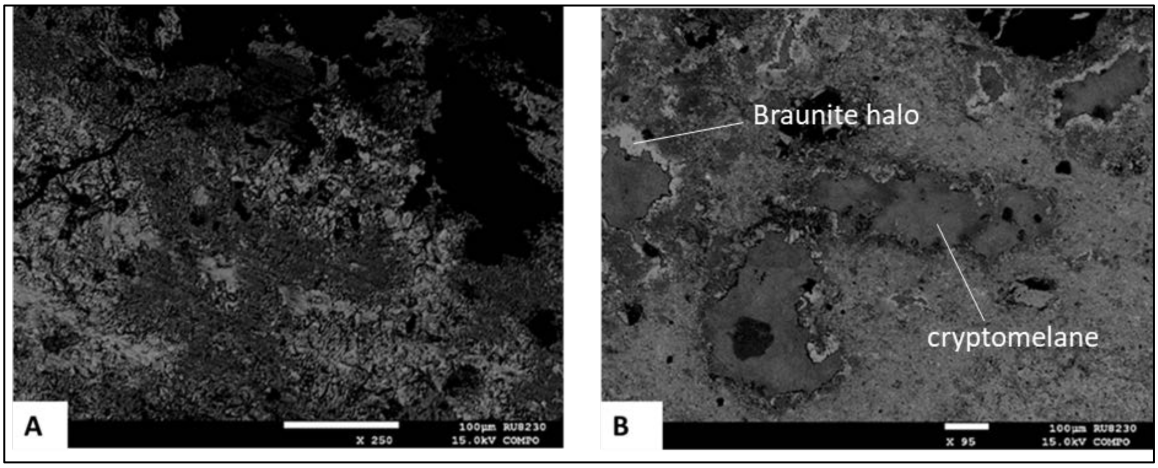

Figure 25: Further back-scattered images of Wolhaarkop breccia matrix from drillcore MC35 at farm McCarthy. A. Irregular, "patchy" contact relationships between braunite (brighter) and cryptomelane (darker). B. Cryptomelane-filled vugs rimmed by braunite halos.

With respect to the assemblages described here against the ones that characterise Wolhaarkop breccia samples from Khumani mine shown in the previous section, it is important to emphasize that the observations made in this study did not include the presence of Na-rich silicate minerals such as albite, aegirine or serandite, which otherwise typify compositions of the breccia as shown earlier in this thesis and also in previously published studies (e.g. Gutzmer and Beukes 1996; Moore *et al.,* 2011). This is an observation also supported by XRF results which showed Na to be in very low concentration in the two analysed samples. By contrast, the presence of barite accounts for the relatively elevated Ba and Sr (substituting for Ba) in the order of thousands ppm, and its stability during supergene alteration. The presence of cryptomelane combined with the absence of sodic minerals found in the fresh Wolhaarkop breccia samples in the Khumani drillcore, suggests likely breakdown and remobilisation of Na due to supergene alteration, whereas K would have been at least partly retained in the cryptomelane structure.

4.3 Geochemistry

4.3.1 Unaltered Wolhaarkop Mn-ore breccia: Khumani drillcore

The mineralogy of the Wolhaarkop breccia samples from the Khumani drillcore, namely abundance of hematite, quartz and braunite, would be expected to be accompanied by the dominance of elemental oxides Fe_2O_3, SiO_2 and MnO_2 in terms of whole-rock geochemistry.

This is indeed supported by the geochemical data produced in this thesis that show respective maxima as high as 92.76 wt%, 64.37 wt% and 40.87 wt% respectively. Bulk aluminium oxide also shows relatively high values at a range between 1.68 wt% and 5.75 wt%. Alkali contents are quite variable but still at a wt% level: Na_2O was found to be highest in just two samples, namely 2.35 wt% in sample WK124.4 and 2.38 wt% in sample WK135.2, and these are the samples where albite was found to be present in significant modal amounts. This confirms previous work done on the Wolhaarkop breccia by Moore *et al* (2011). It is noteworthy, however, that the remaining 5 Khumani samples had Na_2O content ranging from 0.07w% to undetectable, which means that the distribution of Na minerals in the rock must be very uneven. K_2O also ranges widely between 0.03 wt% and 1.17 wt% which would reflect mainly in minor K-feldspar as also reported in Moore *et al* (2011).

The high aluminium content in the Wolhaarkop samples has led to the choice of the Post-Archaean Average Shale (PAAS) for normalisation of the data and production of spidergrams to assess possible elemental associations, controls, and overall geochemical behaviour. The plots will include trace elements only (including rare earth elements, REE), and will focus on possible inferences of the relative mobility and therefore open- or closed-system behaviour of any of them during the geological history of the deposits. In principle, elements such as Zr, Nb and Hf known as High-Field Strength Elements (HFSE) are commonly immobile and enriched in shales, and therefore they will not be included in the plots for consideration. By contrast, Large Ion Lithophile Elements (LILE) such as Sr, Rb, etc, would be more mobile and may show marked depletions or exotic enrichments. The same may apply to transition metals (Zn, Cu, Ni) which show diverse behaviour depending on the rock mineralogy and fluids that may have transported them as soluble complexes into or out of the rocks during geological history

Qualitatively, all samples follow a similar trend for trace element behaviour normalised against PAAS with slight variations from sample to sample in certain elemental concentrations (Fig. 26). The first feature of note is that the rocks are enriched substantially in Ba and Pb compared to PAAS, which agrees with the omnipresence of barite in the samples that probably also contains Pb substititions for Ba and therefore high Pb content too. Other elements that show consistent enrichment relative to PAAS for most samples are transition metals Co, Ni, Cu and Zn which are probably associated with the oxides of Fe and Mn, although for some samples the normalised values plot below the shale line and some clearly above. The remaining elements, especially those in the middle of the x axis representing LILE such as Sr, Rb and Cs, are very depleted compared to PAAS.

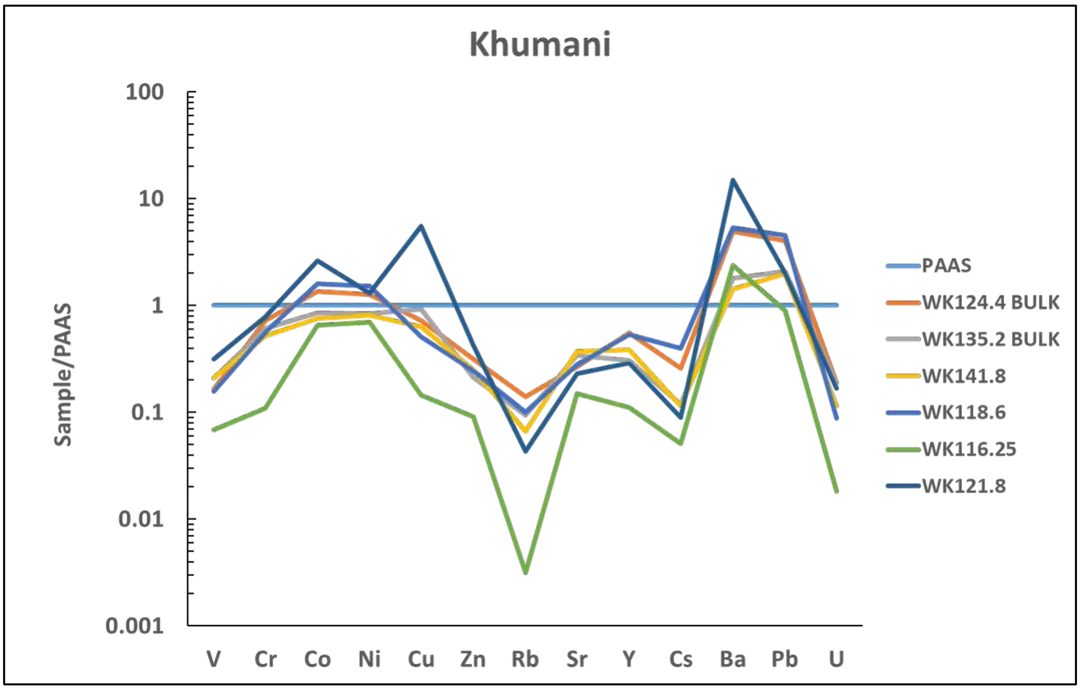

Figure 26: PAAS-normalized trace element spidergram of Wolhaarkop Mn breccia from drillcore WK4/25

With reference to REE data (Fig. 27), the normalised values and spidergrams plot almost completely below the PAAS line and therefore show depletion relative to average shale. The shape of the patterns for almost all samples shows a convex-up shape with the middle REE being the most enriched. LREE show positive slopes (increasing values) from La up to Eu and the HREE show relatively flatter behaviour or negative slopes, although variability in these parameters exists from sample to sample.

The other main features of note are the consistent behaviour of Eu which shows a prominent positive spike in all the samples, whereas the behaviour of Ce is less consistent, with positive and negative spikes shown. Both of these REE are redox sensitive as they can oxidise or reduce, and Eu is also mineralogically controlled as it commonly partitions into feldspars. It is therefore possible that at least the behaviour of Eu may be controlled by the presence of plagioclase (albite) and K-feldspar in the rocks.

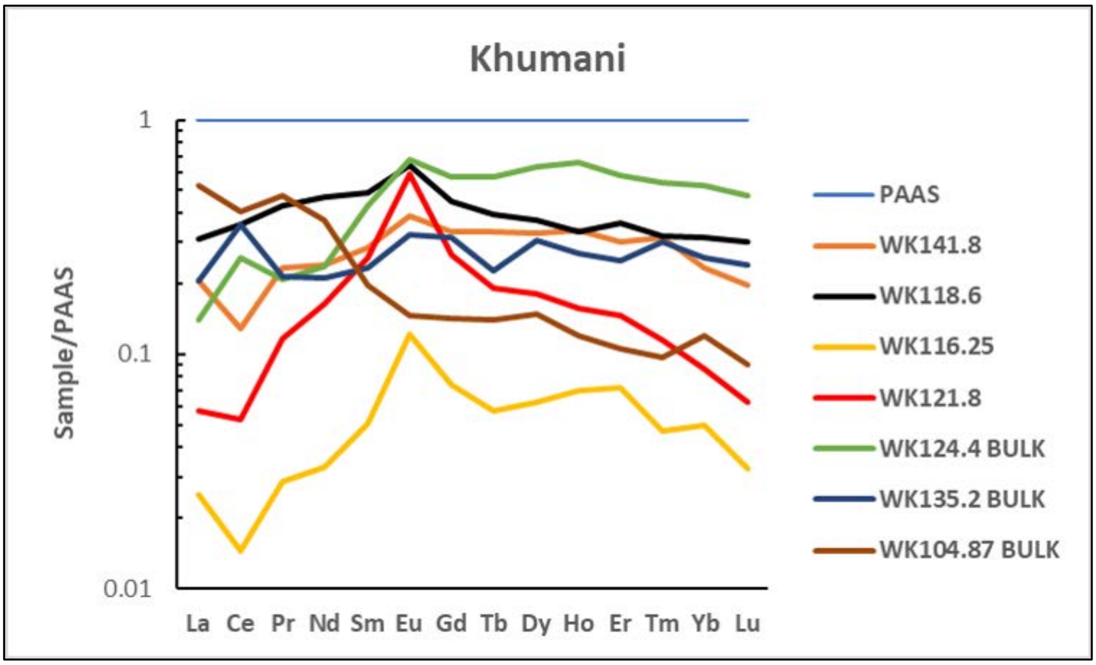

Figure 27: PAAS-normalized REE spidergram of Wolhaarkop Mn breccia from drillcore WK4/25

4.3.2 Altered Wolhaarkop breccia: farm McCarthy (drillcore MK35)

As indicated earlier, two samples (MC83 and MC86.3) of the altered breccia were analysed from the McCarthy drillcore. The chemical composition of the breccia is dominated by concentrations of MnO_2 (9.21 wt% and 57.08 %), Fe_2O_3 (3.71 wt% and 8.51 wt%) and SiO_2 (24.29 wt% and 83.64 wt%). All other elements are present in very low concentrations, with the exception of MgO in sample MC86.3 which registers 3.42 wt %. This is also the very enriched in Mn sample of the two, with a high abundance of cryptomelane which as indicated earlier, occasionally takes some MgO in its structure. With regard to the remaining major element oxides, all of them are in concentrations far lower than those in the samples from the Khumani drillcore, especially the Na abundance. The results shown earlier from petrography and mineralogy have indicated that this is an expected feature, as Na-rich phases are all but absent from the rock probably due to the supergene weathering it underwent.

The trace element geochemistry is dominated by Ba (1373 – 4842 ppm) and Sr (191 ppm – 360 ppm). The rest of the elements analysed for are present in low to moderate concentrations in relation to the previous two elements but occur generally in ranges similar to those reported by Gutzmer and Beukes (1996). These include Co (5.8 and 8.8 ppm), Ni (50 and 55 ppm), Cu (26 and 27 ppm), Pb (3.1 and 6.4 ppm), Zn (27 and 32 ppm) and V (24 and 30 ppm). The two

PAAS normalised spidergrams (Fig. 28) are very similar and show generally a more depleted picture than the Khumani samples, suggesting general mobility of most elements during supergene alteration, including the transition metals. Nevertheless, the spikes in Ba and Sr probably indicate that at least barite (+ Sr substituting for Ba) behaved conservative during the supergene process and retained its geochemical signature in the rock during alteration.

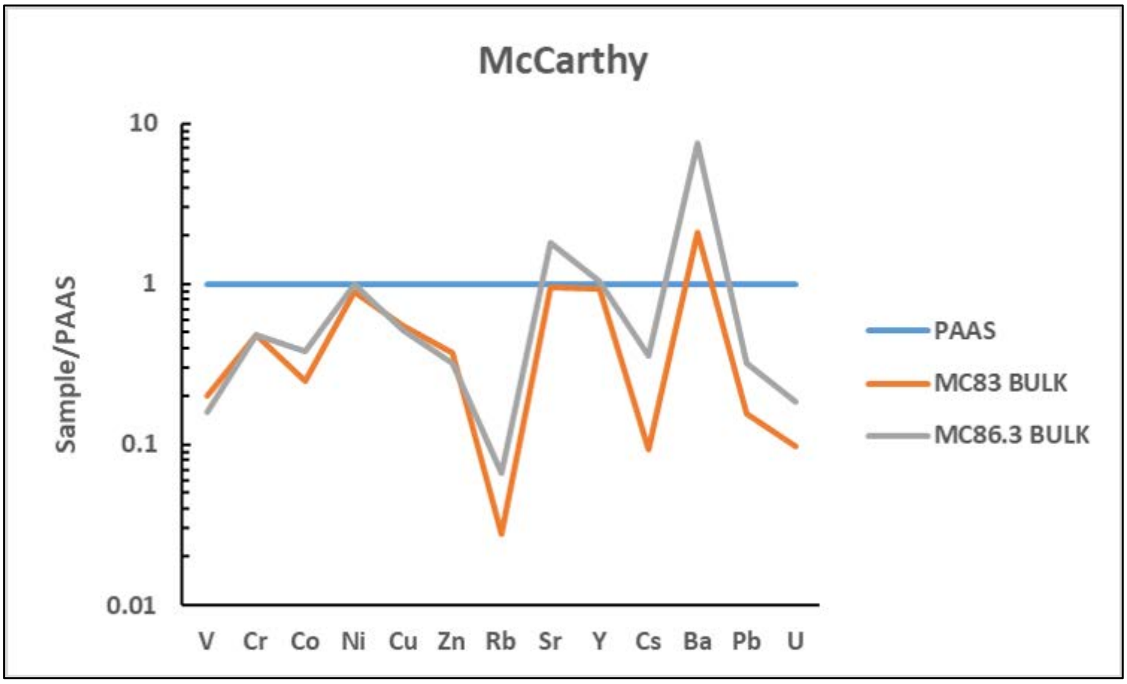

Figure 28: PAAS-normalized trace element spidergram of Wolhaarkop Mn breccia from drillcore MC35

Finally, in relation to the PAAS-normalised REE diagrams, both samples show a depletion compared to PAAS at similar levels to those seen in the Khumani samples (Fig. 29). In addition, the two spidergrams appear much flatter by comparison, and lack the prominent Eu spike. This may be a function of the breakdown and removal of minerals such as feldspars from the pre-alteration breccia, which would have controlled the Eu in the first place.

4.4 Western Belt Mn deposits

This section presents results from the petrography and geochemical analysis of ore samples from the Western Belt. Texturally, the western belt manganese ore can be divided into two types, namely micro-brecciated (contorted) and laminated ore. Due to their more direct stratigraphic association with shales in the form of intercalations within the ore, geochemical analyses of samples from this belt have also been normalized against PAAS.

As mentioned already earlier, petrographic and mineralogical analysis was conducted on a total of 20 western belt manganese ore samples: ten of these came from the Bishop outcrop locality and the other ten were obtained from the Leeuwfontein farm drillcores at Kolomela Iron Ore Mine.

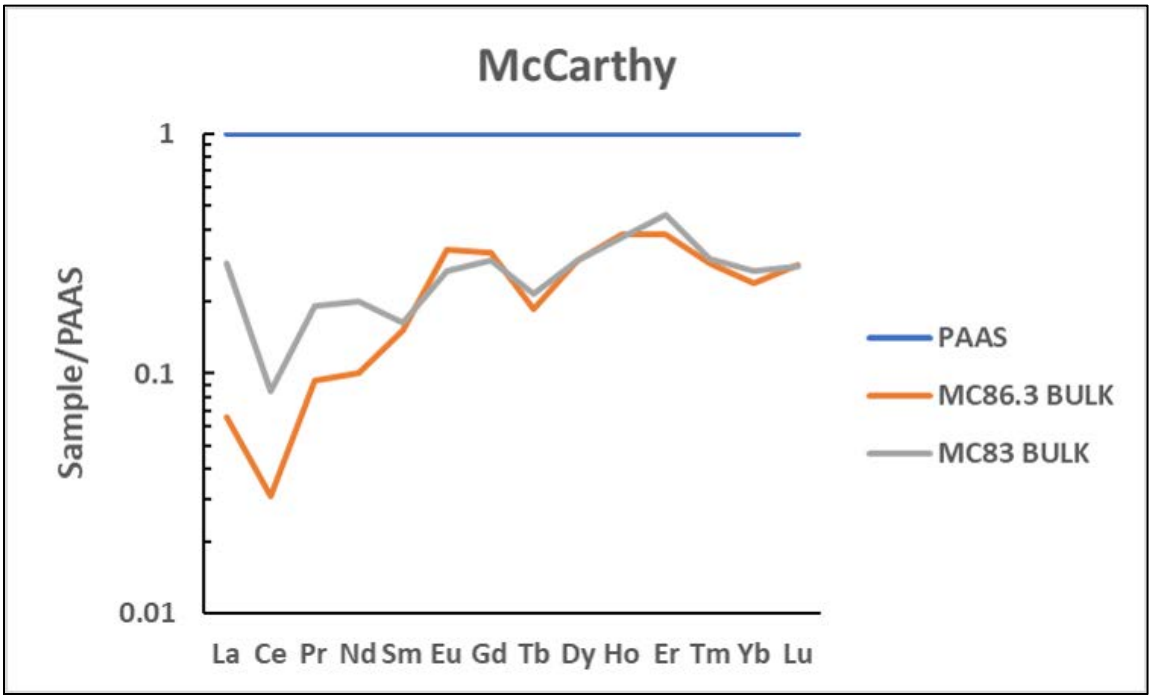

Figure 29: PAAS-normalized REE spidergram of Wolhaarkop Mn breccia from drillcore MC35

4.4.1 Bishop outcrop locality

a) Laminated ore

Samples from the outcrop section at the Bishop locality displayed distinct laminations and were therefore chosen as a classic example of laminated western belt ore for this study. It is, however, important to note upfront that ore interlayering on outcrop scale alternates between strongly laminated layers and more massive ones at dm-scales, and that very thin shale interlayers are still visible in ore that exhibits only crude or no lamination.

On a finer (sub-cm) scale, macroscopically dark and light metallic grey laminations make up the ore intersections (Fig. 30A). The darker layers represent zones enriched in aluminosilicate material whereas the brighter ones are rich in metal oxides, mainly hematite and braunite with respect to iron and manganese respectively, along with lesser very fine-grained interstitial alumino-slilicate phases. Therefore, these alternations almost suggest a decoupling between hematite and aluminosilicate material making up the associated shale interlayers (see corresponding geochemistry later). With regard to the mineralogical character of the aluminosilicate mineral, its identification was somewhat difficult and required a combination of XRD and bulk geochemical results. It will be shown in the latter part of this chapter that these analyses converge to the mineral being ephesite. It will therefore be referred to as such from the outset, and the reasoning will be provided at the end of the chapter.

A closer view of iron rich layers revealed intriguing textures, such as apparently zoned particles of hematite with darker, ephesite-rich rims (Fig. 30B). The size of the hematite cores is variable, and some of these features do not have hematite centres at all. Where well developed, the hematite cores show well crystalline, compact hematite particles whereas the surrounding ephesite-rich rim appears more impure and porous. In the more ephesite-rich layers, the zoned hematite grains are not present but disseminated hematite particles are still quite dominant.

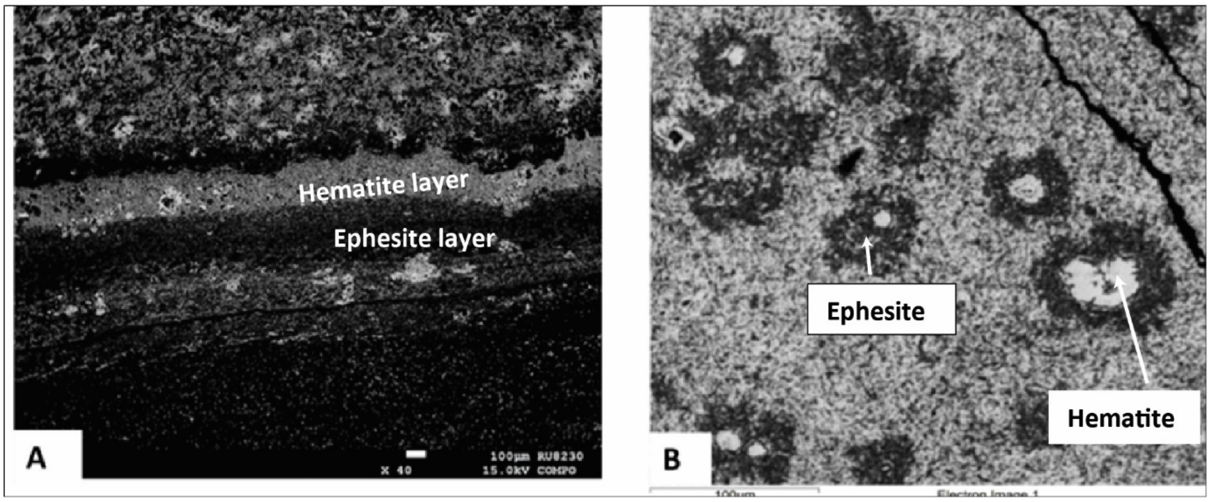

Figure 30: Textures and mineralogy at locality Bishop of western belt ore. **A.** Alternating ephesite-rich and hematite-rich layers. **B.** Hematite layers containing zoned particles of hematite surrounded by ephesite-rich rims

Individual hematite-rich laminae show a characteristically wavy and wispy texture (Fig. 31A). A closer look at these laminae reveals a coexistence of hematite laminae intricately intercalated with thin braunite laminae towards the center (Fig. 31B). Often the braunite laminae appear discontinuous within the more continuous hematite bands. The co-existence between these two minerals is also seen in massive type ore of the same locality (see below).

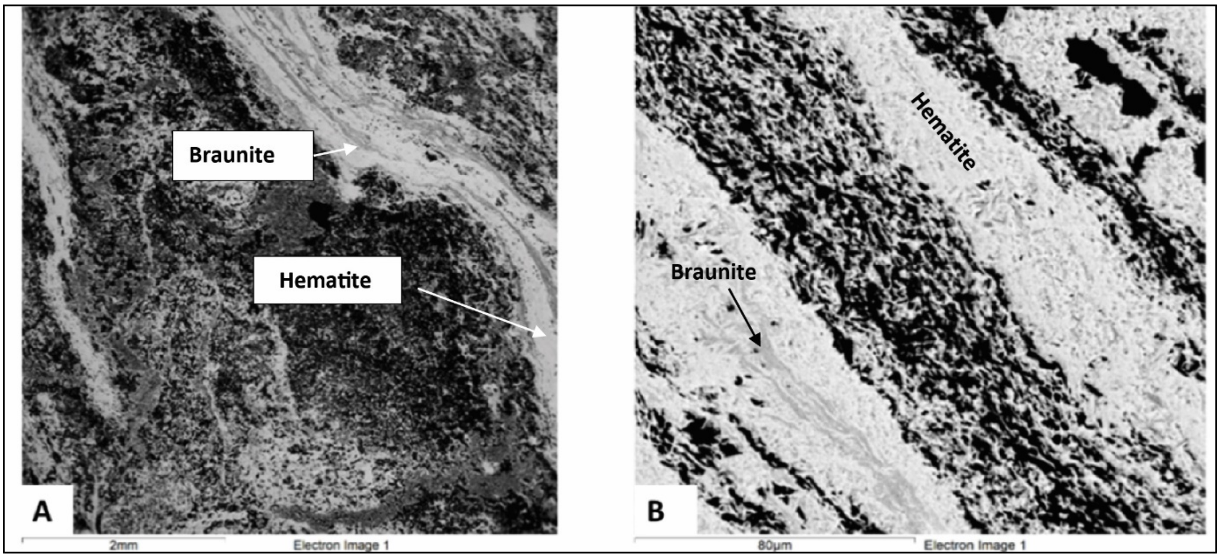

Figure 31: Laminated western belt ore from the Bishop locality showing intricate braunite-hematite laminations

b) Massive Ore

The second ore texture observed at the Bishop outcrop is that of a massive fine-grained ore (Fig. 32A). Microscopically, there are some striking differences from the laminated ore type seen in the same outcrop. Here, characteristic textures include abundant braunite micro-granules with characteristically equant shapes and distinctly rugged to almost serrated edges, floating in an ephesite-rich matrix (Fig. 32B). These grains range in size from sub-mm to cm scale and in most parts coalesce to form a much larger braunite zone. A closer look at the braunite grains reveals the presence of hematite inclusions (Fig. 32C), in a manner not all that different to the hematite/braunite associations in laminated ore. The ephesite-rich groundmass may also develop protrusions into braunite particles in characteristic embayments within the grains (Fig. 32A), (see top-left area of photomicrograph containing larger braunite grains). This could be indicative of partial overgrowth of braunite in a pre-existing alumino-silicate matrix.

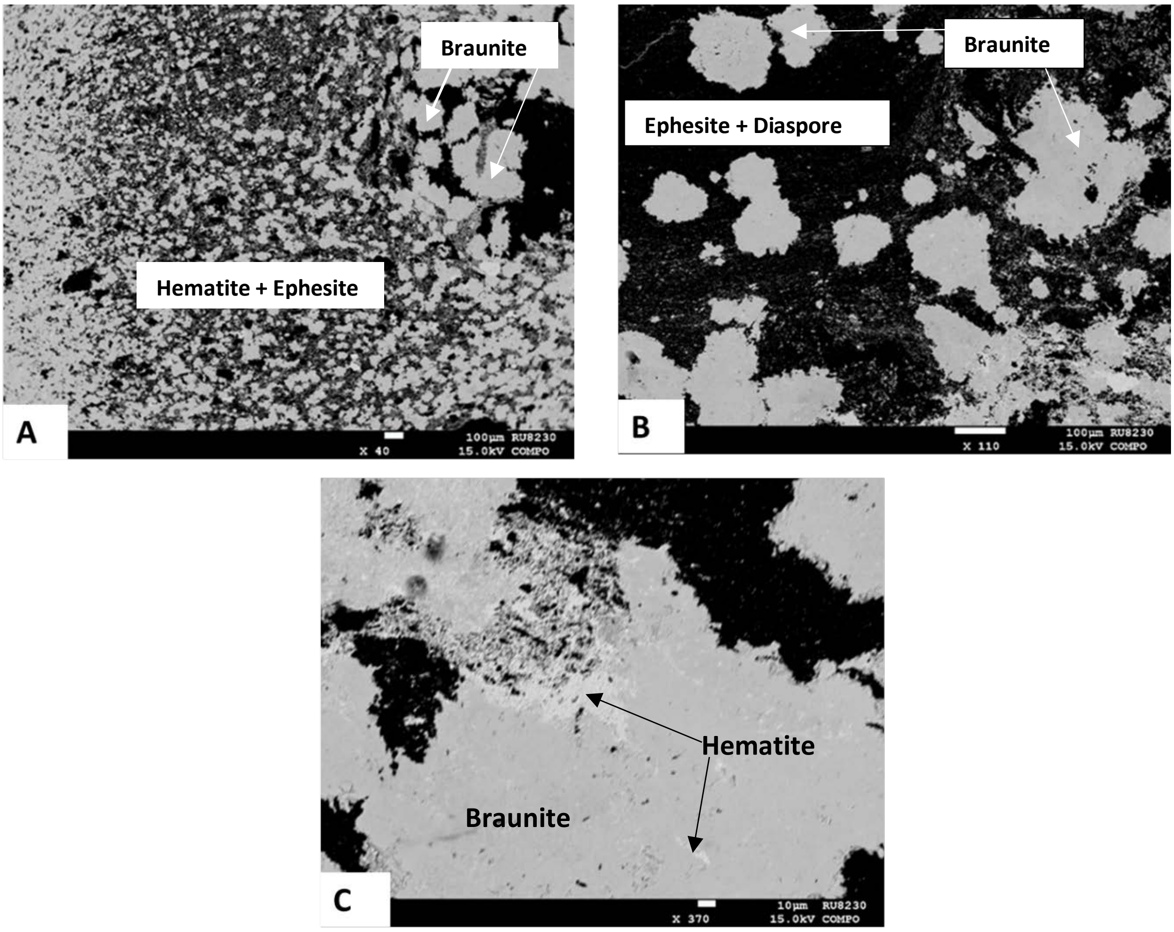

Figure 32: A. Massive, granular western belt manganese ore from locality Bishop. B. Individual braunite grains exhibiting characteristically rugged to serrated grain edges; C: Minute hematite inclusions in braunite

4.4.2 Leeuwfontein drillccores: western belt (or mixed type?) manganese ore

Ore samples from the two drill cores from the Leeuwfontein area at Kolomela mine, are considered here to be of a shale association due to their lithostratigraphic association as presented in Chapter 2 earlier. They are therefore treated here as a candidate of the western belt ore class, similar to the Bishop locality. However, it should be noted that no distinct laminations could be observed with the naked eye from the hand specimens collected, although very thin and discontinuous shale laminations can be seen in certain sections of the ore intersection. Therefore, there is every likelihood that this ore type may not be fully comparable to that described from Bishop locality, and it may even represent a hybrid ("mixed") type of ore as this has been reported previously (Gutzmer and Beukes, 1996; see also Chapter 1).

The ore in the Leuwfontein cores is very iron rich, even more so than at the Bishop locality, and is consequently dominated by hematite. In fact, compositionally the ore is in most part typical to massive hematite ores seen in the broader Maremane Dome region, with very little contained manganese. The hematite is fragmentary and varies from large, highly fractured grains which take an apparent honeycomb texture, to grains that are free from such fracturing patterns (Fig. 33A and B). It should be noted that a similar texture is also observed in the shale-hosted breccia from farm McCarthy (Chapter 3). In some cases, the hematite grains were found to be enriched in aluminium along their boundaries, whereas disseminations of these same Al-bearing hematite grains are dispersed around the hematite grains (Fig. 33C). Darker grey domains in the honeycomb-textured hematite that appear like a replacement feature, (Fig. 33A) still represent hematite but with Al_2O_3 contents that can reach as high as 4 wt% (see Appendix B, Table B11).

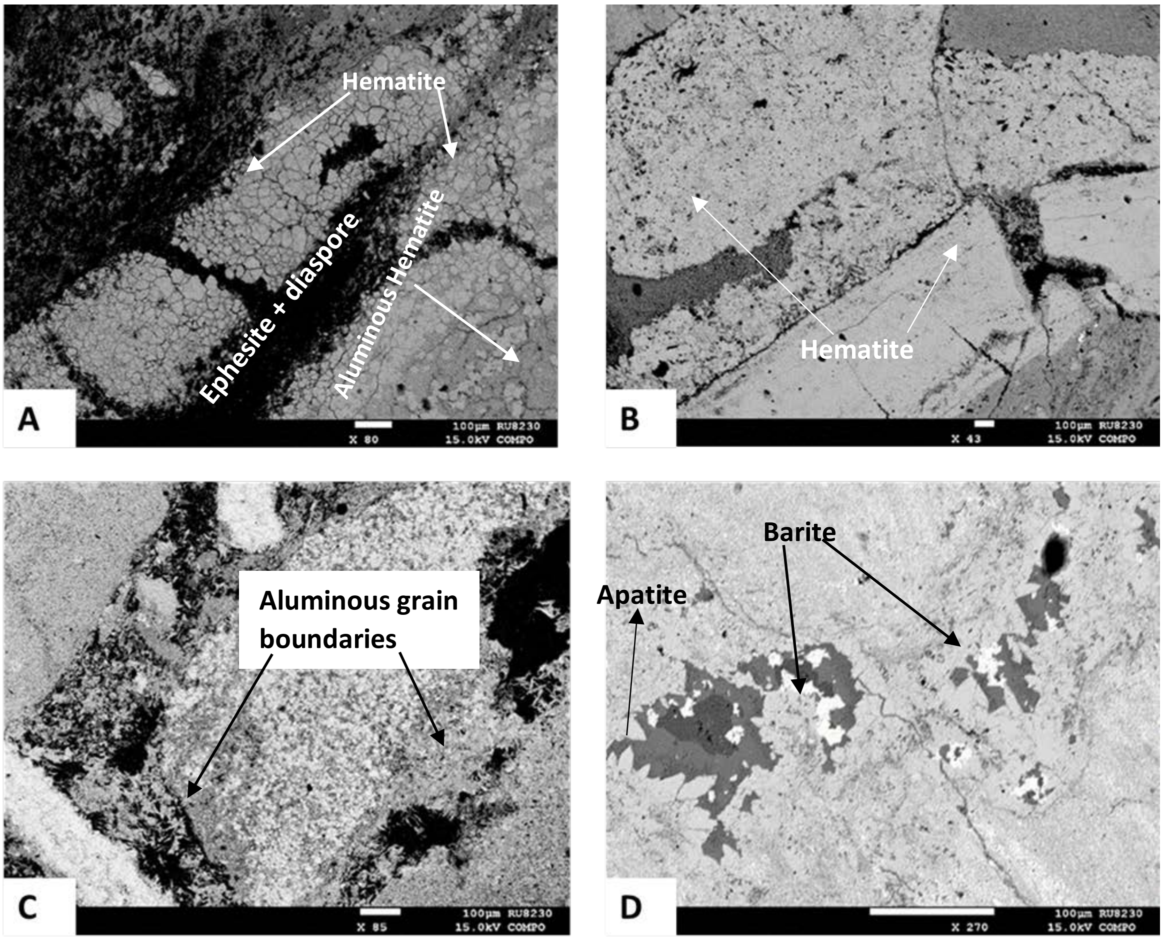

Figure 33: Back-scattered electron images of Leewfontein ore samples **A.** Apparent "honeycomb" textures in large hematite grains **B.** Hematite grains showing variable porosity and crystallinity **C.** Al-enriched hematite grain boundaries observed in selected samples **D.** Interstitial apatite and barite in massive hematite+bixbyite ore

Similarly, to the Bishop locality, the dark alumino-silicate groundmass was identified as a combination of ephesite and diaspore, mainly through a combination of SEM-EDS and XRD analyses (see Appendix B; Table B4) as grain sizes are extremely fine. However, as will be shown in the geochemical results later, the silicate assemblage here is Ca- and not Na-rich, and possibly represents an end-member case of Ca-substitution in ephesite resulting in margarite-like compositions. Apart from hematite and the ephesite-rich groundmass, other accessory phases in this unit include apatite and barite, with which significant manganese is locally found. The manganese content is manifested in the form of the mineral bixbyite (Fig. 33D), which is essentially a mixed Fe-Mn oxide. Apart from bixbyite, no other Mn-hosting mineral has been identified apart of occasional minor braunite grains, suggesting a clear distinction from the predominantly braunitic manganese ore at locality Bishop.

4.5 Geochemistry

The geochemical characteristics of the western belt ores obtained from Bishop and Leeuwfontein were explored using data from major, trace and rare earth element compositions. All values were normalised against PAAS as compiled by Taylor and Mclennan (1985). The direct association of the western belt ores with intercalated shales warrant the PAAS normalisation approach even stronger here (Plehwe-Leisen and Klemm, 1995; Gutzmer and Beukes, 1996). The significance of the shale association becomes all the greater when one considers earlier models which have proposed a replacement origin of manganese ore in the western belt at the expense of a shale protolith (Hall, 1926; Nel, 1929).

The geochemical approach presented in the following section includes also the five high-resolution sub-samples of a single laminated ore sample from the Bishop outcrop locality. In addition to expanding the western belt dataset, this high-resolution dataset can also in its own right provide interesting insights into small-scale geochemical variability and relationships, and their possible controls.

4.5.1 Bishop outcrop locality

Spidergrams for major elemental oxides in manganese ore from Bishop (Fig. 34), suggests an overall very consistent geochemical composition. The ore-zone is expectedly manganese rich, and this is evident in the corresponding spike of Figure 34 – where bulk MnO_2 is enriched relative to both PAAS by a magnitude of up to 1000-fold. Additionally, relative to the PAAS standard, the ore-zone shows enrichment in Fe_2O_3 and Na_2O, while TiO_2 and Al_2O_3 plot just above the PAAS line in all samples. Quantitatively, the metal enrichments translate into the following ranges: MnO_2: 26.4-42 wt%; and Fe_2O_3: 13.8-37.2 wt%). The manganese ores can therefore be regarded as ferruginous. Relative depletion in SiO_2, MgO, CaO as well as K_2O is also observed in all samples. Overall, variability between samples is small and is observed mainly in the alkali (K, Na) and alkali earth (Mg) content, as well as in Al oxide concentrations.

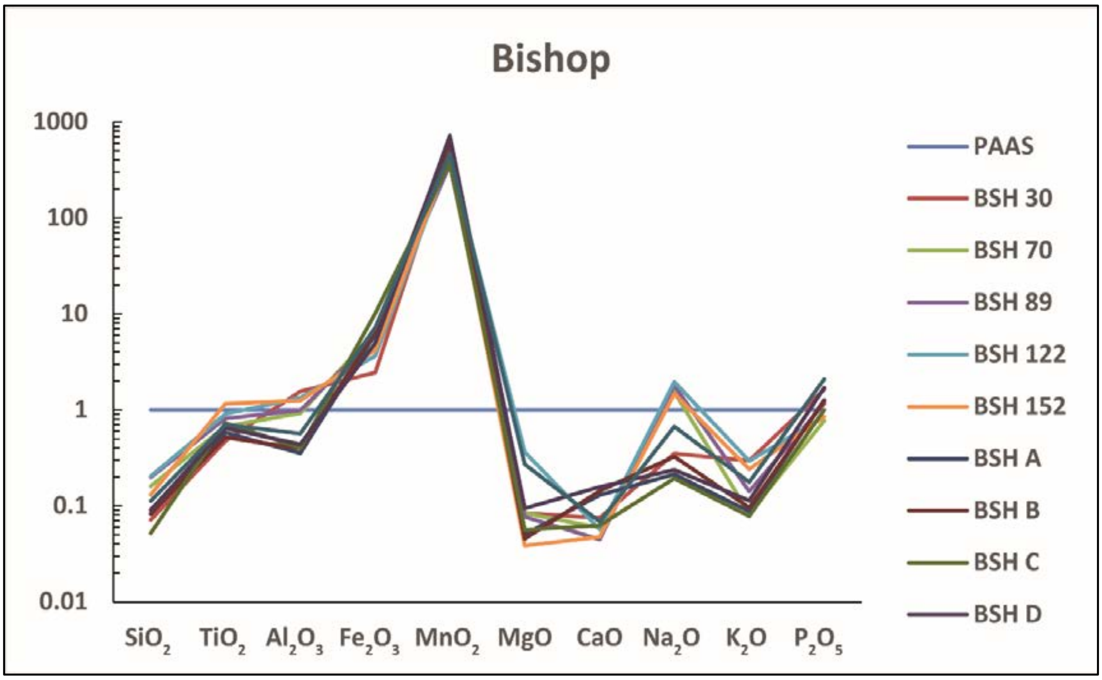

Figure 34: Spidergram for major element oxides of Bishop Mn ore samples, normalized against PAAS

Variations in trace elements plotted against PAAS for samples from Bishop are presented in Figure 35. Transition metals such as Co, Ni and Cu are enriched 4 to 5 times relative to PAAS. Consistent relative enrichments against PAAS albeit with large variability, can also be seen for the elements Sr (107 – 519 ppm), Ba (2235 – 11585 ppm), Pb (45 – 566 ppm) and less so for Y. By contrast Rb, Cs, V and U show clear relative depletions against the PAAS baseline, whereas Cr also plots below the same line for all samples except one (BSH D).

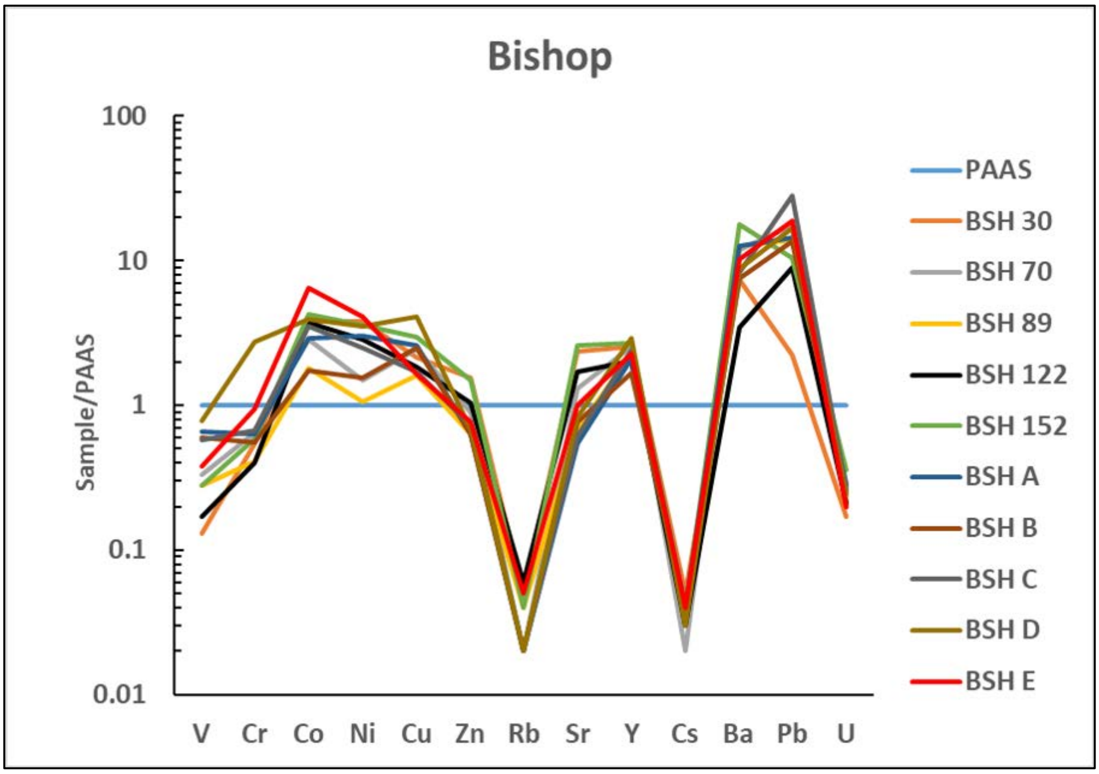

Figure 35: Trace elements for Bishop samples normalized against PAAS

In terms of PAAS-normalised REE results, Figure 36 illustrates the behaviour of all samples analysed. The profiles are generally comparable and broadly flat, with a gentle positive slope developing across the LREE, followed by a "hump" from Eu to Tb, and a very gently negative slope in the HREE. Probably the most characteristic feature in the Bishop dataset is the very strong negative Ce anomaly observed in all but one sample (BSH 89), which has a positive anomaly instead. It is also noteworthy that all samples display higher abundances for most analysed REE by comparison to PAAS.

Diagrams specific to the high-resolution sample-set from one outcrop sample of Bishop ore, are presented in Figure 37. These diagrams provide additional insights into the distribution of Fe and Mn on fine scales, which can be evaluated in conjunction with mineralogical observations presented in earlier sections. The binary diagrams shown are complementary to one-another and illustrate a relatively clear antithetic relationship between Fe and Mn, and a positive correlation between Mn and the alumino-silicate fraction of the rocks. Mineralogically, the above relationship essentially translates into an anticorrelation between the modal abundance of braunite and ephesite in the ores, and that of hematite as essentially the chief carrier of iron in the ore.

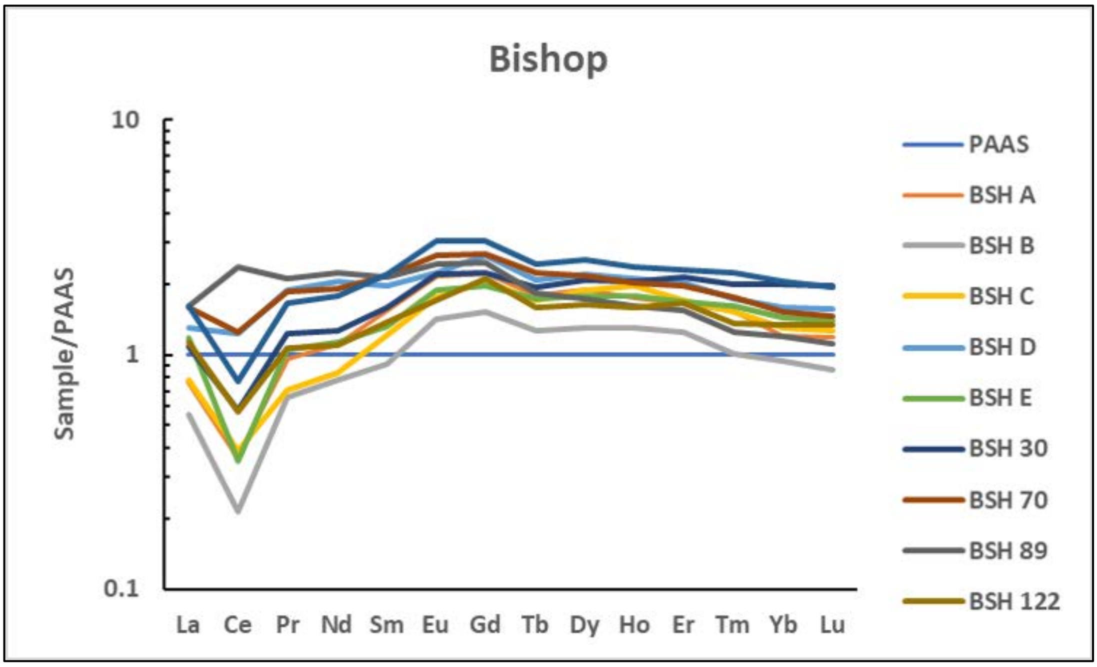

Figure 36: Rare-earth element patterns for Bishop manganese ore samples, normalized against PAAS

According to the supergene model as proposed by Gutzmer and Beukes (1996) for the genesis of the western belt ores, deposition of mineralisation is thought to have taken place in relatively restricted aqueous basins which developed at the top of karstified Campbellrand dolostones. The deposits would have comprised a layered succession of manganiferous wad, lateritic clay, and hematite pebble gravels in the open, fresh-water karstic depressions. The relationships revealed by the geochemistry of the Bishop mineralisation as shown in the diagrams of Figure 37, suggest that deposition of manganese and iron would have taken place in a decoupled fashion, in order to account for their statistical anticorrelation. Although the implications of this feature in terms of the paleoenvironment of deposition will be explored further in the next chapter, it is important to point out that fractionation (separation) between Fe and Mn is probably very difficult to be achieved in oxidised shallow lacustrine basins of a continental environment as alluded to by previous authors (Beukes *et al.,* 2002), and therefore deserves further discussion.

Finally, it is important to stress that from a compositional viewpoint, manganese ore and intercalated shale at the Bishop locality also reflect a high alkali content. Although abundances are highly variable from sample to sample, whole-rock concentrations in Na_2O can reach as high as 5.55 wt%, while K_2O achieves contents up to 1.5 wt%. These manifest mainly through the presence of ephesite mica which will be discussed further at the end of the chapter. Trace alkali earths in the same ores are also quite high, with Ba and Sr (hosted mainly in barite) reaching maximum contents of 4866 ppm and 915 ppm respectively, similarly with the eastern belt ores.

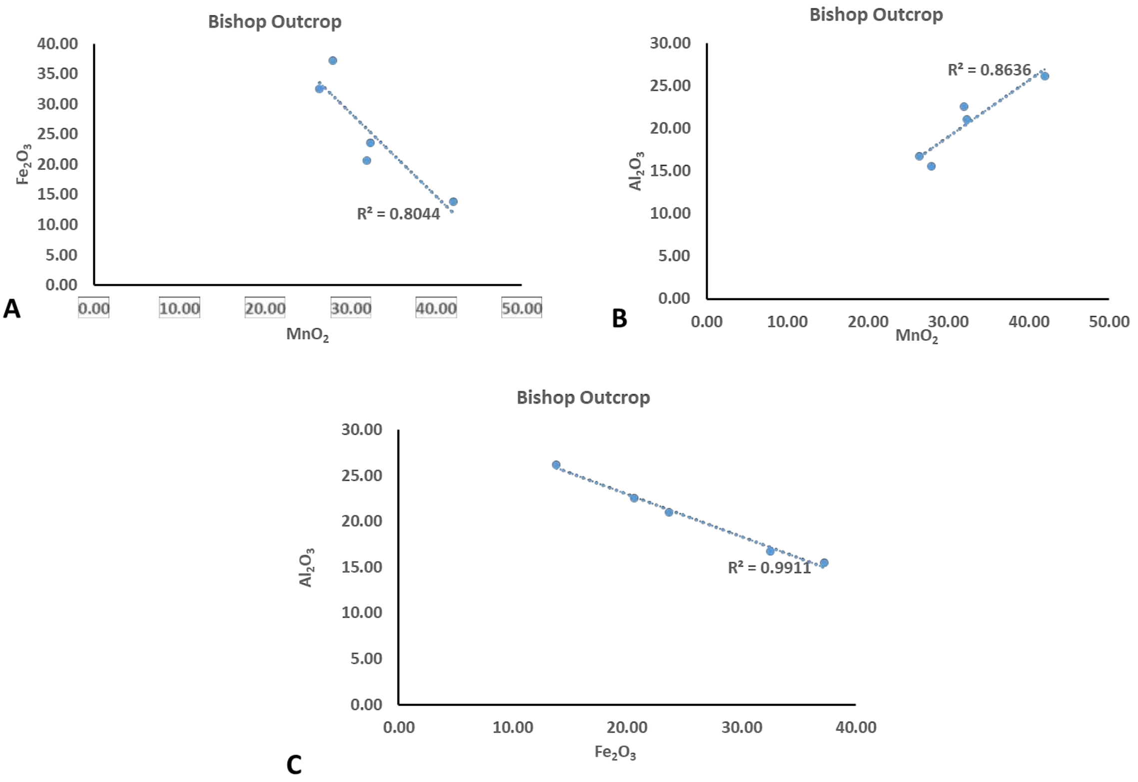

Figure 37: Geochemical relationships in cm-scale sub-samples from a laminated Mn ore specimen from Bishop. **A.** Binary plot reflecting an antithetic relationship between Mn_2O_3 and Fe_2O_3. **B.** A positivie correlation can be seen between Al_2O_3 and MnO_2. **C.** Another antithetic relationship exists between Fe_2O_3 and Al_2O_3

4.5.2 Leeuwfontein

The ore samples obtained from the Leeuwfontein drillcores from the broader Kolomela mine area in the southernmost Maremane Dome, are typically ferruginous and manganese-rich (Plehwe-Leisen and Klemm, 1995; Gutzmer and Beukes, 1996). However, the dominant compositions are very ferruginous with little Mn content, and Mn-rich domains occur relatively sporadically within an otherwise iron-rich ore. From a quantitative point of view, the elevated iron oxide (as Fe_2O_3) can range from as little as 7.7 wt% to as high as 93 wt%, at an average of approximately 45 wt% for the 12 samples analysed. Such high content would qualify parts of the ore as essentially pure hematitic iron ore. With regard to whole-rock Mn abundances, these are essentially bimodal, with five samples containing bulk Mn oxide from 13 to 28 wt%, whereas the rest have contents between less than 1 to just over 6 wt% (see Appendix C; Table C3). Concerning the remaining elemental oxides, bulk Al oxide concentrations are generally low with few exceptions, and the same applies with respect to bulk-rock silica, suggesting that the ores here are mostly oxide-rich. When Al values are high, they correspond to high CaO and not alkali contents which are very low here (unlike the situation with the Bishop ores). This points to the dominance of calcic ephesite as the main aluminosilicate species in this instance.

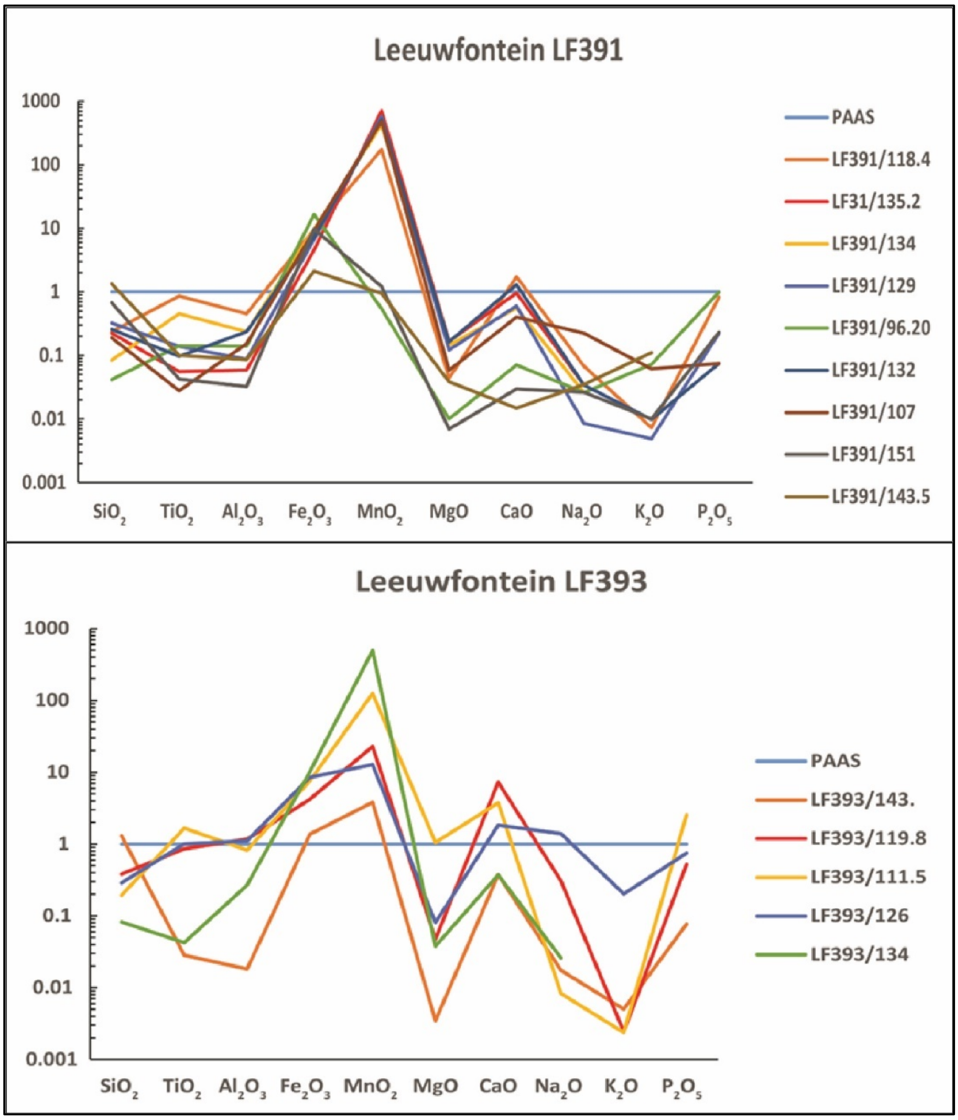

Figure 38: Two PAAS-normalised major element spidergrams for ore samples from the Leeuwfontein drillcores

With regard to PAAS-normalised trace element results, these appear to be comparable to the patterns observed in samples from the Bishop locality (Fig. 35). The ore samples here are also depleted in trace alkali elements such as Rb and Cs, while the transition metals Co, Ni and Cu show relative enrichments mostly above the PAAS baseline. Ba and Pb are also enriched relative to PAAS, pointing to the widespread presence of fine particles of barite in the ores.

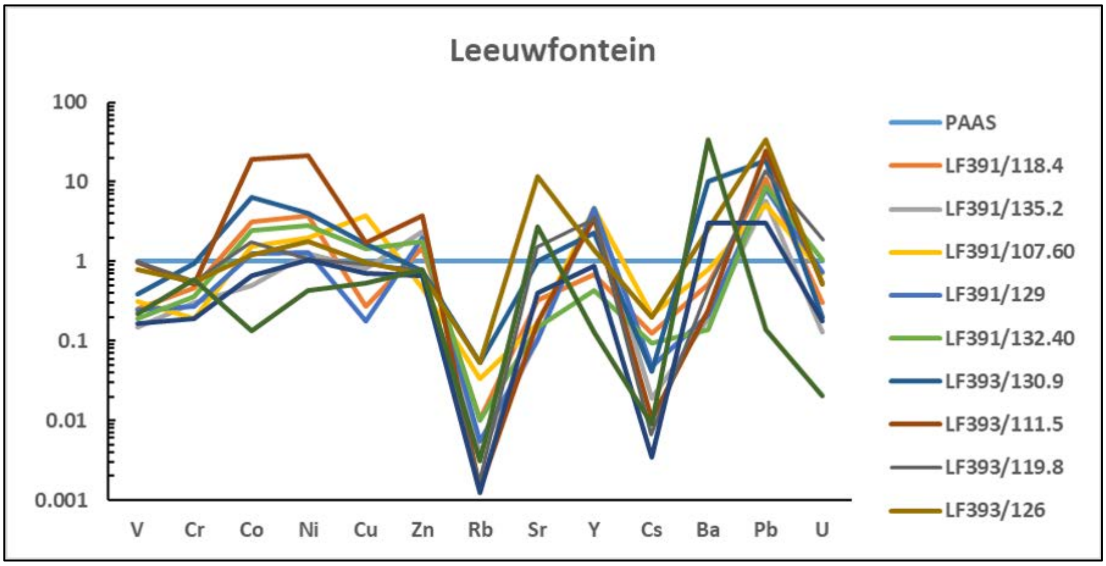

Figure 39: Spidergram for Leeuwfontein trace elements normalized against PAAS

It is important to note that the trace element spidergrams for the Leeuwfontein sample set appear to be much "noisier" that those shown earlier for the Bishop locality, and this applies also especially to the PAAS-normalised REE spidergrams shown below (Fig. 40). This is a function of the relatively large compositional range of the samples collected from the Leeuwfontein cores, which in some instances do not satisfy the strict definition of ore material but rather to variably ferruginous siliceous shale.

With respect to the PAAS-normalised REE spidergrams (Fig. 40), the situation is really quite complex and variable. The samples analysed can be broadly categorised into two groups: one group where the REE show an overall positive sloping trend from LREE to HREE, with a general flattening of that trend across the HREE (from Dy to Lu). This means that in terms of absolute abundances, most samples show LREE values below the PAAS baseline, but the HREE may plot well above that same line for some samples, depending on the steepness of the positive slope. A smaller number of samples however form the second group, which shows much flatter, shale-like patterns, with one of these samples plotting well above the PAAS baseline. Finally, with regard to Ce and Eu anomalies there is no consistent picture, although the majority of the Leeuwfontein samples record clear negative Ce anomalies, a feature which compares closely with corresponding REE patterns for ores from the Bishop locality.

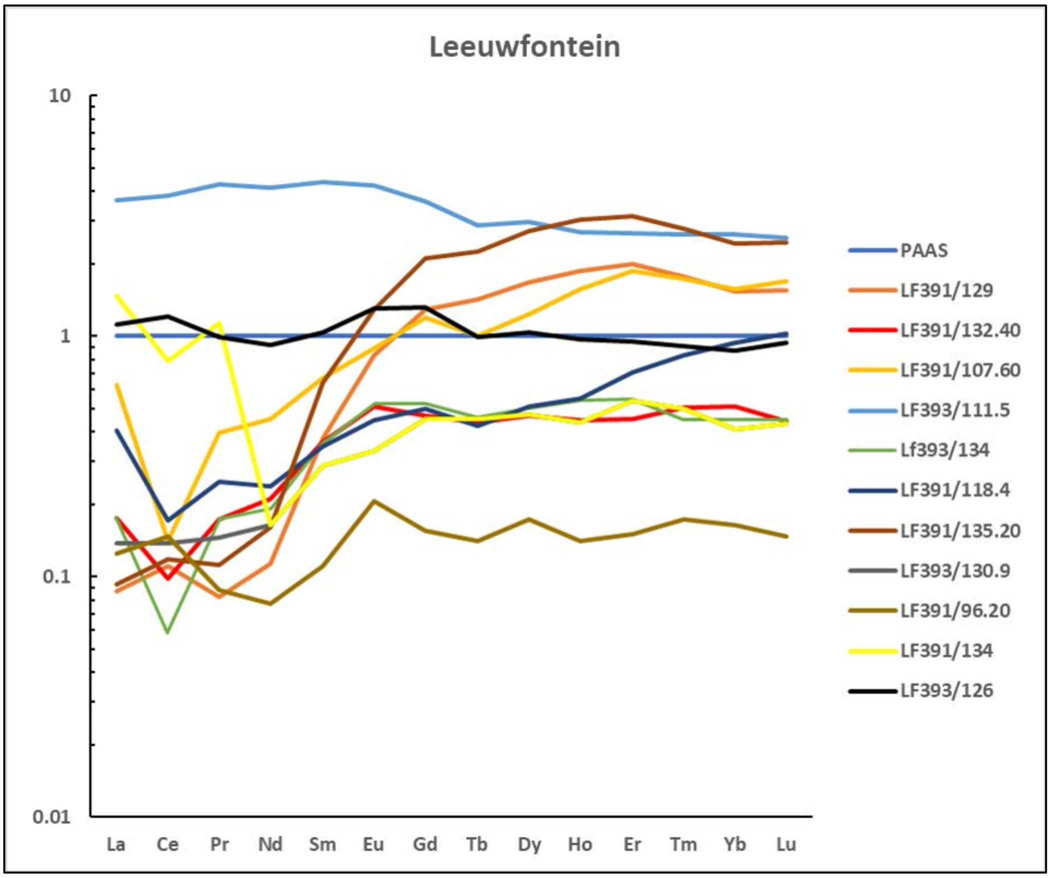

Figure 40: Spidergram for Leeuwfontein REEs normalized against PAAS

4.5.3 Bishop shale and the “ephesite problem”

The shale sub-samples extracted from the Bishop outcrop locality are geochemically dominated by a curious combination of high aluminium contents coupled with abundances of silica which in almost all instances is much lower than that of measured bulk Al oxide (Fig. 41). This association is very difficult to reconcile through classic mineralogical combinations of common detrital minerals in shales such as quartz and sericite, which would result in much higher silica abundances over Al oxide when analysed by bulk-rock techniques, regardless the modal combinations from sample to sample. Moreover, the high abundance in Na in the same samples suggests an aluminosilicate mineral that is sodic and not potassic like the common sericite. Therefore, paragonite mica would make a fitting solution to the mineralogical identity of the main mineral present.

Application of SEM and XRD analyses on sections and corresponding powdered samples of the shales have revealed that the dominant aluminium species to be the mineral ephesite, which stoichiometrically contains in its structure far more Al oxide than silica and therefore satisfies the bulk geochemistry of the samples best. However, the total sum of elemental oxides for one single analyses of that shale returns a deficit of 4.53 wt% which cannot be readily accounted for. Whole-rock Ba contents in the rock can be as high as 11000ppm, but this only makes a small part of the missing 4.5wt%. It is therefore deemed likely, based on the stoichiometry of ephesite, that the rest is made up of Li oxide, which is in any case an integral component of the ephesite structure and an element that also distinguishes ephesite from paragonite.

It is therefore clear that at least part of the Bishop ores are quartz-free and ephesite-rich, and these are compositional characteristics that distance these shales from any other counterparts in the broader region. It is of course not the first time that ephesite is reported in association with the ores of the PMF, as Gutzmer and Beukes (1996) also make mention of this mineral in their work. The presence of ephesite as the main matrix mineral in the shale though is arguably quite extraordinary and matches no other shale in the region. Cousins (2016) and Land *et al* (2018), for example, have reported extensive mineralogical and geochemical results from the Mapedi/Gamagara shales which include hematite, quartz, muscovite and minor chlorite as the main minerals in the rocks and make no mention whatsoever of ephesite or even paragonite. The implications of this mineralogical "anomaly" will be revisited in the final chapter of this thesis.

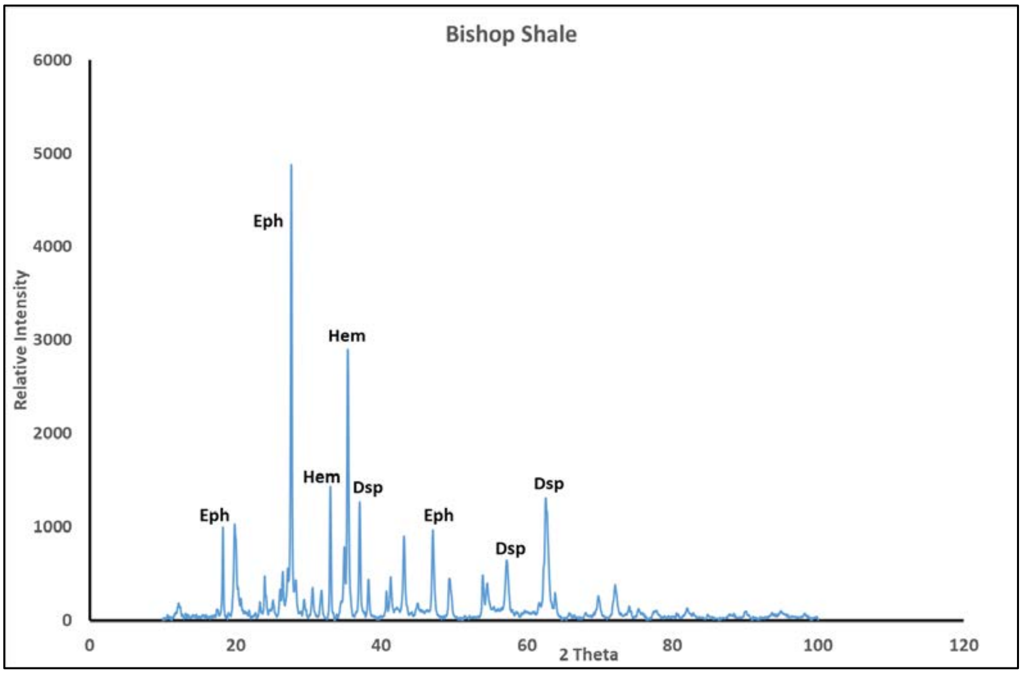

Figure 41: XRD spectra showing dominant species in the Bishop shales

5 Discussion

5.1 Comparisons between different manganese ore types in the PMF

In reviewing manganese deposits in the PMF, a starting discussion point concerns the traditional separation of these deposits mainly on the basis of their bulk iron and silica content; namely, the western belt ores are thought to be typically ferruginous while the eastern belt deposits are more siliceous (Plehwe-Leisen and Klemm, 1995; Gutzmer and Beukes, 1996). Gutzmer and Beukes (1996) compared the ferruginous western belt ores to those of the Lindener Mark in Hesse, Germany, and further argued for a distinctly "lateritic" character for the western belt ores. A closer examination of ore samples analysed from the western belt for this study, however, does not readily reflect that lateritic character texturally, mineralogically and geochemically, especially when considering the characteristic laminated nature of western belt ores, at least locally (e.g. Bishop outcrop locality). For such laminated ores to occur, one would need deposition in a localised aqueous setting in combination possibly with a prevailing lateritic background environment of formation (Gutzmer and Beukes, 1996).

Physically, all ore samples investigated in this study regardless of location (i.e. from the eastern or the western belt families) are massive, indurated manganese ores. Partial exception to this is the McCarthy deposits, which exhibit a much more friable saprolitic texture which supports a recent supergene influence. Besides being massive, the distinct laminated character of the ores at Bishop and the intercalations with unmineralized shale, signifies a sedimentary origin or, at worst, a pseudomorphic replacement one against a sedimentary protolith. This observation clashes with the suggestions of earlier workers such as Gutzmer and Beukes (1996) who state that supergene alterations tend to obscure sedimentary bedding and any original textures of the original ore deposits. Clearly, at least at the Bishop outcrop locality, such an effect does not define the said deposits.

The intercalated shales associated with the Bishop ores also offer some insightful results which may add another new dimension to the possible fluid history of these deposits. Bulk geochemical analysis shows a conspicuous relative enrichment in Al_2O_3 in these shales, which is almost twice as high as the SiO_2 content in the same samples. The mineral ephesite, a sodium lithium mica restricted to quartz-free assemblages associated with laterites at the type locality of Turkey, is clearly a dominant species in these shales and adequately explains this excess Al_2O_3 abundance. Due to its Na enrichment, it also reflects no other shale in the broader region from a compositional viewpoint: for example, the Mapedi/Gamagara shales stratigraphically associated with the ores, are known to be enriched in potassium instead, while containing negligible Na (Land *et al.,* 2018). Moreover, average Mapedi/Gamagara shales contain typical bulk-rock SiO_2 contents ranging from 52.6–73.4wt%, and therefore show no relative Al enrichment. As indicated above, the most widely developed occurrence of ephesite has been reported from metamorphosed bauxitic environments as well as contact metamorphism of compositionally similar rocks (Velde, 1971). This depletion in SiO_2 in the shales combined with the abundance of ephesite in the Bishop locality (and also, to some extent in the Leeuwfontein ores too), suggest a possible alteration effect upon the shales related to fluid circulation and metasomatism. The physico-chemical conditions of such metasomatic processes would not have affected aluminium, which is soluble only under extremely acidic or alkaline conditions (Robb, 2005). By contrast, preferential solubility of silica and addition of Na and Li under alkaline conditions could account for the Si deficiency of these shales and the formation of stable ephesite.

Additionally, there is other textural evidence indicative of fluid-rock interaction in rocks and ores of both the eastern and western belts. The majority of quartz clasts hosted in the red shale breccia discussed earlier in chapter 3, are highly fractured and suggest possibly the effects of brittle deformation and associated mottled texture development in quartz clasts, aided by simultaneous fluid-flow through permeable rock. These are clearly late fluids indicated by recrystallized quartz space-fills within the dominantly altered clasts. Chalcedonic silica formation can also be attributed to the same process. This sort of "cataclastic" fragmentation can also be seen in the Leeuwfontein ores which have a distinct assemblage of incipiently cracked hematite clasts forming "mosaic" textures. It is therefore possible that fluid circulation associated with brittle deformation, and itself related possibly to thrusting as documented regionally to the western part of the Maremane Dome, may have been the major causes behind many of the textures and geochemical effects seen in the rocks across all regional types of Mn mineralisation.

5.1.2 Insights from major, trace and REE relationships

Diagrams utilising trace elements and REEs plotted after normalisation against PAAS, were constructed as a means of effectively comparing the eastern and western belt deposits in order to elucidate their modes of origin and draw comparisons where possible. The REE can be regarded as especially important, as they tend to be relatively conservative to a variety of fluid processes but can also be mobilised under diverse environmental and fluid settings, such as supergene *versus* hydrothermal environments. Therefore, despite the fact that diagenetic processes may modify original sedimentary or residual accumulations and thus impart both chemical and textural alterations to rock resulting in an overprint of primary signatures (McFarlane and Holland, 1991), the REEs can still shed some light into the protolith signature of the ores under examination (Gutzmer *et al,* 2008). In investigating the controls on REE profiles in iron-ore deposits, Gutzmer *et al* (2008) concluded that a distinct empirical separation can be made between supergene and hydrothermal deposits based on their relative HREE and LREE enrichments. According to Gutzmer and Beukes (2008), hydrothermally generated iron ore deposits are typified by a relative depletion in LREEs with a positive slope developing towards the HREEs. By contrast, supergene iron ore deposits develop an essentially opposite REE behaviour, showing relative enrichment in LREEs, a negative slope in PAAS-normalised concentration from Eu to Ho, and low abundances of HREE (Fig. 42). Although the diagrams and interpretations of Gutzmer and Beukes (2008) pertain to iron ores, the close spatial and stratigraphic association in the PMF between iron ore and manganese ores and the interpreted paleo-supergene origin for both ore types (particularly in the eastern belt situation), means that possibly similar considerations could be applied in both end-member cases (i.e. iron and manganese ores alike).

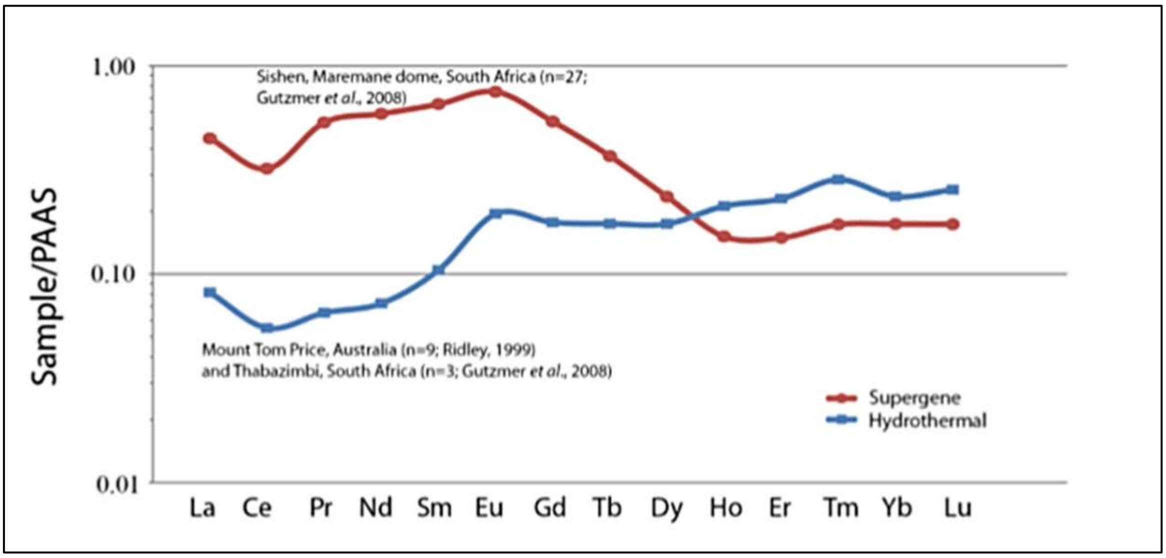

Figure 42: Spidergrams showing the distinct supergene and hydrothermal REE signals relative to PAAS (Gutzmer and Beukes 2008; modified after Land, 2013).

The PAAS-normalised spidergrams of Figures 43 and 44 represent average data for trace elements and REE from all localities tackled in this thesis. Beginning with the trace element results (Fig. 43), one can observe a general similarity in the data from all examined localities. The main points to be extracted are the consistent relative enrichment in selected transition metals (mainly Co and Ni) over others, the notable depletions in trace alkali earths (Rb and Cs) and sharp positive spikes in Ba and Pb well above the PAAS baseline.

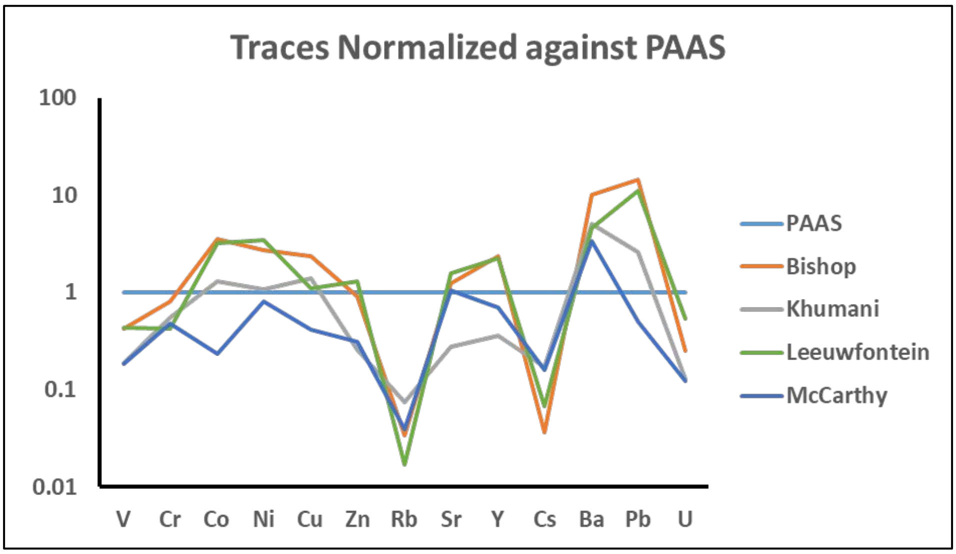

Figure 43: PAAS-normalised spidergrams for averaged trace element averages from the four localities studied

With regard to the averaged REE data, the main observation upfront is that the profiles from the different localities are relatively flat with a generally very gentle positive slope from LREE to HREE. This kind of signature therefore shows an overall similarity not all that different from an average shale. More importantly, however, it also shows a striking similarity in all cases with the hydrothermal signature of Gutzmer and Beukes (2008) as depicted in Figure 42 above. This, of course, is in direct variance with prevailing suggestions in the literature that the PMF ores are predominantly ancient supergene in origin and, if anything, it more readily supports a hydrothermal origin instead.

A further and closer look at the REE signatures exploits the presence of anomalies in the behaviour of Eu and Ce and their controls. These are two REE that are redox sensitive and therefore may enclose information of oxidative or reductive processes taking place during ore formation. Beginning with the massive ore samples, all but one show a variable but consistent negative Ce anomaly. This is an interesting feature, given that the preferential adsorption of Ce^{4+} onto Mn- and Fe-oxyhydroxide particles which is especially common in alkaline fluids

(Elderfield *et al*, 1981; Nelson *et al*, 2003), can result in positive Ce anomalies in Mn (IV) oxide-rich deposits. The negative Ce anomalies are therefore also not supportive of a supergene origin for the PMF ores under study.

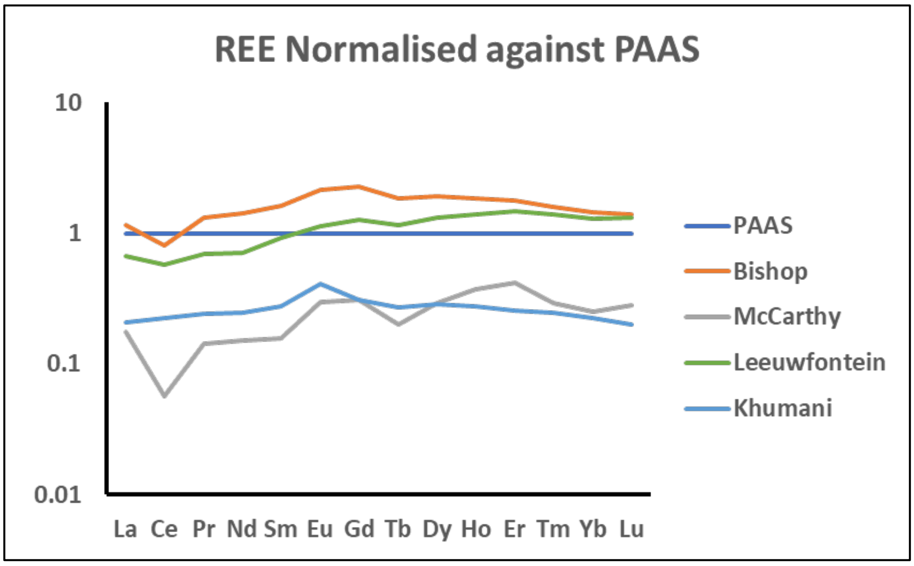

Figure 44: PAAS-normalised **s**pidergrams for averaged REEs from the four localities studied

With regard to Eu anomalies (positive or negative), these are often quite difficult to interpret as they may represent different effects and processes from one sample to the next. In order to extend the discussion, the two shale samples that were sub-sampled from locality Bishop (western belt ore) have been included in the considerations (Fig. 45). Positive Eu anomalies are seen in some samples of eastern belt ore as sampled from the Khumani drillcore, and that is reflected also in the corresponding average spidergram of Figure 44. A significantly higher than expected intensity of the positive Eu anomaly can be observed in the shale samples from Bishop, as recorded in the PAAS-normalised diagram of Figure 45 below.

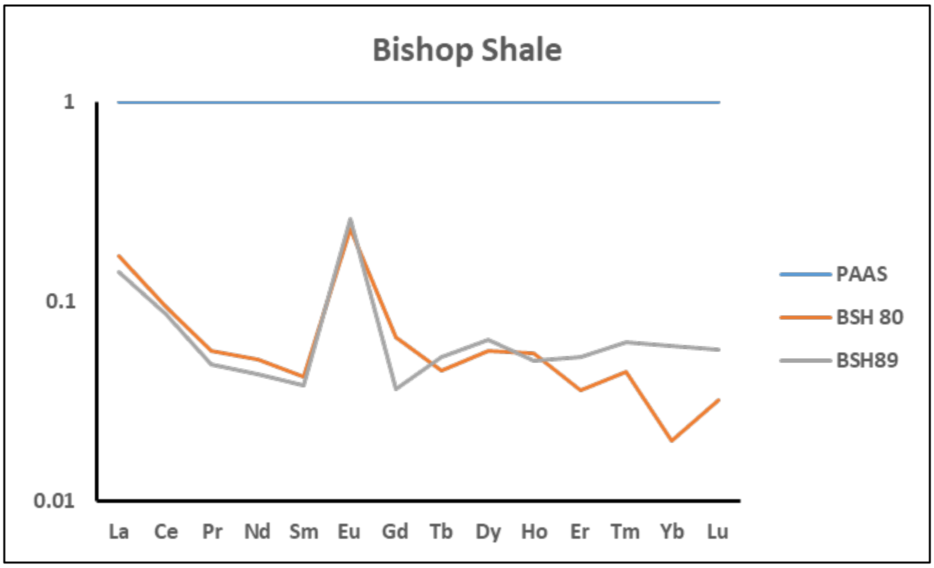

Figure 45: PAAS-normalised REE spidergram of intercalated shale at locality Bishop

It is of course perfectly possible that the Eu anomaly in the shales at Bishop may signify a detrital signal from the particulate material that makes up the rock. However, the fact that a positive Eu signal is seen also in eastern belt ore, may provide reasons to consider a common origin for it. Positive Eu anomalies have been traditionally explained due to its partitioning into feldspar, which is a mineral seen in the eastern belt ores in the form of albite and lesser K-feldspar. They may also be the result of a hydrothermal signal from fluid-leaching of rocks such as orthogneisses of an acidic primary composition characterised by positive Eu anomalies and Ba+Sr enrichments (Terekhov and Shcherbakova, 2006). The imprint of such signals during subsequent fluid-rock interaction and feldspar formation may therefore be a feasible explanation also for the Eu behaviour in the PMF ores.

The main conclusion gleaned from all the above, is that there seems to be no distinct geochemical evidence in support of the supergene model of ore formation, or any clear-cut compositional distinction between the two major end-member ore types examined. To further establish the latter point, ternary diagrams depicting the most dominant oxides in these deposits were drawn (Fig. 46). Ore samples from both the western and eastern belt were specifically plotted on two complementary diagrams utilising the main rock-forming elements in the examined ores, namely Si, Mn, Fe and Al, in the form of their elemental oxides as measured analytically. The main reason for this application is to simply check for any apparent clustering of the examined ore-types, based on the classic argument in the relevant literature that the eastern belt ores are siliceous whereas the western belt ores are ferruginous. If this was true, then separation of the two classes of ore at the PMF should be statistically possible and evident on such diagrams.

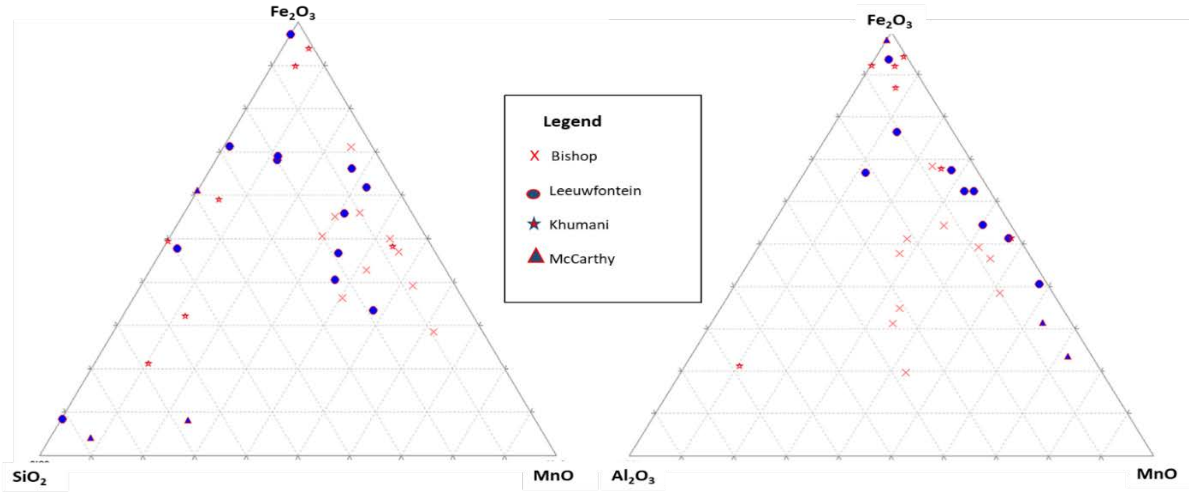

Figure 46: Ternary plots of major oxides for ores from the eastern and western belts of the PMF

Although the silica content is very high in the eastern belt deposits by virtue of the abundance of chert fragments in the ore (an intrinsic trait of the Wolhaarkop Breccia) separation on the basis of bulk iron content is definitely not achievable, and therefore the whole distinction between ferruginous and siliceous appears to be somewhat misleading and biased.

5.1.3 Alkali enrichment and inferences for fluid-rock interaction

The concentration of alkali elements in the studied manganese deposits of the PMF can be considered as high and potentially anomalous. This observation appears to be at direct odds with the suggested supergene environment of formation, as the elements that define that alkali signature would be among the first to be leached out in such conditions, with possible exception the case of Ba when hosted in the highly insoluble mineral barite. It is therefore inferred here that the observed alkali concentrations provide strong circumstantial evidence for some kind of metasomatic alteration and enrichment. As reported earlier in this thesis, the presence of alkali minerals recording such metasomatic origin exist interstitially in the ore at variable abundances but are also present in western belt ores. Previous studies have also documented this alkali enrichment in the eastern belt (Wolhaarkop breccia) manifested in the form of minerals such as sugilite, serandite, norrishite, armbrusterite and albite, documented from a borehole intersection of Wolhaarkop breccia at Bruce iron ore mine (Moore *et al*, 2011).

Aegirine, albite and Ba muscovite and Ba carbonate (witherite) are amongst the minerals also reported in other earlier studies (Gutzmer and Beukes, 1996). To these, one should add the occurrence of ephesite in the western belt ores at Bishop, and its calcic variety at Leeuwfontein. Barite is another mineral that is omnipresent throughout the PMF in diverse Mn ores of all types, as has also been observed in this study. Noteworthy, for example, is the close textural association of bixbyite with barite particles in Mn-rich zones of the Leeuwfontein drillcores in the southern fringe of the PMF.

This kind of alkali enrichment illustrated in the previous paragraph appears to be clearly exotic to the rocks and ores under study, and calls for a metasomatic introduction through fluids. It is certainly an enrichment that cannot be attributed to a common protolith such as a carbonate rock or a banded iron-formation which are rocks known to be very low in alkali contents. It also cannot be explained through ore-forming systems of residual enrichment such as supergene environments, due to the general mobility of alkalis during chemical weathering, and it is also not consistent with fresh-water metalliferous deposits as has been proposed previously (Gutzmer and Beukes, 1996).

During SEM-EDS analysis of samples from both western and eastern belt deposits, the presence of halogens such as Br and Fl is detected within the ores (Appendix C; Table C11). Provided that these measurements are reliable and do not represent some kind of superficial contamination of the samples during processing, they may provide additional clues. F in particular, is a strong ligand and its presence in a fluid enhances metal dissolution, aqueous mobility and finally deposition at suitable sites. The presence of such anionic species has in fact been reported before by De Villiers (1944, 1956,1960). The said author reported the presence of Cl, Li, Na, and B in the ores that he investigated, and attributed these to a magmatic hydrothermal source for the deposits. These anionic species however, do not have exclusive magmatic associations but have also been commonly found in brines of non-magmatic origins. Bąbel and Schreiber (2014) state that elements such as Cl and Li and the rarer F and Br are indicative of common, easily soluble salts. Based on the elevated alkali element content, a hydrothermal brine therefore seems a likely fluid source. It is important to mention in this context that B was also detected in this study in the matrix of eastern belt ore samples from Khumani, specifically making up several wt% of a barite grain (see Appendix C; Table C12). High B concentrations can be achieved in natural brines, for example through evaporation in closed basins (Grew, 2015). Kolodny *et al* (1980) also attributed the presence of B to seawater or seawater-derived evaporated brines in the Mishash chert breccias from Israel. High B concentrations and accompanying abundance of associated minerals such as barite and calcite, provide additional leverage for a brine source (e.g. Bąbel and Schreiber, 2014). A magmatic source of such brines however is very difficult to be accounted for, in view of the regional geology and general absence of felsic or alkaline igneous rocks that would lend support to the contention of De Villiers (1944, 1956,1960).

5.1.4 The Supergene altered McCarthy Ore

Two Wolhaarkop breccia variants and associated eastern belt mineralisation were analysed during this study: one fresh (Khumani) and the other evidently altered by supergene fluids (McCarthy). A few additional lines interrogating their physical and chemical attributes in a comparative sense, are presented below.

The manganese ore at McCarthy appears to be of a much higher metal content than the Khumani equivalent, and certainly represents a more manganese-rich end member. This is probably related to the fact that it has been affected by interaction with supergene fluids. This would have resulted in breakdown and loss of alkali-rich minerals such as the sodic phases mentioned above (albite, serandite, etc) and residual enrichment in Mn. Potassium would however have been somewhat conservative to this process, as it evidently found home in the structure of stable cryptomelane. The textural evidence of relict braunite in a cryptomelane-rich matrix at McCarthy, suggests that the precursor mineral must have been dominantly braunitic, just like with what is seen in the Khumani drillcore material. Moreover, the Mn ore at Khumani is very ferruginous and somewhat transitional to iron ore mined in the same region where the core was drilled. This would also have impacted negatively the Mn grade at Khumani. The abundant crosscutting veins of cryptomelane through the McCarthy ore and the relatively shallower position of it in relation to the present surface, is testament to the later supergene fluid interaction that it has gone through. Finally, the relative depletion in silica in the McCarthy samples and the fact that some braunite analysed from the same ore appears to show a deficit in contained Si (Appendix B; Table B10), suggests that the supergene effect was also open with respect to silica (Gutzmer *et al,* 2008). Therefore, partial loss of Si during secondary cryptomelane formation would itself have contributed to higher Mn grades at McCarthy as compared to Khumani. All the above highlight the complexity in the depositional and fluid history of the PMF ores, and how apparently similar ore types can still register diverse fluid processes and effects in ore mineralogy and chemical composition.

5.2 The Campbellrand Dolostones as manganese and iron source

The changes in geochemical and mineralogical composition experienced by iron and manganese deposits *via* interaction with fluids is not a new topic in literature. In fact, it has been documented quite recently in some parts of the PMF in the form of strong alkali metasomatism and generation of some quite rare new alkali species (e.g. Moore *et al,* 2011; Costin *et al.,* 2015). It also characterises ores of the KMF further north from the PMF, which have also undergone substantial alkali addition (e.g. Tsikos and Moore, 2006). The current traditional supergene model for the PMF deposits describes the source of the manganese ores to be the underlying Campbellrand dolostones. However, the interaction of a dolomitic substrate and meteoric water fails to explain the high alkali content found in the PMF ores. Based on the relative degrees of enrichment recorded in the manganese ores, the supergene model is called into question as fundamental process behind formation of these deposits. The possibility of different metal source/s and ore-forming mechanisms, or at a minimum, secondary hydrothermal interaction overprinting earlier formed Mn mineralisation, therefore needs to be considered further.

When dealing with potentially metasomatically altered rocks, the pressing question that arises concerns the gains and losses made from the transition from original to altered rock. These changes, in essence, inform the type of fluid that interacted with the rocks in question and the nature of mass transfer as it interacted with them. Once alteration has been examined through petrographic and field relations as well as geochemical evidence (Grant, 1986), the basis for qualitative and quantitative gains and losses in mass must be determined. This differs per researcher approach, and hinges essentially on the choice of geochemically immobile constituents marking conservative behaviour, as this would define the baseline for relative gains and losses. In many instances, authors may assume constant volume of rock as that baseline; others rely on specific elements that are generally immobile in fluids, like Al, Ti or Zr (Grant, 1986). Whatever the choice, a thorough understanding of the nuances of each case study is always vitally important.

The isocon approach of Grant (1986) appears to be a simple yet powerful tool to assess mass changes during metasomatic alteration, because of its minimal data manipulation approach. The isocon analysis is a simple tool that effectively estimates the mass and/or volume change as well as concentrations in mass transfer during metasomatic processes (Grant, 1986). It is a simplified graphical solution used as an alternative to the much more complex mathematical approach that Gresens introduced earlier in 1967, by means of a mathematical equation that aims to solve the same volume and concentration relationships in metasomatic systems. The graphical representation of the volume or concentration loss and gain is accomplished by plotting the altered composition against the original composition, while the species that are immobile define the isocon *via* a straight line through the origin. Although several attempts have been made to refine the isocon approach (Baugmartner and Olsen, 1995) and several discussions have raised some questions over its application, Grant's approach remains popular and will be implemented in that way for this particular exercise.

As also indicated in the opening chapter of this thesis, the carbonate rocks (dolostones and limestones) of the Campbellrand Subgroup are the universal footwall of the PMF ore deposits, and have been suggested in previous studies to be the source of the manganese found in the deposits of the eastern and western belts higher up in the regional stratigraphy (Gutzmer and Beukes, 1996). This, as elaborated on in previous chapters, is thought to have been achieved either through a process that involves karstification and accumulation of the residual material at the base of karstic sinkholes (eastern belt ores); or in localised aqueous basins developing in such depressions (western belt ores). The isocon application that follows will therefore assume such locally sampled dolostones as the original rock (and thus source of manganese), and the corresponding overlying ore in each instance as the altered rock.

Two carbonate samples from two localities representing the western belt (specifically the Bishop locality) as well as the eastern belt (Khumani drillcore) were sourced for this exercise. Chemically these dolostones do not show any marked differences from a geochemical viewpoint (see Appendix C, Table C9 and C10). They all show typical compositions of carbonate rocks with no alkali enrichments, thereby establishing a clear lack of correlation with the elevated alkali elements in the manganese ores. In both end-member cases, the Na_2O content is below the detection limit, while the K_2O content does not exceed the value of 0.2 wt%. CaO is obviously of no consideration as it is by definition an essential rock-forming component in dolostones, and the same applies with regards to MgO. In terms of the major elements that are considered as the chemical basis for the separation between western and eastern belt deposits – namely Si and Fe abundances – again no major distinctions are noted between the two samples. The manganese content is also very similar for both samples. Sr, Ba as well as transition metals like Zn, Cu, V and Pb are also present in low concentrations, all ranging below 40 ppm.

It is widely documented that in a supergene environment, HFSE such as Zr and Ti, as well as Al, behave generally in an immobile manner and concentrate in the weathering profile, whereas alkali earth and alkali metal elements are typically mobile (Grant, 1986; McLennan *et al.,* 2003; Angerer *et al.,* 2012). Additionally, the immobility of iron and effective removal of silica, calcium and magnesium is often invoked in the formation of supergene-related high-grade iron ore (Gutzmer *et al.,* 2008). In a residual supergene model as described for the PMF deposits, it would thus be expected that iron and manganese are immobile and passively enriched. Based on this model, the assumption is therefore made that manganese would also be a conservative element in these deposits. The two isocon plots constructed therefore contain a "constant manganese line" which is shown by a green line to denote its postulated immobility.

On the other hand, the blue line in the two isocon plots represent an isocon for HFSEs that are likewise expected to have remained immobile in a supergene environment of manganese ore formation against a given protolith. Such elements include Nb, Zr, Ta, Hf and Ti (Grant, 1986; McLennan *et al.,* 2003) and would therefore be expected to plot approximately on or about the same isocon. This, however was not quite the case here and instead the only two elements that appeared to align were Zr and Nb which in the end were used to construct an immobility isocon (Figs. 47, 48). These elements also did not align with the assumed immobile Mn (and Fe), which suggests that both metals must have been relatively mobile by comparison to the HFSEs. The use of Al as another immobility index was not considered for two reasons: the first is because it is an element that may be mobile under certain conditions either in fluids or through physical addition from airborne clay particles during weathering, and therefore prove spurious; and secondly, because inclusion of more than two immobility isocons would make extraction of information from the plots rather cumbersome.

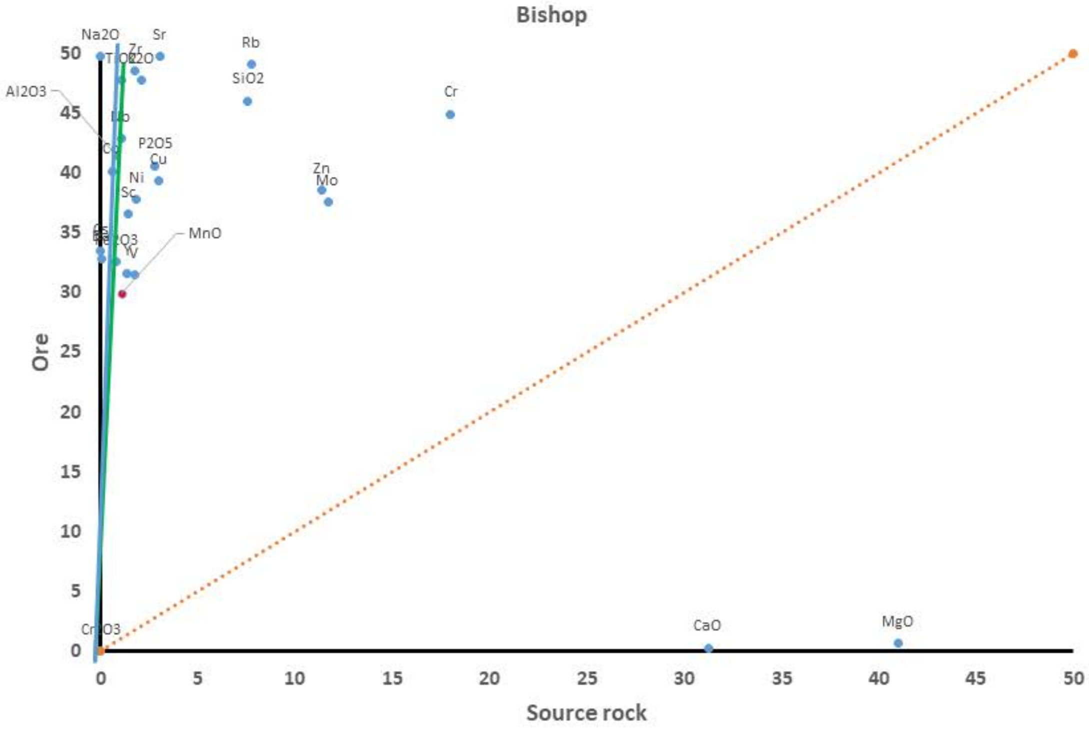

Figure 47: Isocon diagram illustrating mass balance relationships between Campbellrand dolostone as parent rock, and Mn ore from the Bishop outcrop locality as the altered equivalent (western belt).

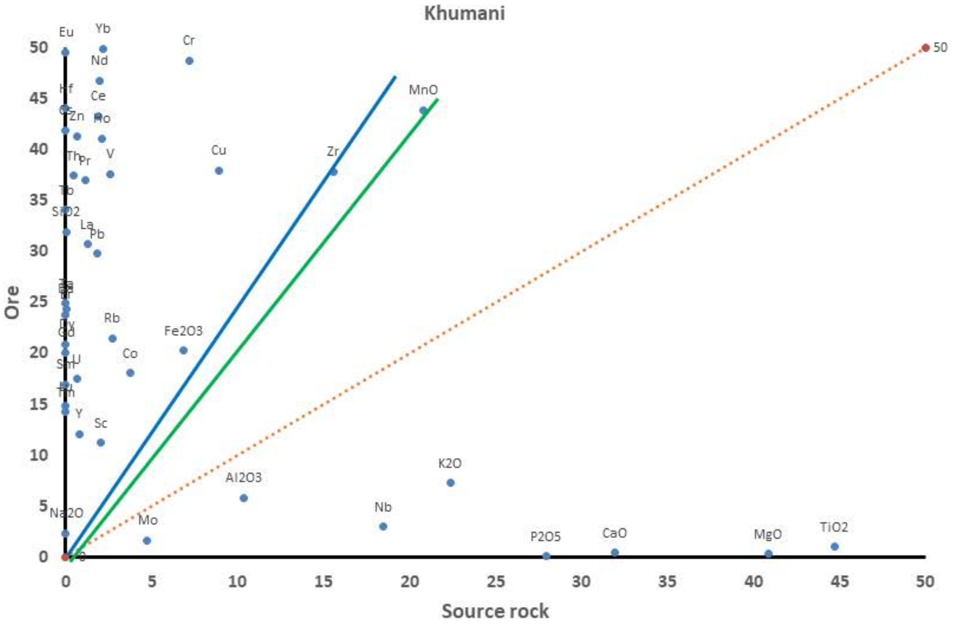

Figure 48: Isocon diagram illustrating mass balance relationships between Campbellrand dolostone as parent rock, and Mn ore from the Khumani drillcore as the altered equivalent (eastern belt).

The isocon diagrams of the Figures 47 and 48 above reveal some interesting insights into the geochemical mass balance of the ore-forming systems that produced the eastern and western belt Mn ores. The first obvious feature is that the immobility isocons for manganese and the selected HFSEs, have a very steep slope which agree with the expected very high loss of mass from the parent dolostones required to produce very high Mn accumulations in residual deposits. For that to happen, practically all the original Ca, Mg and CO_2 from the rock has to be removed through supergene weathering. The immobility isocons are a lot steeper in the Bishop case (western belt) compared to the Khumani case (eastern belt), suggesting that the Western Belt ores require quite extreme levels of leaching compared to those of the eastern belt, in order to produce the corresponding manganese ores.

In view of the chosen isocons in both end member cases, some further conclusions can be gleaned concerning the behaviour of the other elements. Firstly, in the Khumani case (Fig. 48), it appears as if loss of Al and K as well as Nb and Ti would also be required to produce the eastern belt ores, if Mn is fixed as immobile species from the dolostone source. This is a bit difficult to expect in a lateritic weathering environment in which all these elements except K would be expected to be immobile, unless special conditions have prevailed to mobilise some of them in solution. The other explanation would be that Mn would have to be added to the residual material to result in the composition of eastern belt ore. Metasomatic addition would also be required for practically every other trace element analysed, as all of them plot well above the immobility lines and therefore have to be added to the ores by fluids in order for their concentrations to be accounted for.

In the case of the isocon application for the western belt ore as recorded at the Bishop locality (Fig. 47), there is no complication with Al and HFSEs having to be removed from the carbonate protolith to produce the ore compositions, as this can be achieved by the wholesale loss of Ca, Mg and CO_2 alone. However, a group of minor and trace elements, such as Mo, Zn, Cr and Si, seem to have to be removed from the protolith to account for the ore chemistry. Most other elements plotted would still, however, require addition from an external source (fluids).

In summarizing, the isocon plots of Figures 47 and 48 suggest that chemically simple models of supergene loss of alkali earths and enrichments in Mn, Fe, Si and Al to produce the PMF ores, are not quite applicable. The ores evidently require complex metasomatic changes by fluids in order to result in compositons like those reported in this thesis. This is summarised further in the conclusive section that follows.

5.3 Conclusions

A first conclusion that applies across the whole range of manganese mineralisation examined in this thesis, is that there are no distinct geochemical differences observed during this study to support the classic separation found in the literature between western and eastern belt ores, especially based on major element oxides such as Si and Fe. Trace element distributions and REE also have no clear or robust diagnostic value to subdivide the Mn ores into clear subtypes. The Fe content can be very high in both eastern and western belt ores alike, whereas the high Si traditionally thought to characterise eastern belt ores, may be simply a function of the Si clasts contained in the ores, and not necessarily a reflection of the ore mineralogy itself. Further conclusions relating specifically to the eastern and western belt ores are discussed in the respective sections below.

5.3.1 Western Belt

The results of this study have provided some important new information concerning the genesis of the manganese deposits of the PMF. One of the most intriguing of these findings is the shale intercalations in laminated to massive western belt manganese ore. The presence of shale intercalations can be interpreted to reflect alternations between Mn-oxide rich sediment and barren clay-rich material in some kind of cycles, which have been preserved through the burial of these rock successions subsequently. What is most intriguing is the mineralogy and the chemistry of the shales, which are dominated by ephesite and therefore by excess Al and Na compared to Si. This kind of mineralogy and chemistry is not suggestive of simple weathering processes and transport of clay material into an aqueous environment of Mn oxide accumulation as suggested previously (Gutzmer and Beukes, 1996), unless that environment is not freshwater-dominated but possibly some form of hypersaline lake full of dissolved salts. Rather, it is more likely that the ores are hydrothermal replacement in origin at the expense of original shales – possibly the Mapedi/Gamagara shales – which upon reaction with Mn-rich alkali brines resulted in replacive formation of Fe- and Mn-rich mineralogy (braunite, hematite), leaching of Si from original shale material, and replacement of earlier phyllosilicate minerals (like sericite) by ephesite through removal of Si and addition of Na and Li from the brines.

It is further believed that the finer-scale correlation observed between aluminium oxide and manganese oxide as well as the antithetic relationship between aluminium oxide and iron oxide, are supportive of a replacement type style of ore deposition. Lateritic environments where Mn and Fe oxide deposition would take place, especially in the presence of free oxygen (*Beukes et al.,* 2002) would result in massive, unfractionated deposition of primary Fe and Mn oxides. However, fluid replacement mechanisms can preserve primary compositional variability in the rocks that are being replaced, and therefore can result in such apparent decoupling effects.

Therefore, the replacement model as initially proposed by Hall (1926) and Nel (1929), appears to receive some credence from the results presented in this thesis. In such a model, introduction of Mn and replacement of the country rock would have been carried out by manganiferous brines, the presence of which is supported by the elevated alkali content in the ores (abundant ephesite and lesser barite) in conjunction with the observation of halogen peaks in SEM spectra (such as F and Br). Further fluid interaction and alteration may have continued post ore-formation, as observed in the McCarthy and Leeuwfontein ore localities, with the former being subjected to much more oxidizing conditions of low-temperature fluid circulation, resulting in the breakdown of braunite and leaching out of Si and alkalis (except K) in producing what looks like typical supergene-type ore rich in cryptomelane. Further evidence for post ore-formation fluid alteration is suggested by the presence of cracked honeycomb textures in hematite-rich domains in Leeuwfontein ore, possibly associated with localised Ca addition and development of Ca mica and carbonates instead of sodic ephesite. Here, it is possible that the ores were originally Fe-rich and Si-poor with very little Mn, and the latter was added entirely through hyrothermal brines, resulting in localised associations within the ores of bixbyite with barite. The above information is all indicative of the complex history of these ores regionally, with more than one fluid events likely to have overprinted the ores from one locality to the next.

5.3.2 Eastern Belt and the possible pre-existence of evaporites

The existence of evaporites in a sedimentary sequence is often very difficult to decipher, as they easily dissolve thus leaving no evidence of their presence in the resultant lithology (Warren, 1999). Some of the most common evaporites in rocks are gypsum, anhydrite, and halite. Textures such as the crude laminations seen in the chert clast arrangement in the

Wolhaarkop breccia, have been inferred to represent previously interbedded evaporites within host rock (Warren, 1999), a possibility that appears to be rather plausible to the author. By contrast, the suggestion that such crude layering is the result of dissolution of chert-bearing carbonates (Gutzmer and Beukes, 1996; van Schalkwyk, 2005) seems rather improbable. To retain that sort of “ghost” layering in a carbonate host rock requires a much more soluble lithology than a dolostone and a far more dramatic process of *in situ* mass loss, given the very hard and resistant nature of chert interlayers. Evaporites however, because of their susceptibity to dissolution, are the most likely to be the first to get dissolved, thus leaving behind these crude laminations of insoluble material and resistant chert. Fragmented chert, detrital quartz, clay and dolomite rhombs or silicified dolostones (Jacobs *et al,* 1982; Warren, 1999), all recorded in the Wolhaarkop breccia, are common constituents of evaporite breccias. Silicified dolostones are also testament to the former existence of evaporites within the breccia units (Jacobs *et al,* 1982; Swennen *et al,* 1990).The vuggy and porous nature of the Wolhaarkop breccia as seen in the petrography section, also suggests dissolution of easily soluble materials, although one needs to be cautious of the possibility of further dissolution effects at more recent geological times post-dating early evaporite dissolution (such as seen in the Mn ore from locality McCarthy).

Mineralized brines rich in Mn and Fe – probably as chloride complexes – would thus have evolved from the underlying dolostones and later infiltrated the residual, highly permeable accumulations of solid material in sinkholes resulting in ore deposition. The presence of high alkali mineralogy as well as halogen signals again point to the brine source, similar (and possibly common) to the one responsible for the western belt deposits discussed earlier. Additionally, the PAAS-normalised chemical composition of the eastern belt deposits such as those at Khumani, suggests that the ore protolith was not dominantly BIF as argued for the immediately supradjacent massive hematite iron ores (Gutzmer and Beukes 2003; Smith and Beukes, 2015), but mainly of siliciclastic material. The clay intercalations that have been observed in the Wolhaarkop breccia have also been reported and described as hematite-rich illitic shales (Gutzmer, 1996).

This predominant shale-like signal was also observed by Moloto (2017) in his unpublished thesis on iron ore geochemistry, which presents an assessment of BIF-hosted hematitic iron ore at the Maremane Dome region. He concluded that shale fragments from the overlying Mapedi/Gamagara shales is a dominant detrital matter which got replaced by hematite during the ore forming process. It therefore becomes possible that regional-scale ore-forming mechanisms for Fe and Mn ores at the PMF, are characterised mainly by fluid-related replacement of siliciclastic as well as BIF detritus. It remains unclear though, what precisely controls the wide range of mineralisation in the PMF, from essentially pure hematite ores all the way to manganese-rich deposits containing little iron (as hematite).

5.4 Future Research

There is plenty of scope for a lot more research work to be done towards improving our understanding of the PMF deposits and their alkali associations. The possibility that the genesis of these deposits has involved a substantial fluid metasomatic contribution, means that the fluid-rock interaction history of these ores needs to be unravelled further. This can be done through standard stable isotope analyses of hydrous minerals for their oxygen and hydrogen isotope ratios, which may better constrain the source of these fluids and the temperature under which they operated upon reaction with the mineralised rocks. The presence of B, Li and halogens (such as Br and F) in these deposits also signifies specific brines which may have an identifiable origin through the application of analyses for bulk-rock contents and ratios of individual halogens (e.g. Cl/Br), and of course, stable isotope ratio analyses for the contained Li and B in the ores. Kolodny *et al* (2005), for example, have used boron isotopes in chert breccias and explored an association between boron and silicification in deep-sea sediments. Therefore, B and all other afore-mentioned chemical parameters may serve as diagnostic tools for the origin of the brines responsible for the alkali metasomatism of the ores and associated rocks, and ultimately for their role in ore-genesis of the PMF deposits.

6 References

Alchin, D., Lickfold, V., Mienie, P. J., Nel, D., & Strydom, M., 2008. An Integrated Exploration Approach to the Sishen South Iron Ore Deposit, Northern Cape Province, South Africa, and Its Implication for Developing a Structural and/or Resource Model for These Deposits. Reviews in Economic Geology 15, 317-338.

Angerer, T., Hagemann, S. G. and Danyushevsky, L. V., 2012. Geochemical evolution of the banded iron formation-hosted high-grade iron ore system in the Koolyanobbing Greenstone Belt, Western Australia. Econ. Geol., 107, 599– 644.

Astrup J and Tsikos H., 1998. Manganese. In: Wilson M.G.C. and Anhaeusser C.R. (Eds.), *The Mineral Resources of Southern Africa*. Handbook, Council for Geoscience, 16, 450-460.

Anbar, A.D., Duan,Y., Lyons, T.W., Arnold,G.L., Kendall, B., Creaser, R.A., Kaufman,A.J., Gordon, G.W., Scott, C., Garvin, J., and Buick, R., 2007. A Whiff of Oxygen before the Great Oxidation Event? *Science*, 317, 1903-1906.

Altermann W. and Siegfried H.P., 1997. Sedimentology and facies development of an Archaean shelf: carbonate platform transition in the Kaapvaal Craton, as deduced from a deep borehole at Kathu, South Africa. *Journal of African Earth Sciences* 24 (3), 391-410.

Bąbel M., and Schreiber B.C., 2014. Geochemistry of Evaporites and Evolution of Seawater. *Treatise on Geochemistry* 2, 483-559.

Bates R.L., and Jackson J.A., (Eds), 1987. Glossary of Geology. American geological institute, Alexandria, VA, 788.

Baumgartner, L. P., and Olsen, S. N., 1995, A least-squares approach to mass transport calculations using the isocon method: Economic Geology, v. 90, p. 1261-1270.

Beukes N.J., 1978. Facies relations, depositional environments and diagenesis in a major Early Proterozoic stromatolitic carbonate platform to basin sequence, Campbellrand Subgroup, Transvaal Supergroup, Southern Africa. *Sedimentary Geology* 54, 1-46.

Beukes, N. J. (1980). Stratigrafie en litofasies van die Campbellrand-Subgroep van die Proterofitiese Ghaap-Groep, Noord-Kaapland. Transactions of the Geological Society of South Africa 83, 141-170.

Beukes, N. J., 1983. Palaeoenvironmental setting of iron-formations in depositional basin of the Transvaal Supergroup, South Africa, in: Iron-formations: Facts and Problems, eds., A.F. Trendall and R.C. Morris. Developments in Precambrian Geology 6, 131-198.

Beukes N.J., 1986. The Transvaal Sequence in Griqualand West. In: Anhaeusser C.R. and Maske S. (Eds.), *Mineral Deposits of Southern Africa*. Geological Society of South Africa, Johannesburg.

Beukes N.J., 1987. Facies relations, depositional environments and diagenesis in a major early Proterozoic stromatolitic carbonate platform to basinal sequence, Campbellrand Subgroup, Transvaal Supergroup, Southern Africa, *Sedimentary Geology* 54, 1-46.

Beukes N.J. and Smit C.A.,1987. New evidence for thrust faulting in Griqualand West, South Africa: Implications for stratigraphy and the age of red beds. South African Journal of Geology 90 (4), 378-394.

Beukes, N.J., Dorland, H., Gutzmer, J., Nedachi, M., Ohmoto, H., 2002. Tropical laterites, life on land, and the history of atmospheric oxygen in the Paleoproterozoic. *Geology* 30, 491–494.

Blanckenhorn M., 1914. Arabien und Mesopotamien. *Handbuch derregionale Geologie* 5, 159.

Boardman L. G., 1964. Further geological data on the Postmasburg and Kuruman manganese ore deposits, Northern Cape Province. In: Haughton, S.H. (Ed.), The Geology of some ore deposits in Southern Africa, 2, Geol. Soc. S. Afr., Johannesburg 415-439.

Brockie D.C., Hare, E. H., Jr., and Dingess, P.R., 1968. The geology and ore deposits of the Tri-State District of Missouri, Kansas and Oklahoma. Ore Deposits of the United States 1933-1967.

Bryner L., 1961. Breccia and pebble columns associated with epigenetic ore deposits. Economic Geology 56, 488-508.

Button A., 1986. The Transvaal sub-basin of the Transvaal Sequence. In: Anhaeusser, C.R., Maske, S. (eds.) Mineral Deposits of Southern Africa. Geol. Soc. S. Afr., Johannesburg 811-817.

Cairncross, B., and Beukes, N.J. 2013. The Kalahari Manganese Filed – The Adventure Continues. Cape Town. Random House Struik.

Cheney E. S., 1996. Sequence stratigraphy and plate tectonic significance of the Transvaal succession of the Southern Africa and its equivalent in Western Australia. *Precambrian Research* 79, 3-24.

Cornell, D. H., Schutte, S. S., & Eglington, B. L., 1996. The Ongeluk basaltic andesite formation in Griqualand West, South Africa: Submarine alteration in 2222Ma Proterozoic sea. Precambrian Research 79, 101-124.

Costin, G. Fairey, B.J. Tsikos, H. Gucsik, A. 2015. Tokyoite, As-rich tokyoite and noelbensonite: new occurrences from the Postmasburg Manganese Field, Northern Cape Province, South Africa. The Canadian Mineralogist, 53, 981-990.

Cousins D.P., 2016. A stratigraphic, petrographic and geochemical study of the Gamagara Formation at the Maremane Dome, Northern Cape province, south Africa. *Thesis.* Rhodes University.

De Villiers J.E., 1944. The origin of the iron and manganese deposits in the Postmasburg and Thabazimbi areas. *Transactions of the Geological Society of South Africa* 47, 123-135.

De Villiers J.E., 1956. Manganese, Union of South Africa. Papers Int. Geolo. Congre. Mexico 2, 34-72.

De Villiers J.E., 1960. Manganese deposits of the Union of South Africa. *Geological Survey of South Africa*: Handbook 2, Government Printer, Pretoria.

Dixon R., 1985. A study of the compaction properties of potential clay—sand buffer mixtures for use in nuclear fuel waste disposal. Engineering Geology 21 (3-4), 247-255.

Dixon R., 1989. Sugilite and associated metamorphic silicate minerals from Wessels mine, Kalahari manganese field. Bulletin of the Geological Survey of South Africa, 93, 147.

Du Toit A.L., 1933. The manganese deposits of Postmasburg. South Africa. *Economic Geolog*y 28, 95-122.

Dunn, I.S., L.R. Anderson and F.W. Kiefer., 1980. Fundamentals of geotechnical analysis. John Wiley & Sons, Inc., New York.

Elderfield H., Hawkesworth C., Greaves M., and Calvert S., 1981. Rare earth element geochemistry of oceanic ferromanganese nodules and associated sediments. Geochim. Cosmochim. Acta 45, 513-528.

Eliassen A., and Talbot M. R., 2005. Solution-collapse breccias of the Minkinfjellet and Wordiekammen Formations, Central Spitsbergen, Svalbard: a large gypsum palaeokarst system. Sedimentology 52, 775-794.

Fairey B, Tsikos H, Corfu F, Polteau S., 2013. U-Pb systematics in carbonates of the Postmasburg Group Transvaal Supergroup, South Africa: primary versus metasomatic controls. Precambrian Res 231, 194-205.

Fairey, B.J., Timmerman, M.J., Sudo, M., and Tsikos, H., 2019. The Role of Hydrothermal Activity in the Formation of Karst-Hosted Manganese Deposits of the Postmasburg Mn Field, Northern Cape Province, South Africa. Minerals 9 (7), 408.

Fairbridge R.W., 1978. Breccia, sedimentary. The Encyclopedia of Sedimentology. Hutchison & Ross, Dowden, 84-86.

Friede, H. (1980). Iron age mining in the Transvaal. *J.S. Afr. Inst. Min. Metall* 80, 156-165.

Friedman G. M, 1997. Dissolution-collapse breccias and paleokarst resulting from dissolution of evaporite rocks, especially sulfates. Carbonates and Evaporites 12 (1), 53 -63.

Grant, J. A. (1986). The isocon diagram - a simple solution to Gresens equation or metasomatic alteration. *Economic Geology* 81, 1976 - 1982.

Grew E.S., 2015. Boron- The Crustal Element. *Elements* 11 (3), 162-163.

Grobbelaar, W.S., Beukes, N.J. (1986) The Bishop and Glosam Manganese Mines and the Beeshoek Iron Ore Mine of the Postmasburg area. In: Anhaeusser, C.R., Maske S. (eds.) Mineral deposits of Southern Africa. Geol. Soc. S. Afr., Johannesburg, 957–962.

Grobbelaar, W. S., Burger, M. A., Pretorius, A. I., Marais, W., & van Niekerk, I. J. (1995). Stratigraphic and structural setting of the Griqualand West and the Olifantshoek Sequences at Black Rock, Beeshoek and Rooinekke Mines, Griqualand West, South Africa. *Mineralium Deposita* 30, 152-161.

Gumsley, A.P., Chamberlain, K.R., Bleeker, W., Söderlund, U., de Kock, M.O., Larsson, E.R. and Bekker, A., 2017. Timing and tempo of the Great Oxidation Event. Proceedings of the National Academy of Sciences, 114(8), 1811-1816.

Gutzmer J. and Beukes N.J., 1995. Fault-controlled metasomatic alteration of Early Proterozoic sedimentary manganese ores in the Kalahari Manganese Field, South Africa. *Economic Geology* 90, 823-844.

Gutzmer J., 1996. Genesis and Alteration of the Kalahari and Postmasburg Manganese deposits, Griqualand West, South Africa. *Thesis.* University of Johannesburg.

Gutzmer J. and Beukes N.J., 1996. Karst-Hosted Fresh-Water Paleoproterozoic Manganese Deposits, Postmasburg, South Africa. *Economic Geology* 91, 1435-1454.

Gutzmer J. and Beukes N.J., 1997. Mineralogy and mineral chemistry of oxide-facies manganese ores of the Postmasburg manganese field, South Africa. *Mineralogical Magazine* 61, 213-231.

Gutzmer J. and Beukes N.J., 2003. Iron and Manganese Ore Deposits: Mineralogy, Geochemistry, and Economic Geology. Geology 4, 43-69.

Gutzmer, J., Chisonga, B.C., Beukes, N.J. and Mukhopadhyay, J. (2008). The Geochemistry of BIF-hosted High-Grade Hematite-Martite Iron Ores. *Reviews in Economic Geology*, v. 15, 157-184.

Hadley D. W., 1961. Alkali Reactivity of Carbonate Rocks – Expansion and Dedolomitization. *Highway Research Board Proc* 40, 462-474.

Hall A.L., 1926. The manganese deposits near Postmasburg, West of Kimberley. *Transactions of the Geological Society of South Africa* 29,17-46.

Harper G.D. and Tartarotti P., 1996. Structural Evolution of Upper Layer 2, Hole 896A. Alt, J.C., Kinoshita, H., Stokking, L.B., and Michael, P.J. (Eds.)., *Proceedings of the Ocean Drilling Program, Scientific Results* 148, 245-259.

Jacobs, L., Swennen, R., Van Orsmael, J., Notebaert, L. & Viaene, W., 1982. Occurrences of pseudomorphs after evaporite minerals in the Dinantian carbonate rocks of the eastern part of Belgium. Bull. Soc. Beige Geol., 91 (2): 105 — 123.

Jèbrak M., 1997. Hydrothermal breccias in vein-type ore deposits: a review of mechanisms, morphology and size distribution. Ore Geology Review 12, 111-134.

Kaiser E., 1931. Zur Frage der Entstehung der Manganerzlagerstätten von Postmasburg in Griqualand-West, Südafrika: *Neues. Jb. Min., Beil. Bd.* 64, Abt. A (Brauns-Festband).

Klein, 2005. Some Precambrian banded iron formations (BIFs) from around the world: Their age, geologic setting, mineralogy, metamorphism, geochemistry and origins. Am Mineral 90, 1473-1499.

Kolodny Y., Tarablous A., and Frieslander U., 1980. Participation of fresh water in chert diagenesis – Evidence from stable isotopes and boron α-track mapping. *Sedimentology* 27, 305-316.

Kolodny Y., Chaussidon M., and Katz A., 2005. Geochemistry of a chert breccia. *Geochimica et Cosmochimica* 69 (2), 427 – 439.

Laetsch, T., & Downs, R., 2006. Software For Identification and Refinement of Cell Parameters From Powder Diffraction Data of Minerals Using the RRUFF Project and American Mineralogist Crystal Structure Databases. Abstracts from the 19th General Meeting of the International Mineralogical Association, Kobe, Japan, 23-28 July 2006.

Land J. S., Tsikos H., Cousins D., Luvizotto G., and Zack T., 2018. Origin of red beds and paleosols in the Palaeoproterozoic Transvaal and Olifansthoek Supergroups of South Africa: provenance versus metasomatic controls. Geological Journal 53, 191–202.

Lawless J.V. and White P.J., 1990. Ore-related breccias: a revised genetic classification, with particular reference to epithermal deposits. New Zealand Geothermal Workshop 12, 197-202.

Laznicka P., 1988. Breccias and Coarse Fragmentites: Petrology, Environments, Associations, Ores. *Elsevier Science Ltd.*

Lee G. M., 1928. The Chert beds of Palestine. Proc. Geol. Ass. 39, 445-462.

Leisen, H. 1987. Geologisch-tektonische Kartierung der Griqualand West and Olifantshoek Sequenzen in der N/Srdlichen Kapprovinz, Siidafrika, auf der Grundlage yon Landsat-Mss-Daten und terrestrisch-photogrammetrischen Aufnahmen. Unpublished Ph.D.-thesis, Ludwig-Maximilian-University.

Locke A., 1926. The formation of certain ore bodies by mineralization stoping. Economic Geology 21, 431-453.

Madden R.H.C., Wilson, M. E.J., Mihaljevic, M., Pandolfi J.M. and Welsh K., 2017. Unravelling the depositional origins and diagenetic alteration of carbonate breccias. *Sedimentary Geology* 357, 33-52.

Macfarlane A.W. and Holland H.D., 1991, The timing of alkali metasomatism in paleosols: Can. *Mineral* 29, 1043-1050.

McLennan, S. M., Bock, B., Hemming, S. R., Hurowitz, J. A., Lev, S. M. and McDaniel, D. K. (2003). The roles of provenance and sedimentary processes in the geochemistry of sedimentary rocks, in Lentz, D.R., ed., Geochemistry of Sediments and Sedimentary Rocks: Evolutionary Considerations to Mineral Deposit-Forming Environments. *Geotext* 4, 7-38.

Middleton G.V., 1961. Evaporite solution breccias from the Mississippian of southwest Montana *Journal of Sedimentary Research* 31(2), 189 – 195.

Moloto W. 2017. A bulk and fraction-specific geochemical study of the origin of diverse high-grade hematitic iron ores from the Transvaal Supergroup, Northern Cape Province, South Africa. *Thesis*. Rhodes University.

Moore, J. M., Tsikos, H., & Polteau, S. 2001. Deconstructing the Transvaal Supergroup, South Africa: Implication for Palaeoproterozoic palaeoclimate models. *Journal of African Earth Sciences* 33, 437-444.

Moore J.M., Kuhn B.K., Mark D.F. and Tsikos H., 2011. A sugilite-bearing assemblage from the Wolhaarkop breccia, Bruce iron-ore min, South Africa: Evidence for alkali metasomatism and ^{40}Ar -^{39}Ar dating. *European Journal of Mineralogy* 23, 661-673.

Moore, J.M., Polteau, S., Armstrong, R.A., Corfu, F. and Tsikos, H., 2012. The age and correlation of the Postmasburg Group, southern Africa: Constraints from detrital zircon grains. *Journal of African Earth Sciences* 64 (2012), 9-19.

Nel L.T., 1929. The geology of the Postmasburg manganese deposits and the surrounding country. *Geological Survey of South Africa*, Special Publication.

Nelson, B. J., Wood, S. A., & Osiensky, J. L., 2003. Partitioning of REE between solution and particulate matter in natural waters: A filtration experiment. *Journal of Solid State Chemistry* 171, 51-56.

Norton W. H., 1917. Studies for students: a classification of breccias. *The Journal of Geology* 25(2), 160 – 194.

Pirajno F., 2009. Hydrothermal Processes and Wall Rock Alteration. In: Hydrothermal Processes and Mineral Systems. Springer, Dordrecht.

Plehwe-Leissen E. von and Klemm D.D., 1995. Geology and ore genesis of the manganese ore deposits of the Postmasburg manganese-field, South Africa. *Mineralium Deposita* 30, 257-267.

Plehwe-Leissen E. von., 1985. Geologische und erzpetrographische Untersuchungen der Manganerze des Postmasburgfeldes, Nördliche Kapprovinz, Südafrica. Unpublished PH.D. Thesis, Ludwig-Maximilians Universität, München, 129.

Picard L., 1931. Geological researches in the Judean desert, Jerusalem, Goldberg Press, 108.

Polteau S., Moore J.M. and Tsikos H., 2006. The geology and geochemistry of the Palaeoproterozoic Makganyene diamictite. *Precambrian Research* 148, 257-274.

Potter R. M., and Rossman G.R., 1979. The tetravalent manganese oxides: identification, hydration, and structural relationships by infrared spectroscopy. *American Mineralogist* 64, 1199-1218.

Rasmussen, B., Muhling, J.R., Zi J.W., Tsikos, H., and Fischer, W.W., 2020. A 1.25 Ga depositional age for the "Paleoproterozoic" Mapedi red beds, Kalahari manganese field, South Africa: New constraints on the timing of oxidative weathering and hematite mineralisation. *Geology* 48 (1), 44-48.

Reimold W. U., 1998. Exogenic and endogenic breccias: a discussion of major problematic. Earth Science Review 43, 25-47.

Richter R., and Richter E., 1933. Die letzten Phacopidae. *Bulletin du Musee Royal d'Histoire Naturelle de Belgique* 9(21), 1-19.

Robb L., 2005. Introduction to ore-forming processes. *Blackwell Science*.

Roy S., 2006. Sedimentary manganese metallogenesis in response to the evolution of the Earth systems. *Earth Science Reviews* 77, 273-305.

Sawkins F. J., 1964. Lead-zinc ore deposition in the light of fluid inclusion studies, Providencia Mine, Zacatecas, Mexico. *Economic Geology* 59, 883-919.

Sawkins F. J., 1969. Chemical Brecciation, an unrecognized mechanism for breccia formation? *Economic Geology* 64, 613-617.

Schalkwyk G.A.C., 2005. Genesis and characteristics of the Wolhaarkop breccia and associated Manganore iron formation. *MSc thesis.* University of Johannesburg.

Schneiderhöhn H., 1931. Mineralbestand und Gefüge der Manganerze von Postmasburg, Griqualand West, Südafrika: *Neus. Jb. Min., Beil. Bd.* 64, Abt. A (Brauns-Festband).

Sessions, A. L., Doughty, D. M., Welander, P. V., Summons R. E., and Newman, D. K., 2009. The continuing puzzle of the great oxidation event. *Current Biology* 19, 567-574.

Shukla M. K., and Sharma A., 2018. A brief review on breccia: it's contrasting origin and diagnostic signatures. *Solid Earth Sciences*, 1-10.

Smith, A.J.B., and Beukes, N.J., 2016. Palaeoproterozoic Banded Iron formation-hosted High-Grade Hematite Iron Ore Deposits of the Transvaal Supergroup, South Africa. *Episodes* 39 (2), 269-284.

Stanton R. L., 1978. Mineralisation in island arcs with particular reference to the SW pacific region. The Australian Institute of Mining and Metallurgy proceedings 268, 9-20.

Strauss C. A., 1964. The iron ore deposits in the Sishen area, Cape Province, in Haughton, S. H., (ed)., The geology of some ore deposits in Southern Africa, Johannesburg, Geological Society of South Africa 393-403.

Swennen R., Viaene W., and Cornelissen C., 1990. Petrography and geochemistry of the Belle Roche breccia (lower Visean, Belgium): evidence of brecciation by evaporite dissolution. Sedimentology 37, 859-878.

Taylor, S. R., & McLennan, S. M. , 1985. The continental crust: Its composition and evolution. *Oxford: Blackwell*.

Taylor R. G., 2009. Ore Textures. Recognition and Interpretation. *Berlin Springer.*

Terekhov E.N, and Shcherbakova T.F., 2006. Genesis of positive Eu anomalies in acid rocks from the Eastern Baltic Shield.

Tsikos, H., Moore, J. M., & Harris, C., 2001. Geochemistry of the Palaeoproterozoic Mooidraai Formation: Fe-rich limestone as end member of iron formation deposition, Kalahari Manganese Field, Transvaal Supergroup, South Africa. Journal of African Earth Sciences 32, 19-27.

Tsikos, H., Beukes, N. J., Moore, J. M., & Harris, C., 2003. Deposition, Diagenesis, and Secondary Enrichment of Metals in the Paleoproterozoic Hotazel Iron Formation, Kalahari Manganese Field, South Africa. Economic Geology 98, 1449-1462.

Tsikos, H., & Moore, J. M., 2005. Sodic metasomatism in the Palaeoproterozoic Hotazel iron-formation, Transvaal Supergroup, South Africa: implications for fluid-rock interaction in the Kalahari manganese field. *Geofluids* 5, 264-271.

Tsikos H., 1999. Petrographic and geochemical constraints on the origin and post-depositional history of the hotazel iron-manganese deposits, kalahari manganese field, South Africa. *Thesis*. Rhodes University.

Van Schalkwyk, and Beukes, N.J., 1986, The Sishen iron-ore deposit Griqualand West, in: Mineral deposits of Southern Africa, eds., Anhaeusser, C.R., and Maske, S. *Geol. Soc. S. Afr* 1, 931-956.

Van wyk J.F., and Beukes N.J., 1982. The geology of the Sishen iron ore deposit, in Glen, H.W., (ed)., Proceedings of the 12th CMMI Congress, Johannesburg, Geological Society of South Africa 203-211.

Velde B., 1971. The stability and natural occurrence of margarite. Mineralogical Magazine 38, 317-321.

Visser D. J. L., 1944. Stratigraphic features and tectonics of portions of Bechuanaland and Griqualand West. *South African Journal of Geology* 47 (1), 197-254.

Warren J. K., 2016. Evaporites. A Geological Compendium. Second edition. *Springer,* New York.

Wolf K. H., 1976. Handbook of strata-bound and stratiform ore deposits. *Elsevier Scientific Publishing Company*. Volume 5.

Yamaguchi, K. E., & Ohmoto, H. 2006. Geochemical and isotopic contraints on the origin of Paleoproterozoic red shales of the Gamagara/Mapedi Formation, Postmasburg Group, South Africa. South African Journal of Geology 109, 123-138.

Zhao, G., Sun, M., Wilde, S. A., and Sanzhong, L., 2005. Late Archean to Paleoproterozoic evolution of the North China Craton: Key issues revisited. *Precambrian Research* 136, 177-202.

Appendix A: Analytical techniques

The analytical techniques used in this study are described in greater detail in Appendix A. The techniques that will be discussed below include X-ray diffraction analysis, X-ray fluorescence analysis as well as electron microprobe analysis.

X-ray diffraction analysis

The average mineralogy was determined by means of XRD analyses performed using a Bruker D8 Discover XRD housed in the Department of Chemistry at Rhodes University. The machine is equipped with a Lynx Eye detector and uses a Cu-Kα radiation (= 1.5405 Å, nickel filter) operated with power at 20mA and 40kV. Approximately 1g of the crushed sample was prepared on a glass slide and inserted into the aluminium cavity mount. The scanning was completed from 5° to 55° (2θ) with speeds of 1° per minute. The X-ray diffraction data was treated using the Eva (evaluation curve fitting) software with baseline corrections performed on each diffraction pattern.

Qualitative phase identifications were completed via means of peak comparison to the database hosted by RRUF **(**Laetsch and Downs, 2006). The measured peaks on the diffraction patterns obtained are compared to known peaks of minerals from the database using the computer software, Crystal Sleuth (Laetsch and Downs, 2006). A collation of the spectra obtained obtained during this study is available in Appendix B.

X-ray fluorescence analysis

Samples were cleaned and pulverized at the Geology department at Rhodes University. The samples were then crushed in a chrome swing mill continuously for 2 minutes to ensure a homogenous fine talc-like powder. These were then sent off for major element and trace element analysis using XRF analysis at the Central of Analytical Facilities, Stellenbosch University, South Africa.

Glass disks were prepared for XRF analysis using 7.3 g of ultra-high purity trace element and Rare Earth Element-free flux ($LiBO_2$=49.75%, $Li_2B_4O_7$=49.75% LiI=0.50%) mixed with 0.4g of the pulverized sample. Whole-rock major element compositions were determined by XRF spectrometry on a PANalytical Axios Wavelength Dispersive spectrometer. The spectrometer is fitted with a Rhodium tube and with the following analytical crystals: LIF200, LIF220, PE002, GE111 and PX1. The instrument is fitted with a gas-flow proportional counter and a scintillation detector. The gas flow-flow proportional counter uses a 90% Ar to 10% methane gas mixture. Major element analysis was carried out using a fused glass disk, using a 2.4kW Rhodium tube. The matrix effects in the samples were corrected for by applying theoretical alpha factors and measured line overlap factors to the raw intensities measured with the SuperQ PANalytical software. The concentration of the control standards that were used in the calibration procedures for major element analysis, fit the range of concentration of the samples.

Electron microprobe analysis

Quantitative mineral chemical analyses were performed using a four wavelength dispersive spectrometer on a Jeol JXA 8230 electron probe micro-analyzer with 4 WD spectrometers housed in the Department of Geology, Rhodes University. The beam was generated by a Tungsten cathode; 15 kV accelerating potential, and 20 nA current. A 1µm beam size was applied; on beam sensitive phases up to 20µm was used.

The analyses were conducted on polished thin sections and briquettes with a 30 µm thick carbon coating. A variety of standard materials were used to set up the EMPA depending upon the mineral analysed.

Appendix B: Mineralogy

The XRD spectra and EMPA data will be grouped in term of the locality from which the samples were obtained. The numbers that go with the sample name essentially represent the depth at which the samples were obtained from the drill core. Leeuwfontein samples have essentially two numbers displayed in this format; X/Y and this is to distinguish between the two drill cores from which the samples were obtained. X represents the drill core number while Y is the depth of the sample.

Bishop and Leeuwfontein samples represent the Western belt of the Maremane Dome while the McCarthy and Khumani results are a reflection of the Eastern belt mineralogy.

Bishop

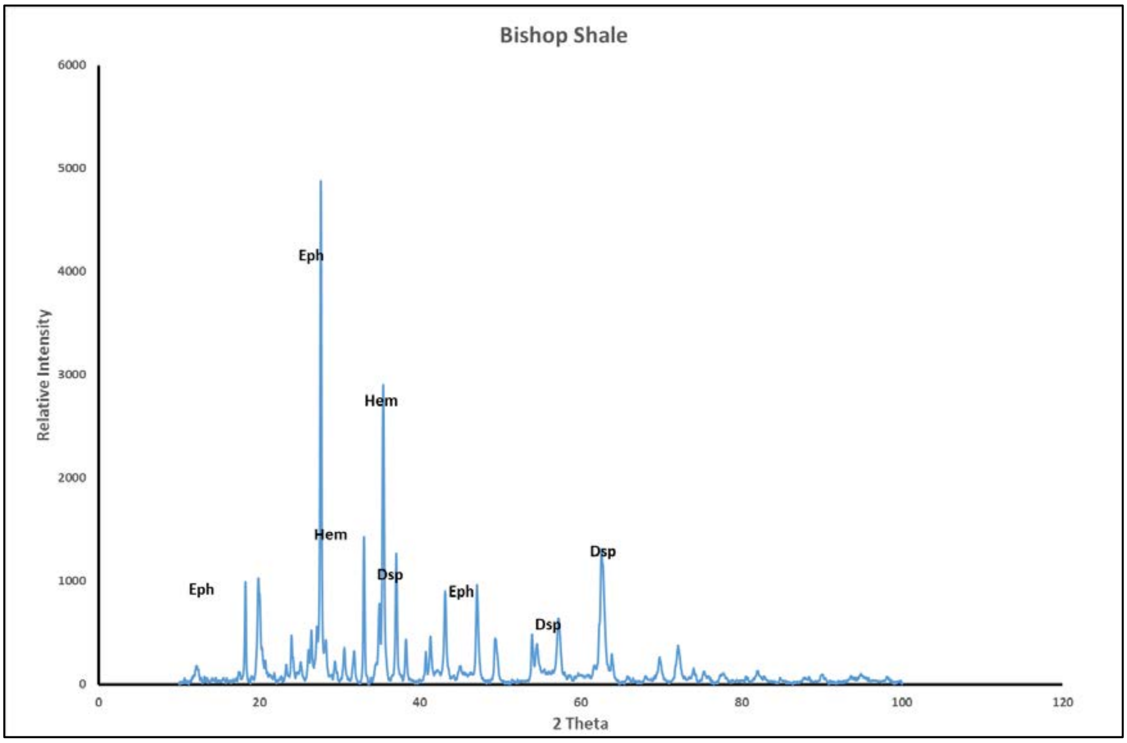

Figure B1: Representative XRD spectra of the red shale from the Bishop locality

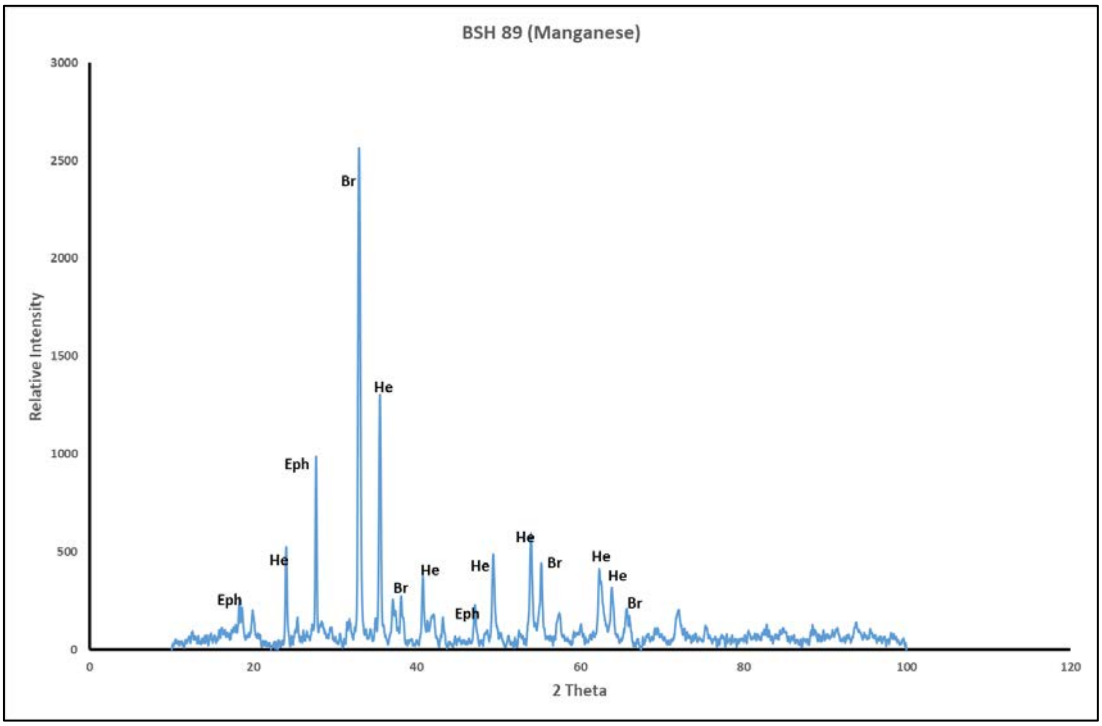

Figure B2: XRD spectra showing dominant mineral specis of the Bishop manganese ore.

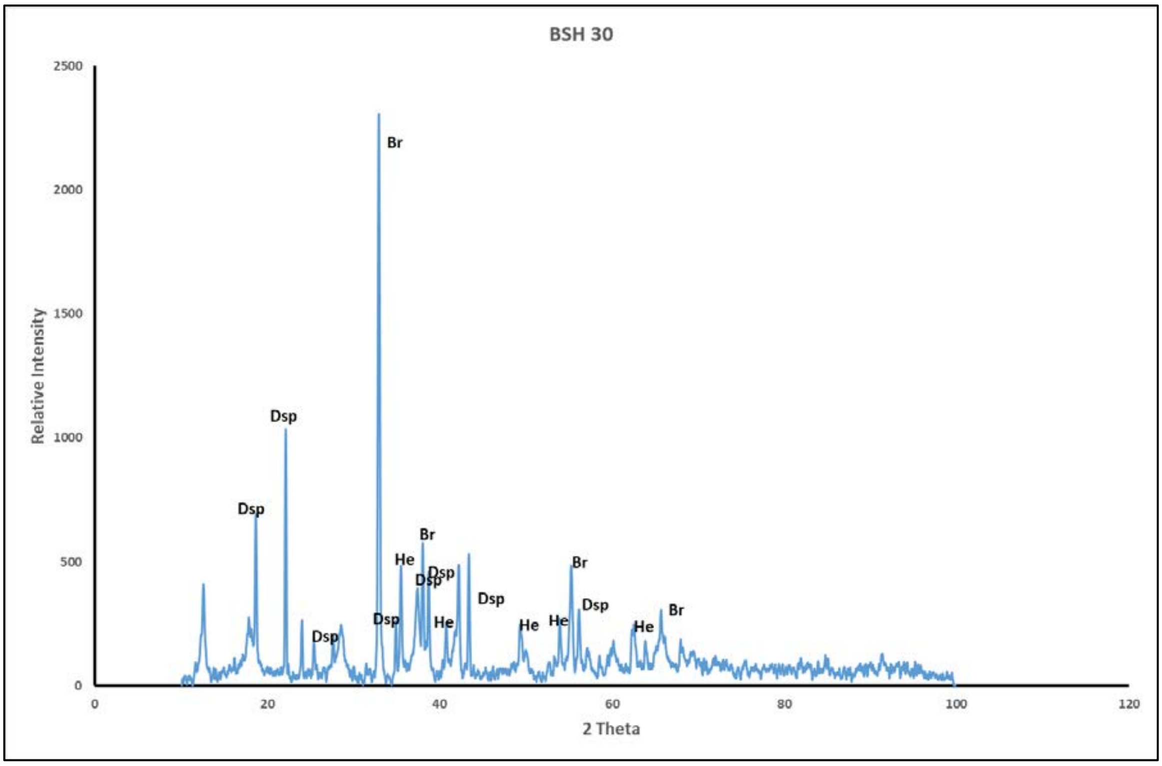

Figure B3: Dominant mineral species in the Bishop ore as refelcted by sample BSH 30

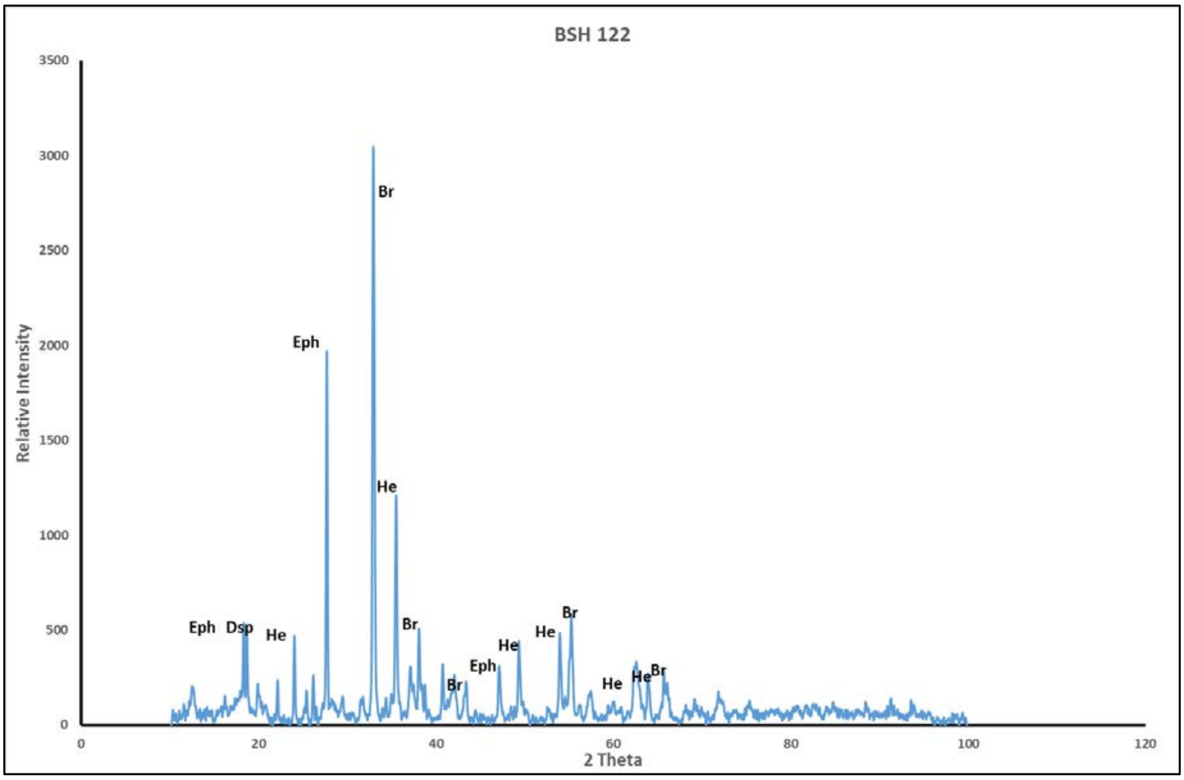

Figure B4: Dominant mineral species in the Bishop ore as refelcted by sample BSH 122

Leeuwfontein

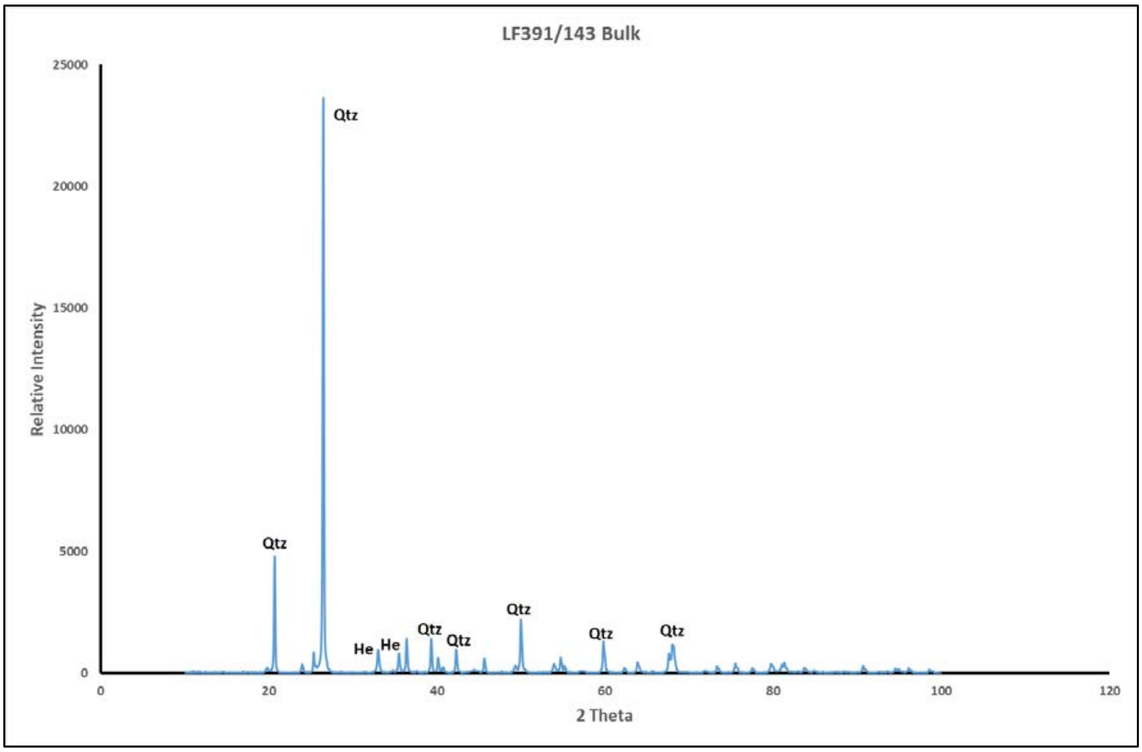

Figure B5: Dominant mineral species in the Leeuwfontein ore as refelcted by sample from drill core LF391, at a depth of 143m

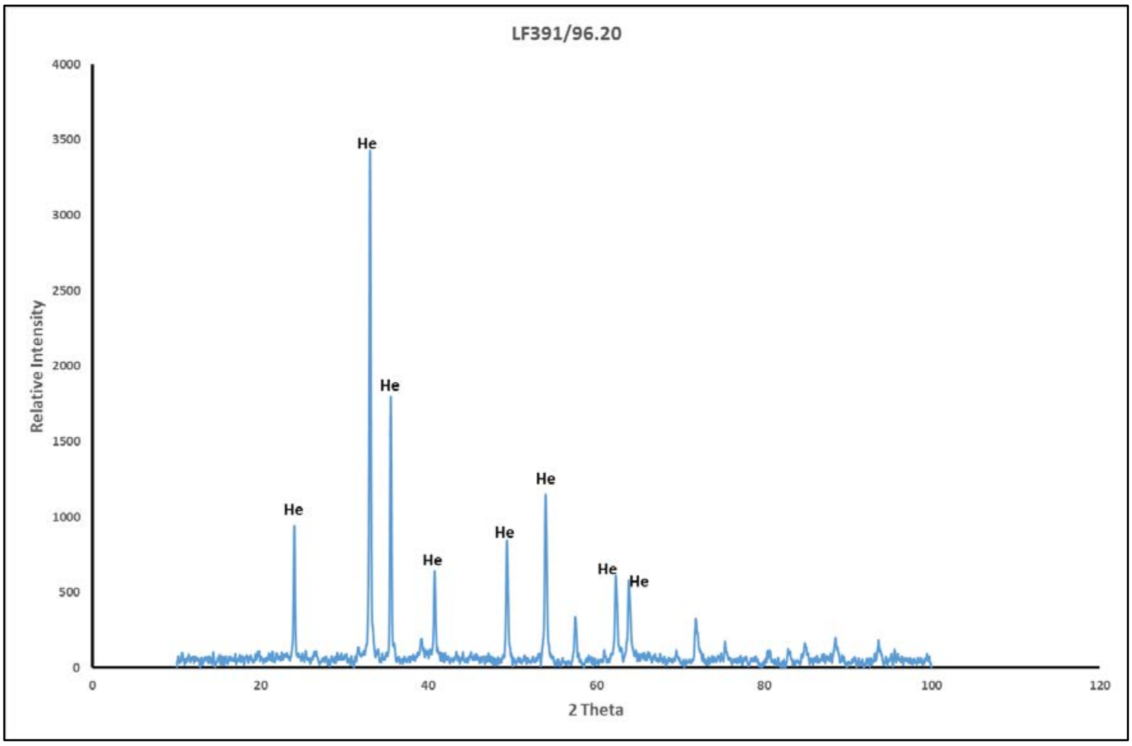

Figure B6: Dominant mineral species in the Leeuwfontein ore as refelcted by sample from drill core LF391, at a depth of 96.20m

Khumani

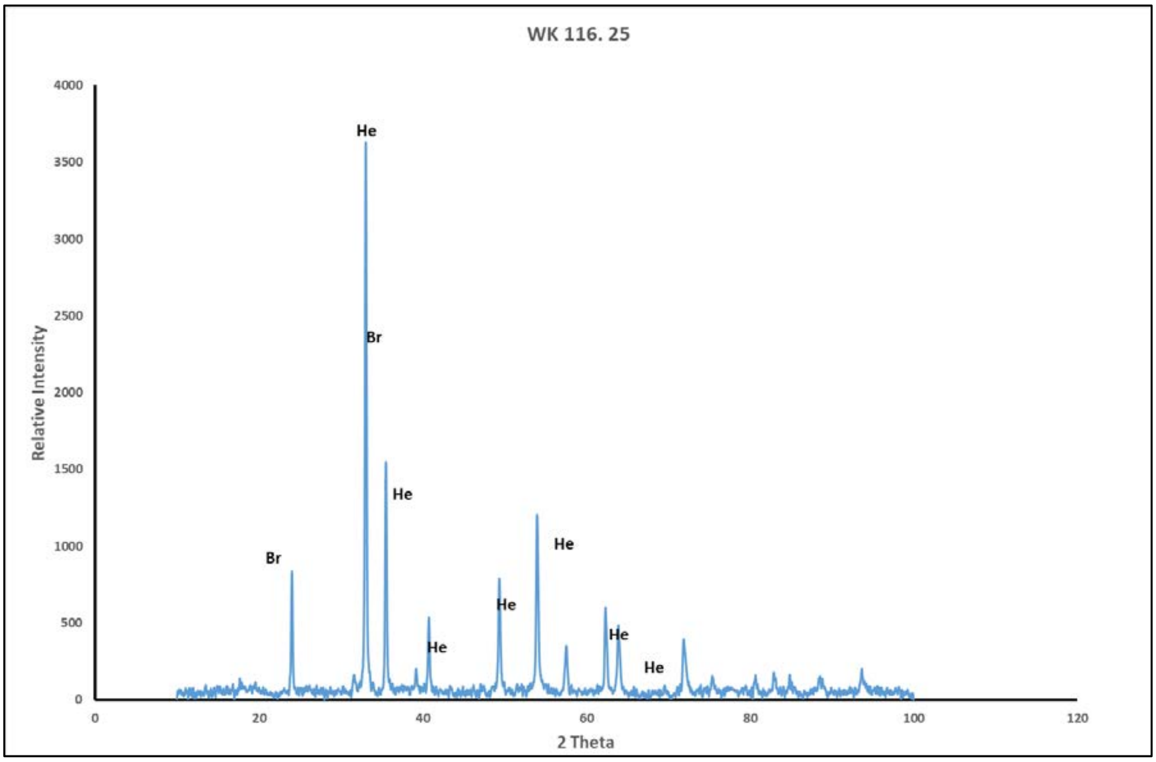

Figure B7: Dominant mineral species in the Khumani ore ,sample WK116.25

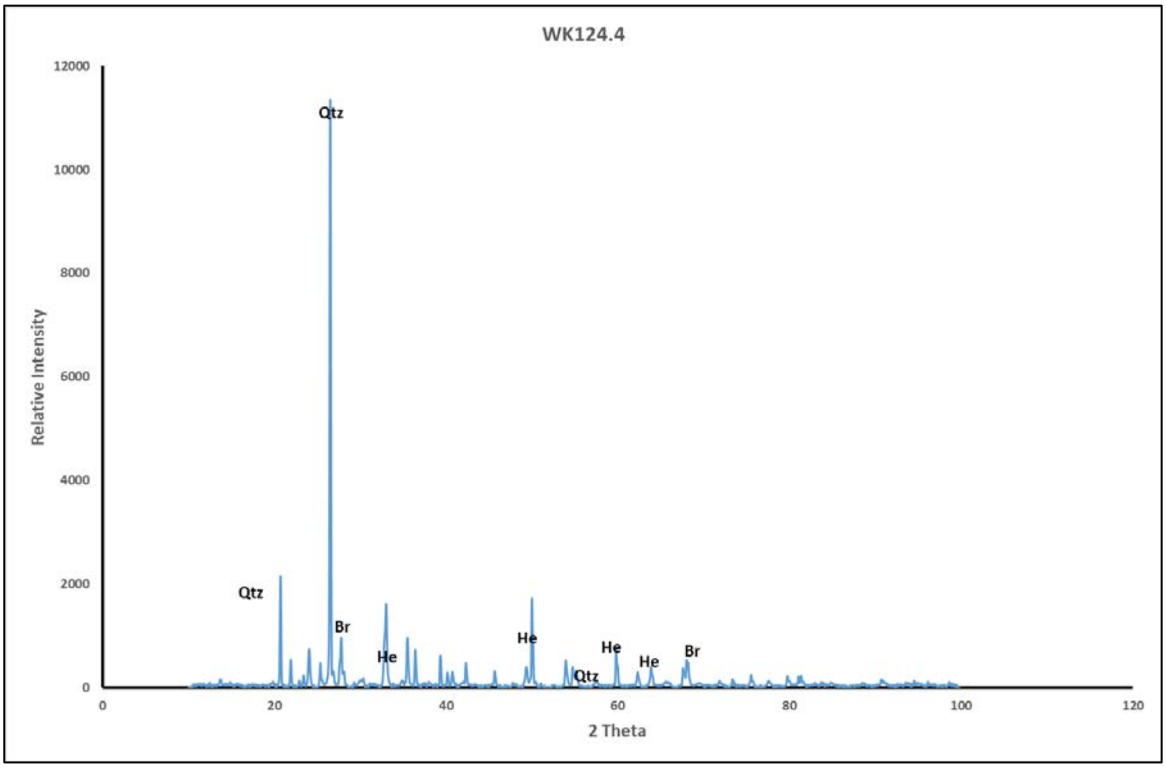

Figure B8: Dominant mineral species in the Khumani ore, sample WK124.4

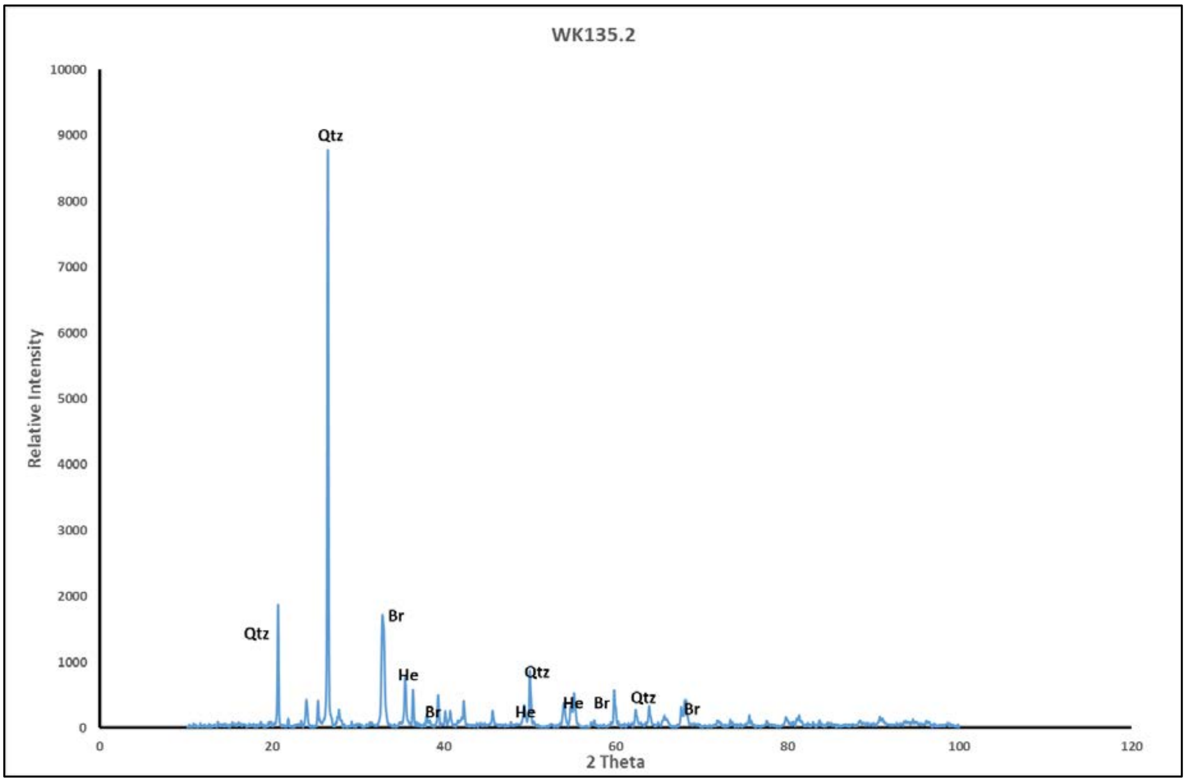

Figure B9: Dominant mineral species in the Khumani ore, sample WK135.2

McCarthy

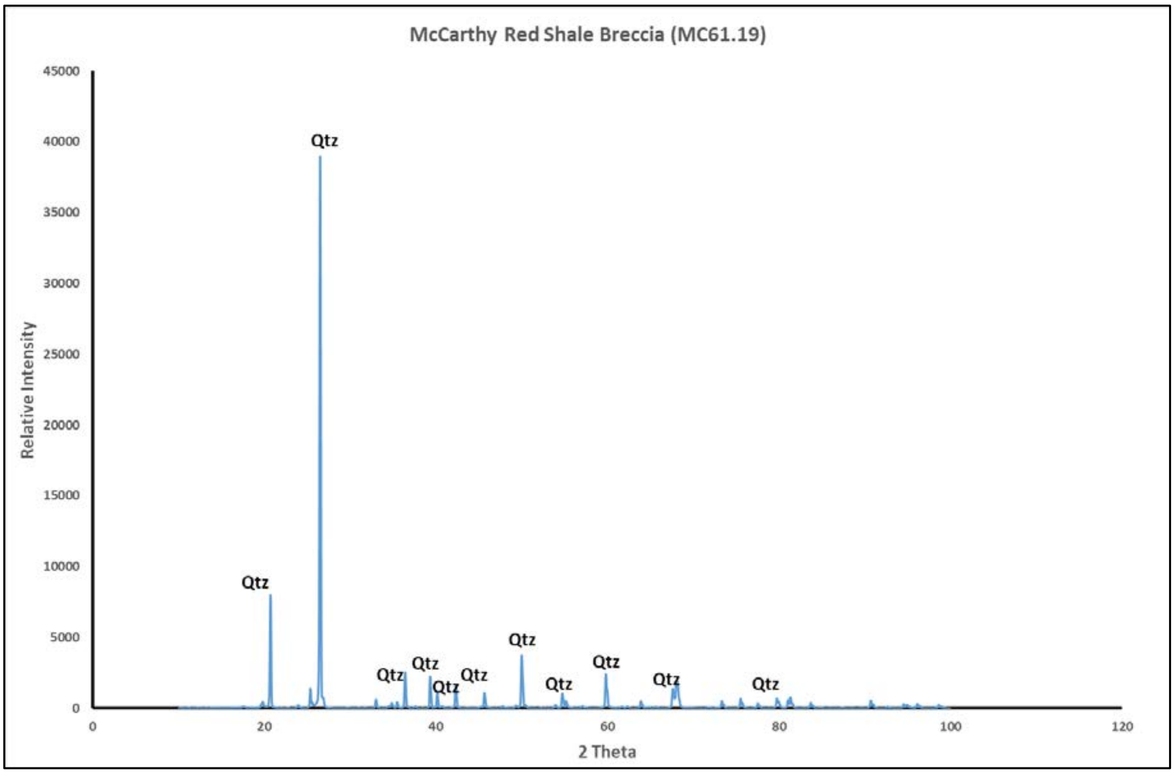

Figure B10: Dominant mineral species obtained from McCarthy farm, sample MC61.19

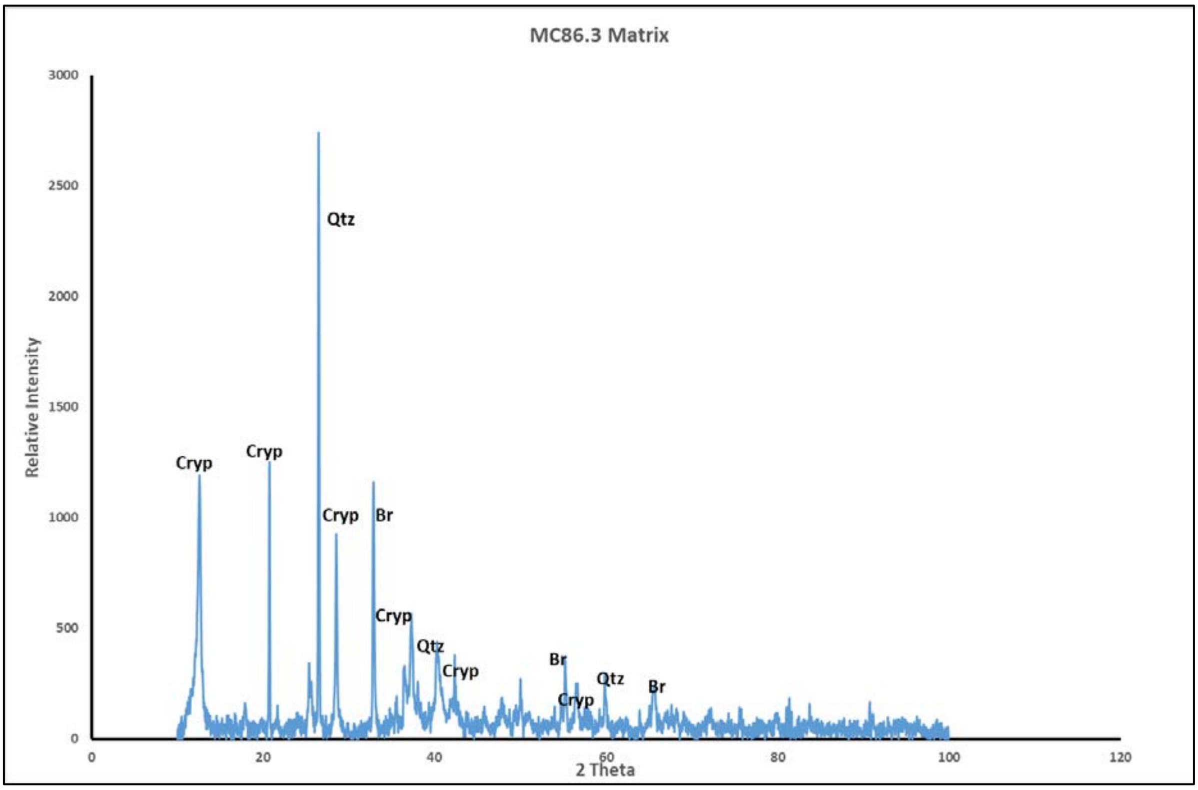

Figure B11: Dominant mineral species obtained from McCarthy farm, sample MC86.3

Probe Data

Bishop

Table B1: EMPA data for Hematite

Oxide	Analysis 1	Analysis 2	Analysis 3
SiO_2	0.611	1.674	5.372
Al_2O_3	0.475	1.096	4.364
MgO	0	0.105	0.227
P_2O_5	0.217	0.238	0.105
FeO	81.751	81.592	72.428
MnO	6.225	3.17	6.779
SO_3	0	0.007	0
CaO	0	0	0.032
BaO	0.837	0.167	0.902
Total	90.116	88.049	90.209

Table B2: EMPA data for Ephesite

Oxide	Analysis 1	Analysis 2
SiO_2	26.721	28.082
Al_2O_3	42.554	43.217
MgO	0.353	0.558
P_2O_5	0	0.069
FeO	14.792	3.675
MnO	0.568	1.188
SO_3	0.038	0.002
CaO	0.038	0.006
BaO	0.466	0.368
Total	85.53	77.135

Table B3: EMPA data for Braunite

Oxide	Analysis 1
SiO_2	8.097
Al_2O_3	0.855
MgO	0.138
P_2O_5	0.689
FeO	4.44
MnO	75.048
SO_3	0.007
CaO	0.5
BaO	0.431
Total	90.205

Khumani

Table B4: EMPA data for Barite

Oxide	Analysis 1
SiO_2	0
Al_2O_3	1.206
MgO	0
P_2O_5	0.218
FeO	0.012
MnO	0
SO_3	30.22
CaO	0.015
BaO	65.569
Total	97.24

Table B5: EMPA data for Quartz

Oxide	Analysis 1	Analysis 2	Analysis 3	Analysis 4
SiO_2	96.397	96.581	96.515	90.354
Al_2O_3	0	0	0	2.667
MgO	0	0.019	0.002	0.218
P_2O_5	0	0	0	0
FeO	0.084	0.031	0.342	0.29
MnO	0.061	0.016	0.013	0.029
SO_3	0.012	0	0	0.02
CaO	0	0	0.001	0
BaO	0	0	0	0.178
Total	96.554	96.647	96.873	93.756

Table B6: EMPA data for Braunite

Oxide	Analysis 1	Analysis 2	Analysis 3	Analysis 4
SiO_2	9.405	8.833	9.431	9.748
Al_2O_3	0.444	0.359	0.018	1.21
MgO	0.054	0.004	0.025	0.03
P_2O_5	0.351	0.375	0.273	0.712
FeO	6.517	6.51	0.097	4.007
MnO	71.156	72.005	79.043	73.18
SO_3	0.01	0.027	0	0.017
CaO	1.546	0.709	1.116	1.119
BaO	0.462	0.603	0	0.049
Total	89.945	89.425	90.003	90.072

Table B7: EMPA data for Hematite

Oxide	Analysis 1	Analysis 2	Analysis 3	Analysis 4
SiO_2	0.911	0.244	0.139	0.274
Al_2O_3	0.5	0.154	0.088	0.147
MgO	0.017	0.05	0	0.039
P_2O_5	0.105	0.186	0.224	0.271
FeO	86.469	85.307	88.41	88.275
MnO	3.763	2.733	2.938	2.068
SO_3	0	0.018	0.036	0.012
CaO	0.012	0.041	0	0.018
BaO	0.037	0.069	0	0
Total	91.814	88.802	91.835	91.104

McCarthy

Table B8: EMPA data for Quartz

Oxide	Analysis 1	Analysis 2
SiO_2	97.19	90.251
Al_2O_3	0	0.539
MgO	0	0.295
P_2O_5	0	0
FeO	0.007	0.412
MnO	0.19	2.773
SO_3	0.02	0.102
CaO	0	0.235
BaO	0.033	0
Total	97.44	94.607

Table B9: EMPA data for Cryptomelane

Oxide	Analysis 1	Analysis 2	Analysis 3	Analysis 4
SiO_2	0.677	0.714	0.947	0.875
Al_2O_3	0.401	0.374	0.417	0.439
MgO	3.36	1.828	2.362	0.726
P_2O_5	0.549	0.265	0.781	0.945
FeO	1.127	0.768	0.995	0.535
MnO	69.068	67.268	72.293	75.761
SO_3	0.016	0.049	0.046	0.066
CaO	0.781	0.692	0.84	0.842
BaO	0	0	0	0.007
Total	75.979	71.958	78.681	80.196

Table B10: EMPA data for Braunite

Oxide	Analysis 1	Analysis 2	Analysis 3	Analysis 4
SiO_2	3.943	9.991	9.712	9.401
Al_2O_3	0.557	0.826	0.786	0.787
MgO	0.64	0.03	0.035	0.076
P_2O_5	0.776	0.295	0.32	0.207
FeO	0.985	2.806	2.801	2.938
MnO	75.558	74.842	75.06	74.504
SO_3	0.033	0	0.023	0.018
CaO	0.882	1.215	1.507	1.572
BaO	0.077	0.049	0	0.009
Total	83.451	90.054	90.244	89.512

Leeuwfontein

Table B11: Aluminous hematite EMPA data

Oxide	Analysis 1
SiO_2	5.372
Al_2O_3	4.364
MgO	0.227
P_2O_5	0.105
FeO	72.428
MnO	6.779
SO_3	0
CaO	0.032
BaO	0.902
Total	90.209

Appendix C: Geochemistry

Appendix C contains raw tabulated whole-rock geochemical data for all samples analysed in this study. Major element data are expressed as values in weight percent (wt.%) whereas the trace element data are presented in parts per million (ppm).

This section also contains PAAS diagrams for individual samples from all the locations under study. In the thesis, some alterations had been done to the data in the form of averages and omissions of samples that show huge variability from the rest. Fluorine and Boron SEM/EDS data obtained during this study is also tabulated.

Whole-rock Geochemical Data

Abbreviations used:

LOI: Loss on ignition

bdl: below detection limit

Table C1: Bishop Major Elements

Sample	**Fe_2O_3 (wt%)**	**MnO_2 (wt%)**	**TiO_2 (wt%)**	**CaO (wt%)**	**K_2O (wt%)**	**P_2O_5 (wt%)**	**SiO_2 (wt%)**	**Al_2O_3 (wt%)**	**MgO (wt%)**	**Na_2O (wt%)**	**LOI (wt%)**	**Sum Of Conc. (wt%)**
BSH A	34.96	47.80	0.41	0.43	0.35	0.16	5.29	5.95	0.14	0.24	3.35	99.09
BSH B	37.42	44.71	0.36	0.48	0.38	0.16	5.40	6.66	0.13	0.37	3.02	99.09
BSH C	56.95	27.52	0.51	0.21	0.31	0.13	3.35	6.72	0.16	0.22	2.96	99.04
BSH D	28.04	52.48	0.45	0.53	0.45	0.22	5.86	7.39	0.27	0.27	3.23	99.19
BSH E	40.66	34.36	0.49	0.23	0.70	0.27	7.25	9.55	0.77	0.76	3.14	98.18
BSH 30	13.81	41.99	0.33	0.25	1.17	0.21	4.62	26.15	0.24	0.40	9.17	98.34
BSH 70	37.23	27.88	0.47	0.20	0.33	0.10	10.38	15.53	0.24	1.74	3.55	97.65
BSH 89	32.54	26.37	0.57	0.15	0.56	0.15	12.84	16.75	0.22	2.04	4.28	96.47
BSH 122	20.59	31.92	0.63	0.19	1.16	0.11	13.21	22.52	1.04	2.22	5.47	99.06
BSH 152	23.63	32.27	0.81	0.16	0.96	0.11	8.47	21.01	0.11	1.68	7.47	96.68

Sample	**Fe_2O_3 (wt%)**	**MnO_2 (wt%)**	**TiO_2 (wt%)**	**CaO (wt%)**	**K_2O (wt%)**	**P_2O_5 (wt%)**	**SiO_2 (wt%)**	**Al_2O_3 (wt%)**	**MgO (wt%)**	**Na_2O (wt%)**	**Cr_2O_3 (wt%)**	**L.O.I. (wt%)**	**Sum Of Conc. (wt%)**
BSH 80 Shale	12.71	0.25	0.17	0.08	0.73	0.02	58.45	87.57	0.15	11.23	0.08	6.84	178.27
BSH89 Shale	6.29	0.42	0.09	0.04	1.50	0.01	29.99	45.31	0.14	5.55	0.02	6.10	95.47

Table C2: Bishop Trace Elements and REEs

Sample	BSH A	BSH B	BSH C	BSH D	BSH E	BSH 30	BSH 70	BSH 89	BSH 122	BSH 152	BSH 80	BSH89
U	0.87	0.77	0.79	0.75	0.62	0.52	0.91	0.69	0.64	1.13	1.0905	0.714
Th	3.98	2.56	3.37	6.20	3.54	8.95	6.97	4.87	7.69	9.36	3.115	1.809
Pb	288.25	273.30	566.00	338.00	374.55	44.60	351.60	279.20	178.90	210.65	47.85	43.875
Ta	0.29	0.25	0.29	0.52	0.34	0.59	1.00	0.76	0.70	0.90	0.7595	0.425
Hf	1.47	1.04	1.10	2.97	1.27	2.01	5.98	4.19	2.82	5.30	0.5135	0.313
Lu	0.52	0.37	0.55	0.68	0.60	0.86	0.63	0.48	0.58	0.83	0.01395	0.025
Yb	3.41	2.64	3.69	4.48	4.05	5.59	4.29	3.35	3.77	5.76	0.0565	0.1695
Tm	0.62	0.41	0.62	0.70	0.65	0.80	0.71	0.51	0.55	0.90	0.018	0.0255
Er	4.67	3.56	4.86	5.76	4.80	6.05	5.60	4.37	4.73	6.52	0.103	0.15
Ho	1.73	1.28	1.94	2.08	1.77	2.04	2.01	1.61	1.58	2.35	0.0545	0.05
Dy	8.93	6.07	8.79	10.28	8.30	9.78	10.21	8.09	7.59	11.93	0.267	0.301
Tb	1.39	0.98	1.32	1.61	1.35	1.49	1.72	1.42	1.22	1.88	0.035	0.041
Gd	10.31	7.06	9.58	12.26	9.11	10.36	12.56	11.49	9.79	14.21	0.31	0.171
Eu	2.32	1.53	1.90	2.42	2.05	2.39	2.86	2.61	1.83	3.28	0.2485	0.2795
Sm	8.44	5.05	6.77	10.86	7.33	8.85	12.08	11.80	7.65	12.18	0.235	0.2115
Nd	37.65	26.30	28.30	69.00	38.20	42.65	64.70	75.45	36.95	60.00	1.735	1.47
Pr	8.51	5.79	6.25	16.61	9.32	10.83	16.44	18.49	9.48	14.56	0.5025	0.426
Ce	29.17	17.00	30.80	97.30	28.06	46.05	98.70	187.10	45.47	61.05	7.5	6.895
La	29.24	21.14	29.80	49.35	44.80	41.20	60.30	61.89	43.31	61.65	6.49	5.375
Ba	8220.00	4885.00	5450.00	5710.00	6705.00	4800.00	7790.00	8268.50	2235.00	11585.00	4866	6595.5
Cs	0.26	0.24	0.24	0.18	0.25	0.31	0.13	0.20	0.21	0.22	0.443	0.17
Mo	2.61	2.29	1.78	2.26	1.94	1.74	1.68	1.06	1.19	2.24	0.8	0.775
Nb	6.42	6.67	9.60	8.84	6.91	3.26	12.25	12.21	8.03	11.56	5.955	3.585
Zr	44.30	33.65	40.60	107.75	39.05	61.65	201.95	154.85	93.25	192.90	13.255	12.25
Y	56.45	45.08	65.00	78.25	61.20	68.35	68.95	61.27	54.25	73.45	1.855	1.61
Sr	107.20	153.90	122.75	166.10	201.00	473.50	261.90	138.45	343.40	519.00	915	342.3
Rb	2.72	2.81	2.83	3.61	8.52	7.41	3.30	7.00	9.39	6.95	7.945	13.47
Zn	54.50	54.30	60.80	58.95	64.60	130.60	76.45	53.95	89.45	127.25	85.75	32.65
Cu	129.70	124.90	85.75	206.65	82.50	107.50	121.65	80.50	92.00	147.60	182.05	22.45
Ni	167.20	84.55	137.20	192.50	223.70	209.00	82.75	58.10	156.70	197.95	36.6	23.85
Co	66.60	39.80	81.10	90.20	147.65	86.65	65.45	41.89	85.25	98.75	6.75	5.205
Cr	69.60	60.75	74.10	304.00	102.90	59.90	72.00	45.10	44.40	64.95	556.5	166.15
V	98.35	90.40	87.30	117.50	57.70	18.90	50.05	41.30	25.95	41.85	29.1	13.945
Sc	16.86	15.43	11.79	23.15	9.53	8.81	27.45	23.99	18.93	26.95	7.835	4.41

Table C3: Leeuwfontein Major Elements

Sample	Fe_2O_3 (wt%0)	MnO_2 (wt%)	TiO_2 (wt%)	CaO (wt%)	K_2O (wt%)	P_2O_5 (wt%)	SiO_2 (wt%)	Al_2O_3 (wt%)	MgO (wt%)	Na_2O (wt%)	LOI (wt%)	Sum Of Conc. (wt%)
LF391/ 118.4	54.49	12.72	0.60	5.82	0.03	0.11	15.23	7.69	0.13	0.08	2.90	99.80
LF391/ 135.20	25.92	51.62	0.04	3.22	bdl	0.08	14.50	0.99	0.48	0.04	2.56	99.43
LF391/ 134	54.97	31.58	0.32	1.86	bdl	0.12	5.46	4.01	0.42	0.03	0.95	99.71

Sample	Fe_2O_3 (wt%)	MnO_2 (wt%)	TiO_2 (wt%)	CaO (wt%)	K_2O (wt%)	P_2O_5 (wt%)	SiO_2 (wt%)	Al_2O_3 (wt%)	MgO (wt%)	Na_2O (wt%)	Cr_2O_3 (wt%)	L.O.I. (wt%)	Sum Of Conc. (wt%)
LF391/129.	37.74	28.19	0.10	2.02	0.02	0.03	21.01	1.48	0.35	0.01	bdl	2.73	93.68
LF391/96.20	93.01	0.02	0.10	0.24	0.29	0.13	2.69	2.38	bdl	0.03	bdl	1.11	100.00
LF391/132	41.37	24.99	0.07	4.38	0.04	0.01	16.65	4.00	0.47	0.04	bdl	2.91	94.92
LF391/107	52.40	23.78	0.02	1.36	0.24	0.01	12.31	2.58	0.17	0.25	bdl	2.36	95.47
LF393/143	7.73	0.19	0.02	1.26	0.02	0.01	84.47	0.31	0.01	0.02	bdl	0.78	94.81
LF393/119.8	23.82	1.13	0.60	24.39	0.01	0.07	24.74	19.79	0.14	0.35	bdl	3.24	98.27
LF393/111.5	42.89	6.17	1.17	12.62	0.01	0.33	12.54	13.83	3.02	0.01	bdl	5.66	98.24
LF393/126	48.12	0.63	0.71	6.16	0.80	0.10	18.62	18.73	0.23	1.59	bdl	3.35	99.03
LF393/134	57.24	24.50	0.03	1.25	0.00	0.05	5.33	4.52	0.11	0.03	bdl	1.39	94.45
LF391/151	70.24	0.07	0.02	0.07	0.04	0.02	29.38	0.43	0.03	0.04	bdl	0.40	#REF!
LF391 143.5	12.00	0.05	0.07	0.05	0.44	0.00	86.81	1.46	0.11	0.04	bdl	-0.06	100.98
LF393/130.9	75.64	13.14	0.03	0.75	0.01	0.04	3.01	2.05	0.05	0.02	bdl	1.51	99.13

Table C4: Leeuwfontein Trace Elements and REEs

Sample	LF391/	LF391/	LF391/	LF391/	LF393/	LF393/	LF393/	LF393/	Lf393/	LF391/	LF391/	LF391/	LF393/	LF391	LF391
U	2.31	0.433	3.3	2.1885	0.0625	5.785	1.631	1.6175	0.5445	0.9385	0.402	1.145	0.378	0.1965	0.2655
Th	1.218	1.206	0.7475	0.341	0.2025	20.73	35.355	12.89	0.234	10.175	0.4055	8.27	0.4105	1.51	0.3615
Pb	164.45	6.235	173.2	103.35	2.785	271.75	493.9	670	61.415	218.55	113.1	186.55	92.6	4.025	4.635
Ta	0.0775	0.2	0.049	0.0078	0.0239	4.29	2.0905	0.911	0.0166	0.6825	0.0229	1.1805	0.0224	0.0435	0.0106
Hf	0.3215	0.5385	0.202	0.106	0.103	12.825	9.075	4.77	0.077	2.42	0.1615	4.485	0.1415	0.2755	0.185
Lu	0.6725	0.0632	0.1905	0.7315	0.0265	0.8785	1.108	0.407	0.1935	0.443	1.0575	0.7415	0.1865	0.025	#DIV/0
Yb	4.31	0.4635	1.44	4.41	0.1345	6.595	7.43	2.445	1.265	2.635	6.86	4.65	1.15	0.161	0.069
Tm	0.7185	0.0701	0.2035	0.6965	0.0195	1.047	1.0745	0.369	0.1815	0.3365	1.1345	0.7195	0.2015	0.0285	0.0162
Er	5.685	0.4275	1.29	5.32	0.167	8.035	7.635	2.715	1.55	2.015	8.96	4.75	1.54	0.1365	0.171
Ho	1.85	0.139	0.4435	1.5545	0.05	2.6775	2.665	0.9625	0.5375	0.544	3.015	1.579	0.4315	0.065	#DIV/0
Dy	7.79	0.805	2.185	5.735	0.2675	13.41	14	4.82	2.34	2.395	12.81	7.36	2.195	0.232	0.231
Tb	1.0935	0.1085	0.338	0.7755	0.0405	1.9095	2.235	0.7695	0.355	0.3285	1.743	1.008	0.3495	#DIV/0	#DIV/0
Gd	6.015	0.725	2.18	5.575	0.274	11.325	16.93	6.105	2.45	2.32	9.75	6.665	2.11	0.285	0.285
Eu	0.894	0.221	0.5485	0.96	0.671	1.35	4.565	1.411	0.563	0.4835	1.39	1.365	0.3605	0.0695	0.079
Sm	2.09	0.612	2.025	3.7	0.166	5.79	24.315	5.715	1.99	1.935	3.57	5.77	1.61	0.1095	0.235
Nd	3.815	2.61	7.16	15.34	0.685	14.82	140.05	31.22	6.495	8.07	5.435	33.615	5.52	0.865	1.005
Pr	0.729	0.775	1.5275	3.515	0.1535	4.68	37.775	8.79	1.5285	2.195	0.9865	9.94	1.28	0.2075	0.204
Ce	8.75	11.715	7.825	11.13	10.725	1722.5	303.9	95.48	4.63	13.59	9.345	62.95	10.99	1.6	1.64
La	3.31	4.735	6.7	23.93	0.747	42.575	140.8	42.555	6.675	15.405	3.55	56.3	5.26	0.53	0.7135
Ba	136.4	1652	88.9	518.9	22085	307.85	160.55	1681	1960	336.05	123.05	267.55	369.5	1287	56.45
Cs	0.2875	0.266	0.554	1.267	0.0535	0.04	0.063	1.203	0.021	0.7355	0.1145	0.068	0.043	0.7265	0.295
Mo	2.575	2.67	2.525	2.1	4.265	7.23	7	2.895	1.84	2.685	2.305	2.65	1.87	4.39	4.26
Nb	0.96	2.945	0.6305	0.5095	1.9	271.8	43.245	12.28	0.392	6.12	0.55	17.145	0.508	1.325	0.3805
Zr	11.235	24.3	7.985	4.825	4.51	532.5	414	177.65	3.835	88.5	6.855	162.75	6.895	12.9	6.285
Y	126.25	4.455	11.56	125.65	3.54	94.09	94.7	38.09	23.805	18.655	127.35	72.8	22.245	2.985	1.825
Sr	21.205	42.6	30.27	32.57	549.15	307.85	34.665	2366.5	79.2	65.35	21.13	38.65	23.15	51.65	7.26
Rb	0.87	4.615	1.58	5.295	0.505	0.2675	0.2165	8.445	0.2	1.655	0.61	0.63	0.72	12.68	1.57
Zn	170	8.43	154.25	39.45	68.05	65.45	319.9	59	57	125.05	203.2	114.65	59.7	22.35	58.25
Cu	9	2.955	72.95	186.1	26.6	45.75	87.6	48.35	35.6	13.68	40.75	111.8	26.55	27.75	23.4
Ni	72.05	22.05	153.5	108.85	23.4	59.5	1194	97.2	56.85	210.25	68.3	564	56.85	32.45	24.1
Co	28.985	4.44	56.57	35.145	3.05	40.255	440.05	27.92	15.175	73.15	11.52	208.3	14.505	3.35	2.255
Cr	30.45	16.3	40.05	20.8	66.3	62.5	57.5	60.65	20.8	50.4	32.9	51.05	26.5	68.45	40.35
V	36.27	88.95	28.9	47.59	32.715	147.25	148.25	117.5	24.96	37.5	21.99	65.35	28.55	37.06	18.585
Sc	3.045	4.33	3.55	1.975	5.395	16.83	24.265	21.295	1.92	8.98	2.075	7.415	1.275	7.46	3.475

Table C5: Khumani Major Elements

Sample	Fe_2O_3 (wt%0)	MnO_2 (wt%)	TiO_2 (wt%)	CaO (wt%)	K_2O (wt%)	P_2O_5 (wt%)	SiO_2 (wt%)	Al_2O_3 (wt%)	MgO (wt%)	Na_2O (wt%)	LOI (wt%)	Sum Of Conc. (wt%)
WK124.4	53.71	6.46	0.21	0.66	1.17	0.05	32.61	3.42	0.21	0.59	1.03	100.12
WK135.2	18.98	13.06	0.14	0.63	0.54	0.06	61.12	2.89	0.29	0.87	0.57	99.15

Sample	Fe_2O_3 (wt%)	MnO_2 (wt%)	TiO_2 (wt%)	CaO (wt%)	K_2O (wt%)	P_2O_5 (wt%)	SiO_2 (wt%)	Al_2O_3 (wt%)	MgO (wt%)	Na_2O (wt%)	Cr_2O_3 (wt%)	L.O.I. (wt%)	Sum Of Conc. (wt%)
WK141.8	29.61	9.22	0.15	1.15	0.49	0.07	51.43	2.90	0.23	0.93	bdl	1.01	97.17
WK118.6	84.95	3.56	0.17	0.57	0.80	0.20	5.28	3.16	0.18	0.07	bdl	1.23	100.18
WK116.25	92.76	4.23	0.03	0.46	0.03	0.16	0.99	0.57	0.02	0.02	bdl	0.59	99.86
WK121.8	44.52	33.51	0.04	0.84	0.49	0.19	7.01	1.27	0.03	0.05	0.01	0.82	88.79
WK114.87	20.21	0.05	0.05	0.08	0.50	0.04	38.37	1.68	0.13	bdl	bdl	38.54	99.65

Table C6: Khumani Trace Elements and REEs

Sample	WK141.8	WK118.6	WK116.25	WK121.8	WK124.4	WK135.2	WK114.87
U	0.355	0.2715	0.0565	0.5195	0.5825	0.5815	0.1505
Th	1.9655	1.954	0.116	0.2825	3.66	2.47	0.4715
Pb	39.85	90	17.765	39.915	81.1	41.435	3.305
Ta	0.1145	0.137	0.0051	0.0161	0.1975	0.149	0.0163
Hf	0.5255	0.563	0.0305	0.0695	0.86	0.705	0.131
Lu	0.085	0.1305	0.01415	0.0272	0.2065	0.1035	0.039
Yb	0.655	0.885	0.1405	0.2445	1.485	0.725	0.3385
Tm	0.128	0.129	0.019	0.0465	0.218	0.122	0.039
Er	0.859	1.03	0.204	0.4145	1.64	0.715	0.302
Ho	0.335	0.3305	0.069	0.1565	0.6485	0.267	0.1185
Dy	1.53	1.74	0.291	0.845	2.95	1.44	0.694
Tb	0.2565	0.305	0.0442	0.149	0.4445	0.1765	0.109
Gd	1.56	2.095	0.3445	1.235	2.655	1.475	0.66
Eu	0.4195	0.693	0.131	0.634	0.736	0.3495	0.159
Sm	1.58	2.695	0.2815	1.435	2.38	1.29	1.1
Nd	8.095	15.85	1.11	5.555	8.035	7.12	12.735
Pr	2.075	3.78	0.2505	1.023	1.851	1.885	4.2
Ce	10.215	28.39	1.1485	4.17	20.435	28.64	32.235
La	7.81	11.91	0.955	2.18	5.375	7.825	20.18
Ba	929	3458.5	1545.5	9630	3195	1165.5	26.6
Cs	0.6855	2.385	0.3045	0.532	1.54	0.7105	0.3225
Mo	2.395	1.54	0.9	2.605	2.23	2.93	1.855
Nb	1.745	1.835	0.111	0.251	2.515	2.195	0.5195
Zr	21.915	20.77	1.19	5.09	29.03	29.29	5.7
Y	10.3	14.48	2.985	7.76	15.01	8.185	3.145
Sr	74.35	56.2	30.05	46.125	53.6	68.75	5.795
Rb	10.655	15.995	0.5005	6.875	22.195	14.995	12.26
Zn	21.35	20.9	7.675	36.1	26.9	18.05	6.63
Cu	31.7	25.625	7.17	275.7	35.8	45.95	9.86
Ni	44.15	84.2	38.45	72.1	69.05	45.65	18.8
Co	17.5	36.68	15.105	60.05	31.135	19.425	2.955
Cr	56.75	62.25	11.905	86.2	78.85	66.85	34.05
V	31.905	23.71	10.245	47.14	24.77	31.01	17.2
Sc	6.52	3.725	0.62	1.515	8.22	8.065	5.175

Table C7: McCarthy Major Elements

Sample	Fe_2O_3 (wt% 0)	MnO_2 (wt%)	TiO_2 (wt%)	CaO (wt%)	K_2O (wt%)	P_2O_5 (wt%)	SiO_2 (wt%)	Al_2O_3 (wt%)	MgO (wt%)	Na_2O (wt%)	LOI (wt%)	Sum Of Conc. (wt%)
MC86.3 BULK	6.23	23.67	0.06	0.38	0.37	0.04	52.75	1.29	1.16	0.06	13.09	99.1
MC83 BULK	3.71	9.21	0.03	0.24	0.26	0.04	83.64	0.66	0.25	0	1.99	100.03

Sample	Fe_2O_3 (wt %)	MnO_2 (wt %)	TiO_2 (wt %)	CaO (wt %)	K_2O (wt %)	P_2O_5 (wt %)	SiO_2 (wt %)	Al_2O_3 (wt %)	MgO (wt %)	Na_2O (wt %)	Cr_2O_3 (wt %)	L.O.I. (wt%)	Sum Of Conc. (wt%)
MC50.62	10.25	0.09	0.35	0.13	1.91	0.04	79.64	6.57	0.23	0.01	bdl	1.36	100.58
MC61.19	12.93	0.09	0.06	0.05	0.38	0.02	84.40	1.42	0.01	0.02	bdl	0.68	100.08
MC33.50	59.88	0.03	0.07	0.06	0.22	0.06	38.28	1.23	0.00	0.02	bdl	0.36	100.22

Table C8: McCarthy Trace Elements And REEs

Values in	MC50.62	MC61.19	MC86.3	MC83	MC33.50
U	0.47	0.12	0.57	0.30	0.26
Th	5.81	1.13	0.71	0.34	0.98
Pb	3.07	1.26	6.40	3.13	20.72
Ta	0.40	0.04	0.04	0.04	0.06
Hf	2.27	0.34	0.19	0.13	0.73
Lu	0.19	0.06	0.12	0.12	0.05
Yb	1.17	0.35	0.67	0.76	0.45
Tm	0.18	0.08	0.12	0.12	0.05
Er	1.09	0.55	1.09	1.32	0.41
Ho	0.30	0.17	0.37	0.37	0.12
Dy	1.33	1.00	1.38	1.39	0.57
Tb	0.24	0.17	0.14	0.17	0.08
Gd	1.69	1.09	1.50	1.39	0.62
Eu	0.49	0.17	0.35	0.29	0.16
Sm	3.12	0.54	0.84	0.91	0.58
Nd	14.84	0.77	3.42	6.80	3.37
Pr	3.93	0.13	0.83	1.70	0.92
Ce	33.01	1.42	2.45	6.70	9.47
La	21.95	0.49	2.54	10.96	4.22
Ba	69.05	27.75	4841.50	1373.00	295.93
Cs	0.88	0.22	2.14	0.56	0.18
Mo	2.35	4.19	2.86	4.04	1.82
Nb	4.98	0.93	0.64	0.41	1.07
Zr	88.35	10.65	8.54	5.87	28.12
Y	8.47	4.14	27.93	25.17	3.88
Sr	21.99	4.46	359.50	190.55	77.85
Rb	35.60	7.49	10.71	4.50	3.37
Zn	9.20	8.70	27.20	31.80	19.60
Cu	12.15	21.60	25.50	27.20	9.94
Ni	98.60	65.25	54.85	49.60	27.55
Co	9.13	4.70	8.79	5.75	1.39
Cr	55.25	66.00	52.65	52.85	50.75
V	27.81	30.65	23.97	30.38	27.80
Sc	12.40	7.95	4.96	6.52	4.78

Table C9: Western and Eastern Belt carbonate major elements

Sample	Fe_2O_3 (wt%)	MnO (wt%)	TiO_2 (wt%)	CaO (wt%)	K_2O (wt%)	P_2O_5 (wt%)	SiO_2 (wt%)	Al_2O_3 (wt%)	MgO (wt%)	Na_2O (wt%)	Cr_2O_3 (wt%)	L.O.I. (wt%)	Sum Of Conc. (wt%)
BSH CARB	0.83	1.09	0.01	31.24	0.03	0.01	1.26	0.28	20.49	bdl	bdl	43.84	99.07
MC06/76.14	0.68	1.49	0.01	31.95	0.02	0.03	0.25	0.21	20.42	bdl	bdl	44.13	99.19

Table C10: Western and Eastern Belt carbonate minor elements

Sample	**BSH CARB**	**MC06/76.14**
U	0.1005	0.0335
Th	0.0475	0.0465
Pb	2.125	3.7
Ta	bdl	bdl
Hf	bdl	bdl
Lu	bdl	bdl
Yb	0.235	0.0435
Tm	bdl	bdl
Er	0.1565	bdl
Ho	0.115	0.021
Dy	0.25	bdl
Tb	0.0235	bdl
Gd	bdl	bdl
Eu	bdl	bdl
Sm	0.4	bdl
Nd	1.3725	0.395
Pr	0.263	0.074
Ce	1.685	0.625
La	0.92	0.434
Ba	11.8	6.6
Cs	bdl	bdl
Mo	0.585	0.395
Nb	0.21	0.194
Zr	3.55	2.59
Y	2.75	0.765
Sr	15.2	9.1
Rb	0.86	0.45
Zn	22.75	6.615
Cu	9.05	8.9
Ni	7.35	7
Co	1.205	0.62
Cr	36	7.2
V	3.525	2.59
Sc	0.725	0.41

PAAS Trace Element Graphs

Bishop

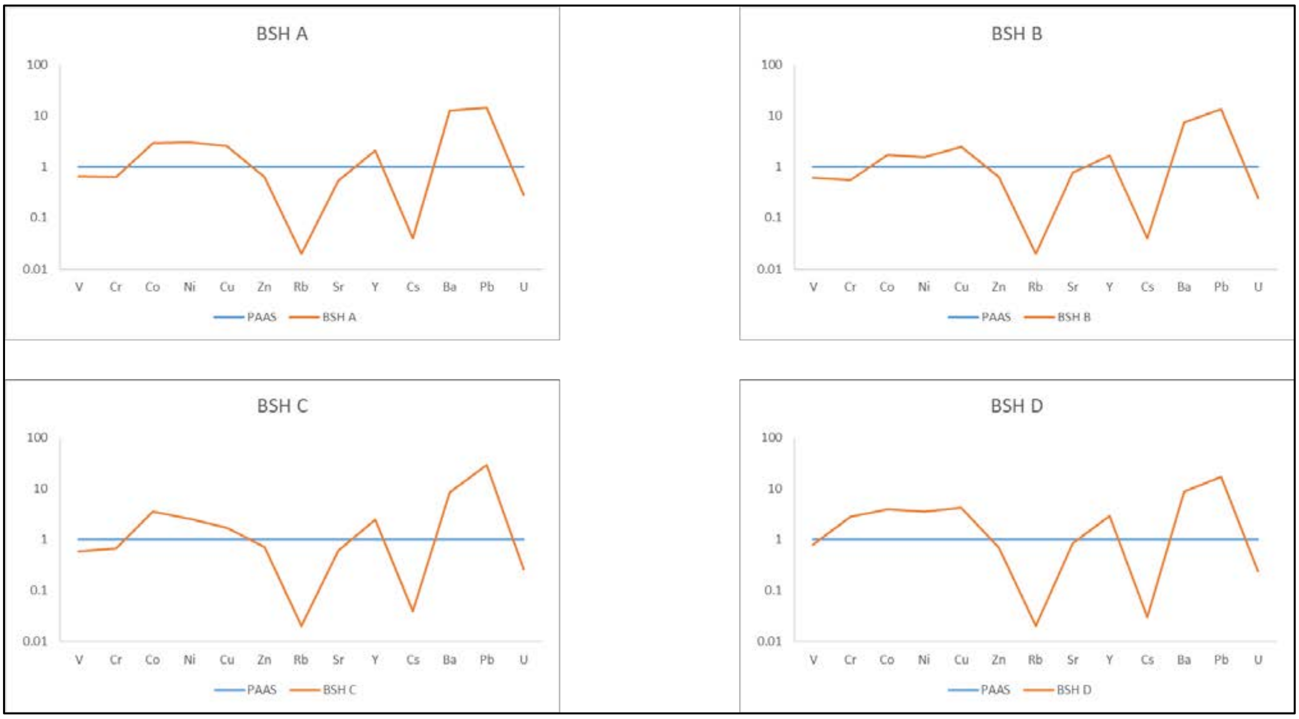

Figure C1: Ore trace element from the Bishop locality plotted against PAAS

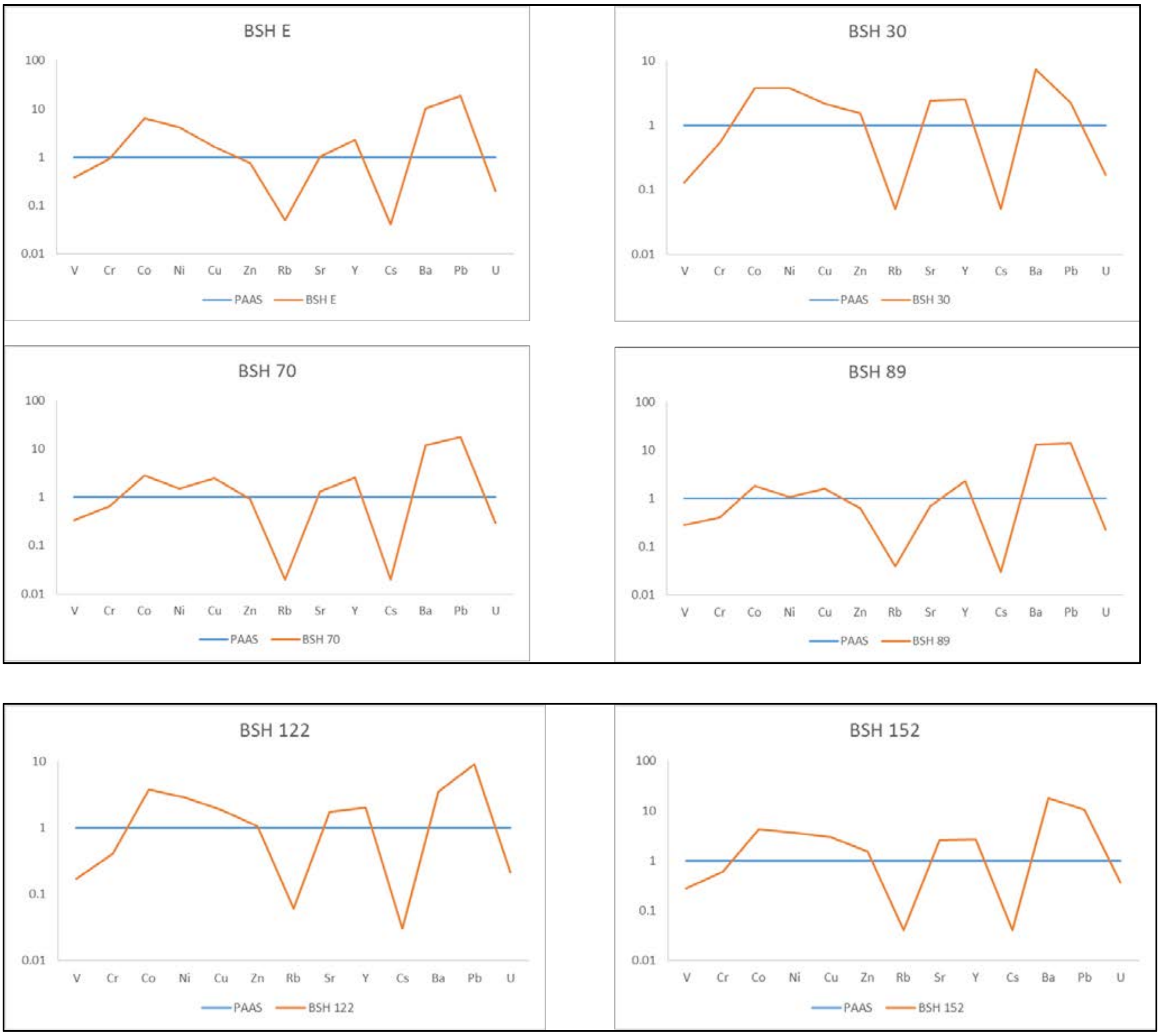

Figure C2: More ore trace elements from the Bishop locality plotted against PAAS

Leeuwfontein

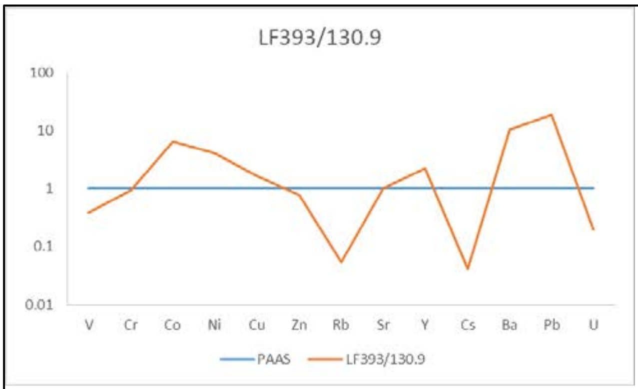

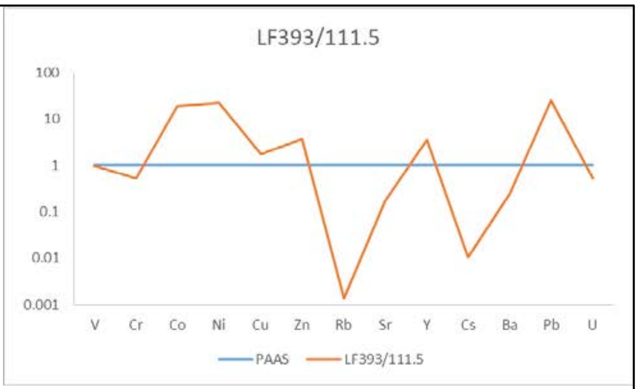

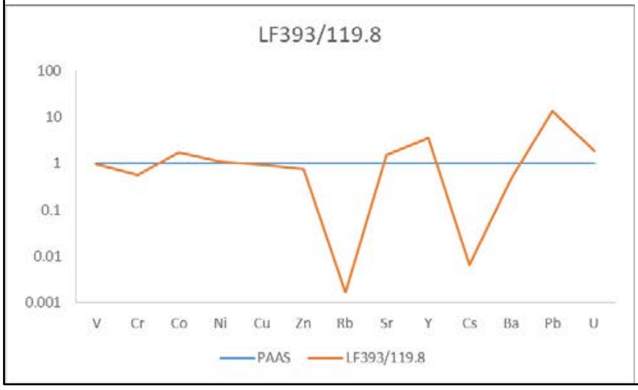

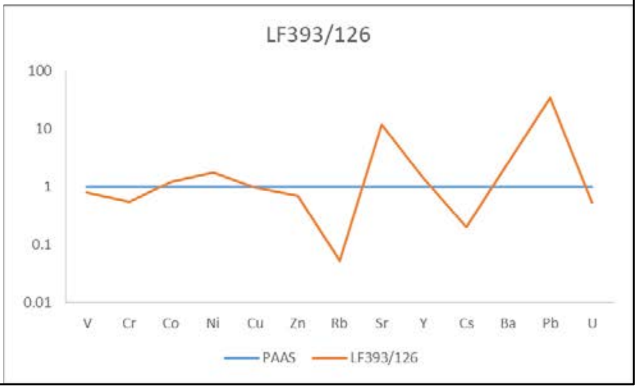

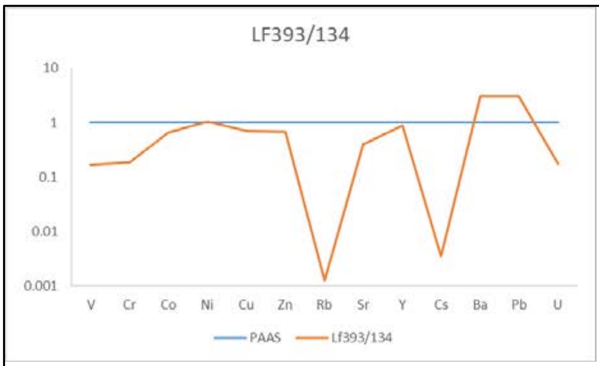

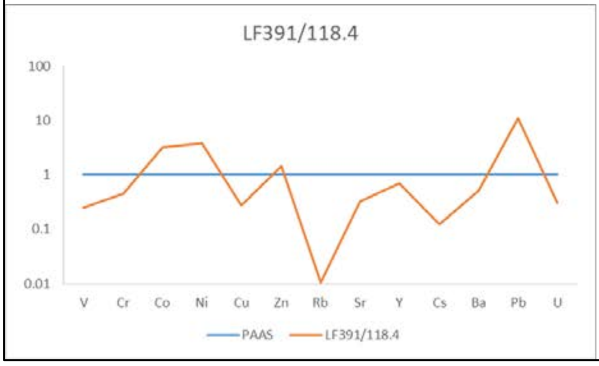

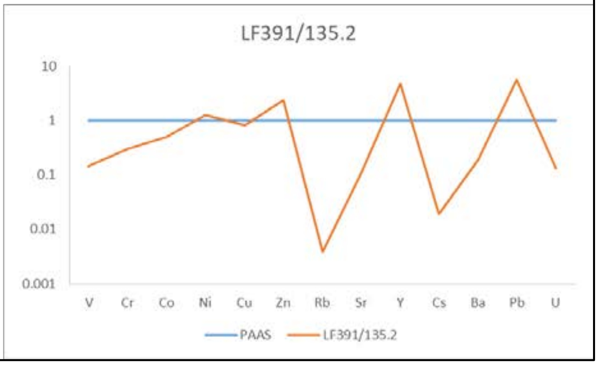

Figure C3: Ore trace elements from the Leeuwfontein locality plotted against PAAS

Khumani

Figure C4: Ore trace elements from the Khumani locality plotted against PAAS

McCarthy

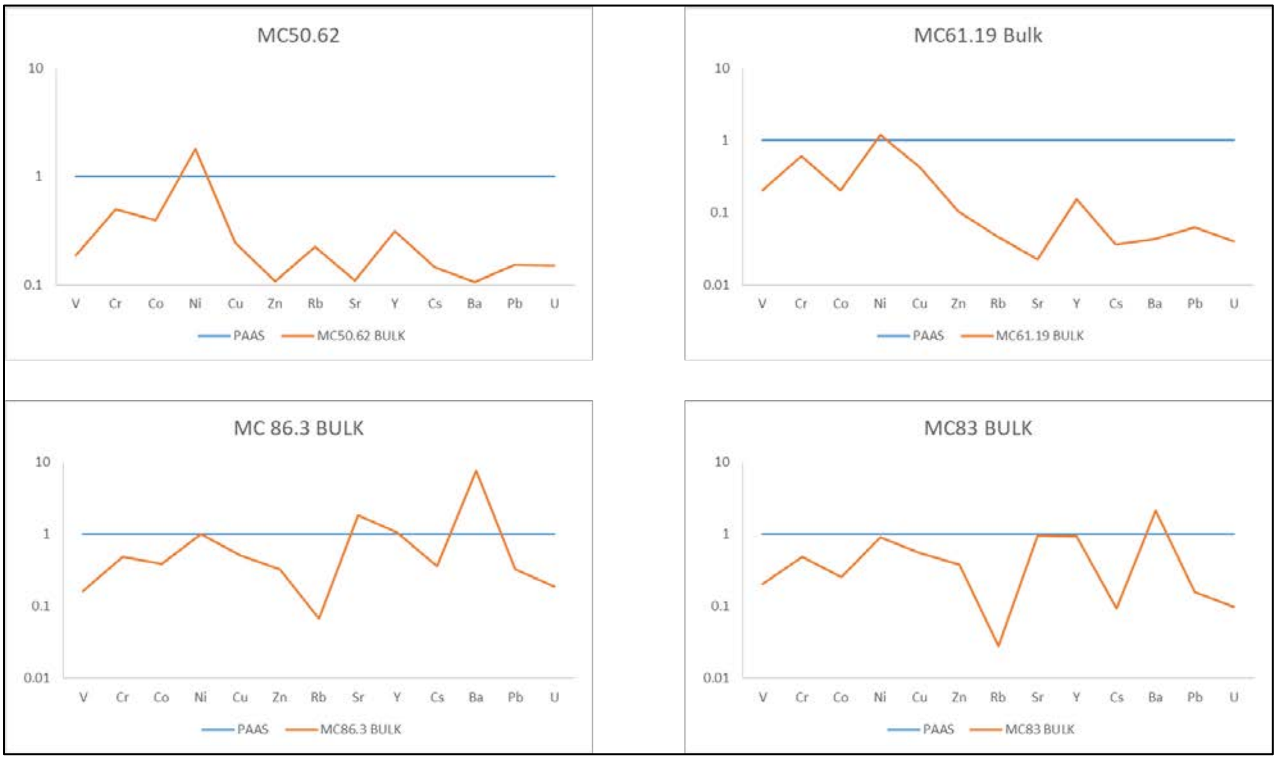

Figure C5: Ore trace elements from McCarthy farm plotted against PAAS

Rare Earth Element PAAS Graphs

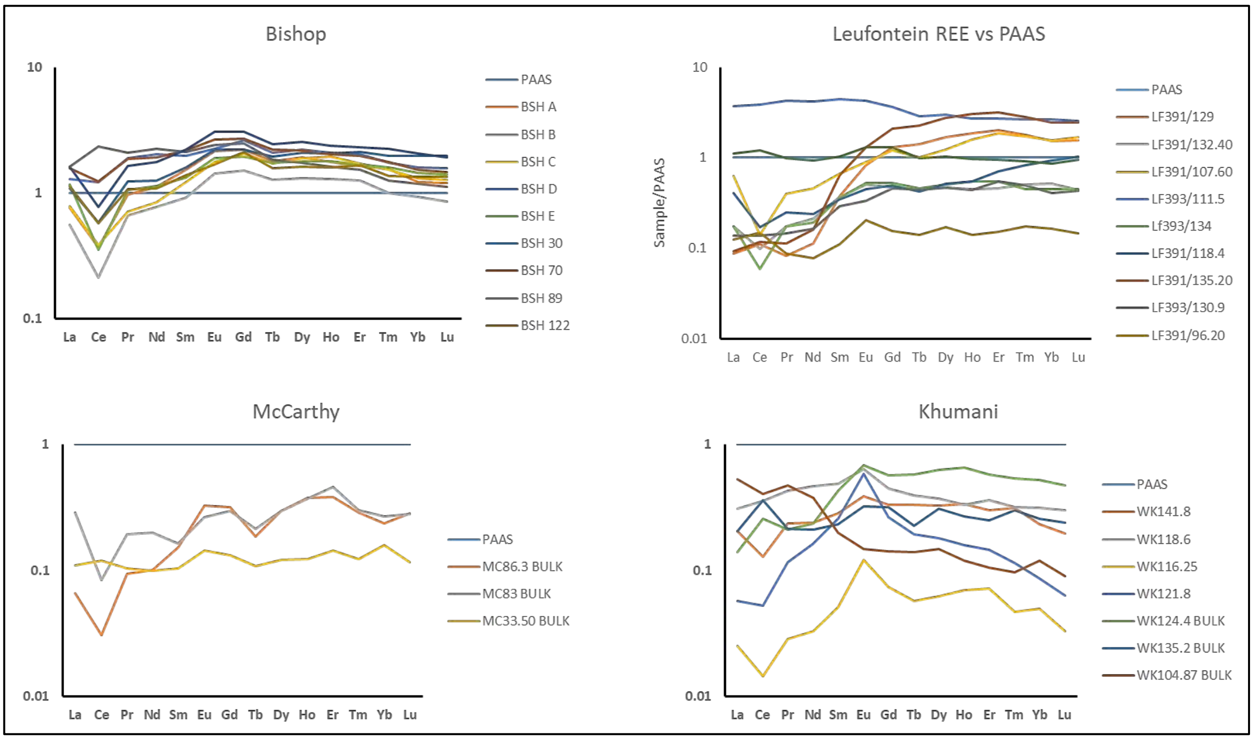

Figure C6: Ore rare earth elements from Bishop, Leeuwfontein, Khumani and McCarthy plotted against PAAS

SEM/EDS

Table C11: Khumani data indicating the presence of fluorine within the manganese ore

Element	Atomic %
O	62.02
F	2.36
Al	0.55
Si	4.74
Ca	0.65
Ti	0.22
Mn	27.93
Fe	1.54
Total	**100**

Table C12: SEM/EDS data from Leeuwfontein indicating the presence of bromine in a barite grain

Element	Atomic %
O	57.7
Ba	10.91
B	17.29
Sr	1.23
Co	0.06
S	12.8
Total	**99.99**